Annual Progress Report for the LIBRA Light Ion Beam Fusion Reactor Project for the Period January-December 1984

B. Badger, T.J. Bartel, M.L. Corradini, R.L. Engelstad, D.L. Henderson, G.L. Kulcinski, E.G. Lovell, G.A. Moses, K.J. O'Brien, R.R. Peterson, L. Pong, M.E. Sawan, I.N. Sviatoslavsky, W.F. Vogelsang, and J.J. Watrous

December 1984

FPA-84-8

FUSION POWER ASSOCIATES

2 Professional Drive, Suite 248
Gaithersburg, Maryland 20879
(301) 258-0545

1500 Engineering Drive
Madison, Wisconsin 53706
(608) 263-2308

ANNUAL PROGRESS REPORT FOR THE LIBRA LIGHT ION BEAM FUSION REACTOR PROJECT FOR THE PERIOD JANUARY-DECEMBER 1984

B. Badger
T.J. Bartel
M.L. Corradini
R.L. Engelstad
D.L. Henderson
G.L. Kulcinski
E.G. Lovell
G.A. Moses
K.J. O'Brien
R.R. Peterson
L. Pong
M.E. Sawan
I.N. Sviatoslavsky
W.F. Vogelsang
J.J. Watrous

Fusion Power Associates
6515 Grand Teton Plaza
Madison, WI 53719

December 1984

FPA-84-8

TABLE OF CONTENTS

1. INTRODUCTION

This is a progress report of work performed between January 1, 1984 and December 31, 1984 by Fusion Power Associates under contract to Kernforschungszentrum Karlsruhe. The purpose of the work is to investigate "critical issues" associated with the conceptual design of the LIBRA Light Ion Beam Fusion Demonstration Reactor. These critical issues all relate to the nuclear island part of the conceptual design. Furthermore, they are generic in nature such that they are relevant to many light ion fusion reactor designs and high yield target experiments. They include:

1. modeling of preformed plasma channel creation by a discharge through a cavity gas;
2. modeling of ion beam transport through a preformed channel;
3. modeling of cavity gas interaction with INPORT units; and
4. modeling of INPORT unit response to the fireball blast.

Most of the work discussed in this report consists of computer code development and the use of these codes for analysis. A good perspective on this work can be drawn by comparing this report with its predecessor from 1983, Fusion Power Associates Report FPA-83-8.

The LIBRA reactor is a demonstration facility driven by high current light ion beams transported through preformed plasma channels. A schematic view of the reactor and blanket is shown in Fig. 1.1. Major parameters for the system are given in Table 1.1. A target yield of 320 MJ and a repetition rate of 1.5 Hz have been selected. The first wall is protected by INPORT units similar to those used in the HIBALL design. The target yield and repetition rate combine to produce 480 MW of fusion power. No blanket neutronics studies have been done for LIBRA but we estimate, using the results of previous studies, that the blanket multiplication will provide us with 612 MW of thermal power. At a 40% thermal efficiency, this gives 245 MW of gross electrical power. With a recirculating power fraction of 12%, the net electrical power is 215 MW. It is within the context of these design parameters that the detailed work reported here was performed.

The following is a list of publications and presentations over the past year (1984) that relate to the LIBRA design.

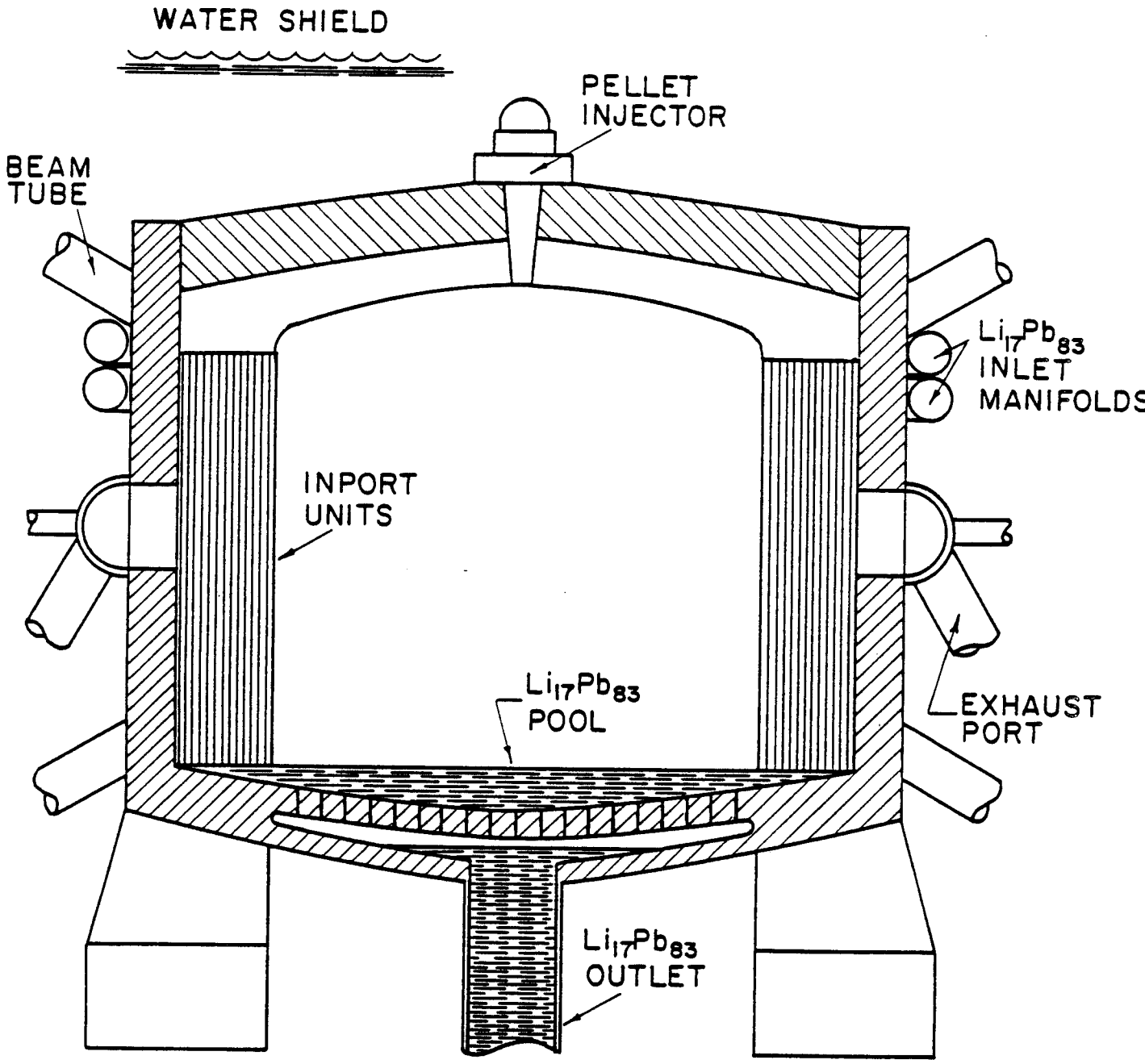

Fig. 1.1. Schematic of LIBRA reactor chamber.

Table 1.1. Major LIBRA Parameters

Reactor Type	Demonstration, Electricity Production
Cost Goal	Less than 10^9 $
Ion Accelerator Type	Helia Pulsed Power/Diode
First Wall Protection	HIBALL-like INPORT Units
Ion Propagation Mode	Preformed Channels
Target Yield	320 MJ
Power on Target	240 TW
Energy on Target	4 MJ
Target Gain	80
Repetition Rate	1.5 Hz
Fusion Power	480 MW
Thermal Power	612 MW
Gross Electrical Power	245 MW
Net Electrical Power	215 MW

1. K.J. O'Brien and G.A. Moses, "Adiabatic Beam Model Theory: Resonant Modification of Transverse Invariants," Bull. Amer. Phys. Soc. 29, 1435 (1984).

2. R.R. Peterson, J.J. Watrous and G.A. Moses, "Microfireball Propagation in Z-Pinch Plasma Channels," Bull. Amer. Phys. Soc. 29, 1350 (1984).

3. R.L. Engelstad and E.G. Lovell, "Mechanical Response and Stability of INPORT Tubes for ICF Reactors," 13th Symposium on Fusion Technology, Varese, Italy, September 1984.

4. R.L. Engelstad and E.G. Lovell, "Analysis of Modal Coupling of Coolant Tubes for Inertial Fusion Applications," 3rd International Modal Analysis Conference, Orlando, FL, January 1985.

5. R.L. Engelstad, "Planar Vibrations of LIBRA INPORT Tubes Including Gravity Gradient Effects," Fusion Power Associates Report FPA-84-2, July 1984.

6. R.L. Engelstad, "Basic Theory for Three-Dimensional Motion of LIBRA INPORT Tubes," Fusion Power Associates Report FPA-84-3, July 1984.

7. G.A. Moses, "ION, A Code to Compute Ion Trajectories in Z-Pinch Plasma Channels," Fusion Power Associates Report FPA-84-5, November 1984.

8. R.R. Peterson, "WINDOW - A Code to Compute Ion Beam Power Constraints," Fusion Power Associates Report FPA-84-6, December 1984.

9. J.J. Watrous, G.A. Moses and R.R. Peterson, "Z-PINCH - A Magnetohydrodynamic Radiative Transfer Computer Code," University of Wisconsin Fusion Engineering Program Report UWFDM-584, June 1984.

2. ION PROPAGATION CODE DEVELOPMENT

2.1 Z-PINCH Magnetohydrodynamic Code

A computer code called Z-PINCH has been developed to describe the creation of plasma channels. The Z-PINCH code[1] is a combination of radiation-hydrodynamics from MF-FIRE,[2] equations of state and opacities from MIXERG,[3] magnetic field diffusion and convection from MAGPIE,[4] and external circuit modeling from WHYRAC.[5] The fundamentals of the Z-PINCH code have been completed and tested. The Z-PINCH code has been used to verify the results of Freeman, Baker and Cook[6] and shows good agreement with their calculations. The first version of the Z-PINCH code was delivered to KfK in July 1984 and has been implemented on their computer system. Further testing and enhancement of the code is continuing. In this report we present full scale results of the code for the problem of channel formation.

The problem to be simulated consists of a laser initiated low temperature argon plasma at a density of 2.25×10^{-5} g/cm^3 through which a two-stage current pulse is discharged. The current pulse shape is shown in Fig. 2.1. This two-stage current pulse is modeled as a succession of two critically damped LRC circuits, Fig. 2.2. Figures 2.3-2.11 show various quantities output by the Z-PINCH code. Each of these figures is compared with the results of Freeman, Baker and Cook where possible. The R-T plots, Fig. 2.3, show the trajectories of the Lagrangian zones and are an excellent way of visualizing the channel dynamics. The first current pulse is small enough that the expansive force due to Joule heating dominates over the $\underline{J} \times \underline{B}$ pinching force of the magnetic field. A shock wave is driven outward, evacuating the channel to less than 10% of its initial density. The second, stronger pulse, creates a strong magnetic field which pinches the channel very rapidly. The ion beam is injected into the channel shortly after 5 μs, once the magnetic field is established but before the field has time to pinch the channel. The other figures show the radial profiles of the hydrodynamic quantities during the first and second current pulses. Figure 2.11 shows a roughly linear magnetic field with a maximum of nearly 20 kG at 5.3 μs.

The first version of the 1-D MHD code, Z-PINCH, was completed in June 1984 and implemented at KfK in July 1984. Since that time, the code has been undergoing modifications that will allow ion beam-channel interaction simulations to be performed.

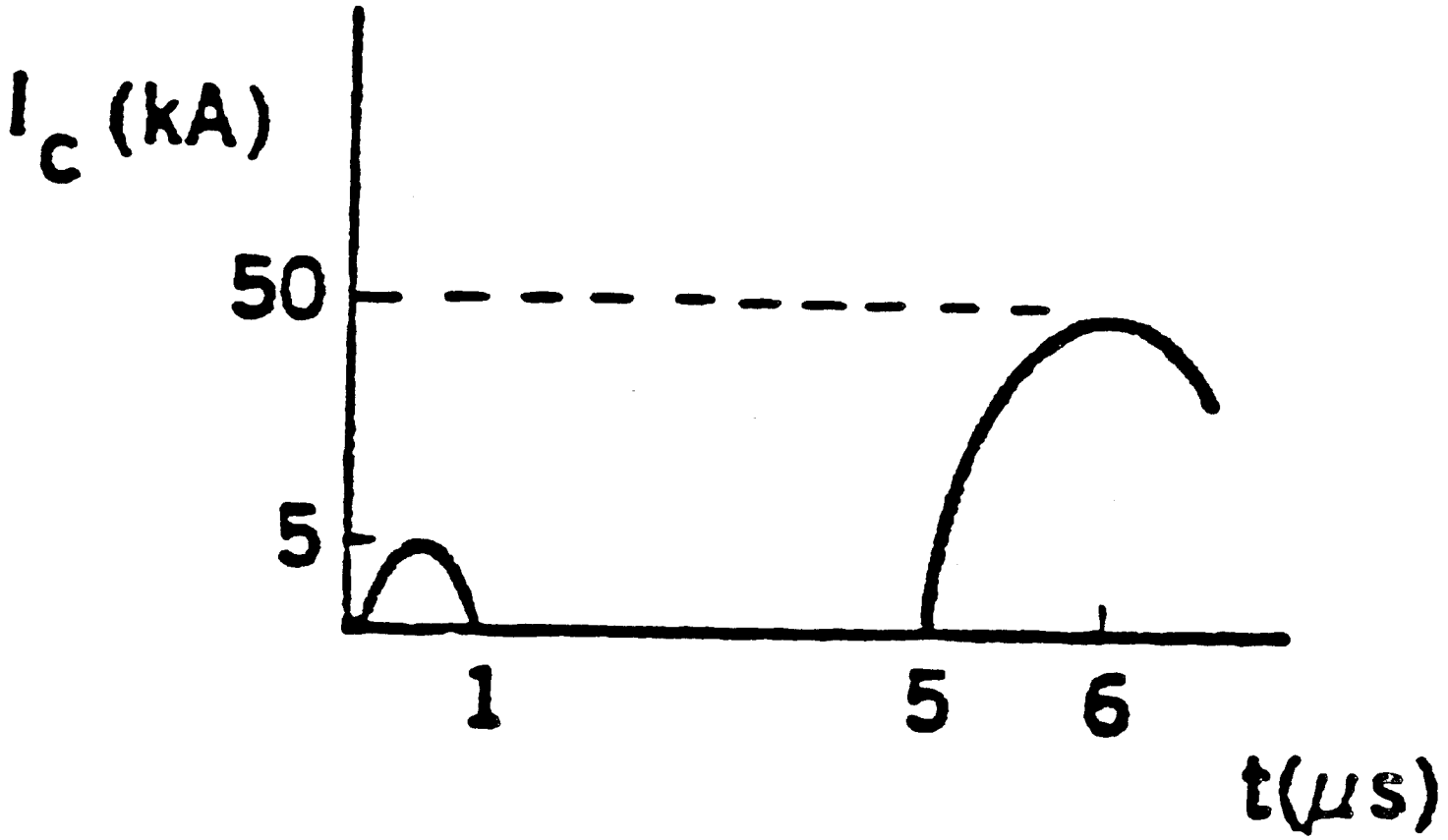

Fig. 2.1. Two-stage current pulse.

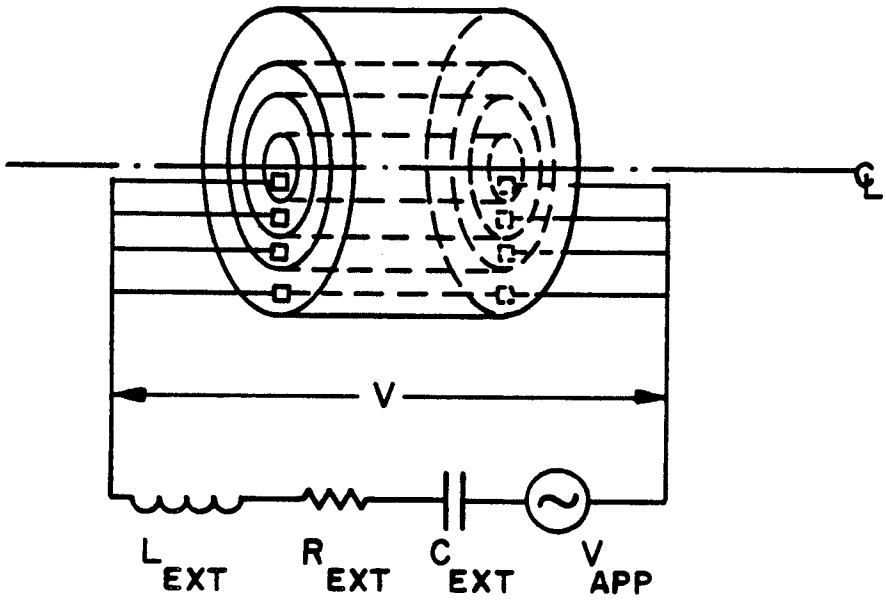

Fig. 2.2. External circuit.

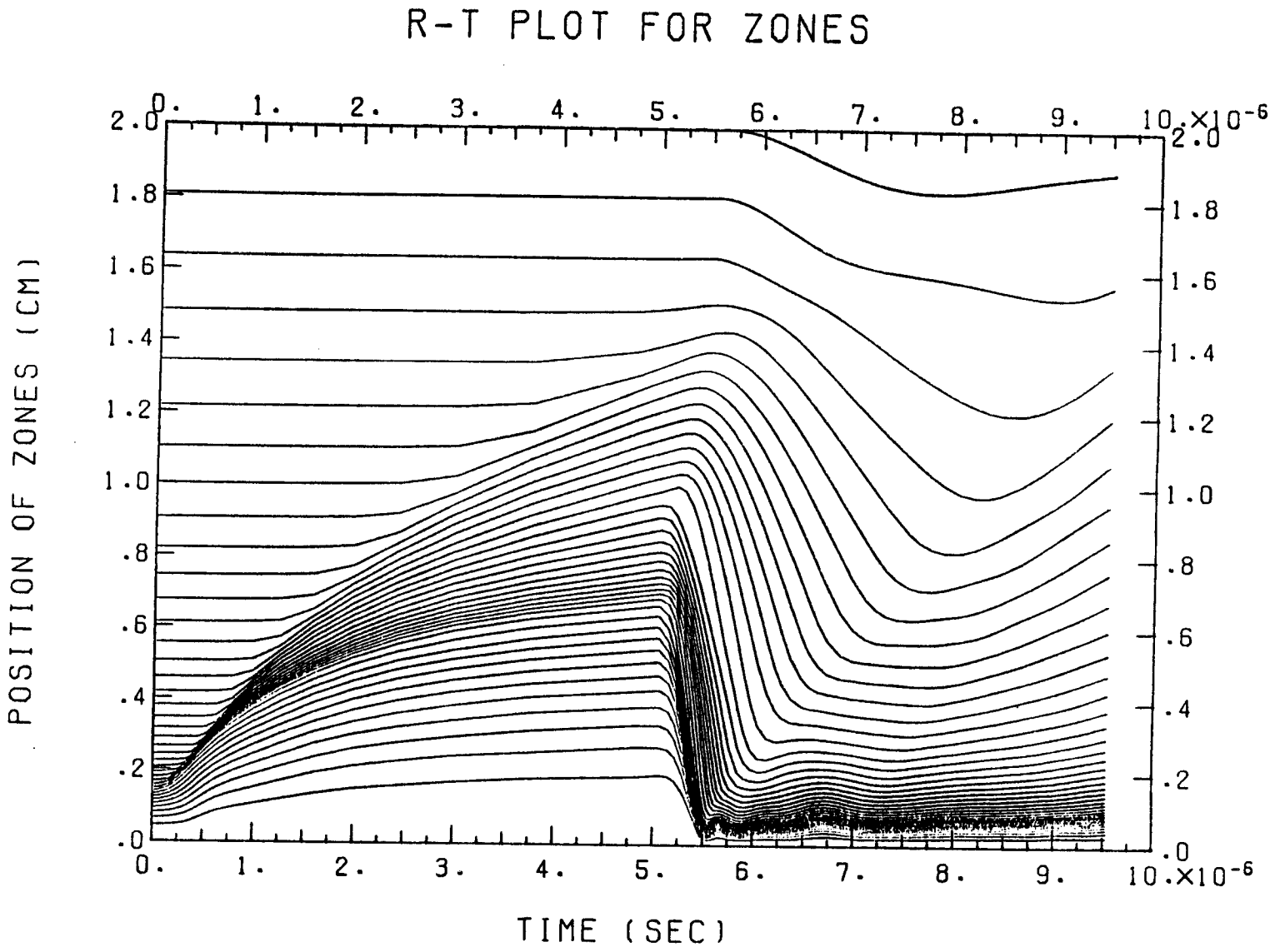

Fig. 2.3. R-T plot for zones.

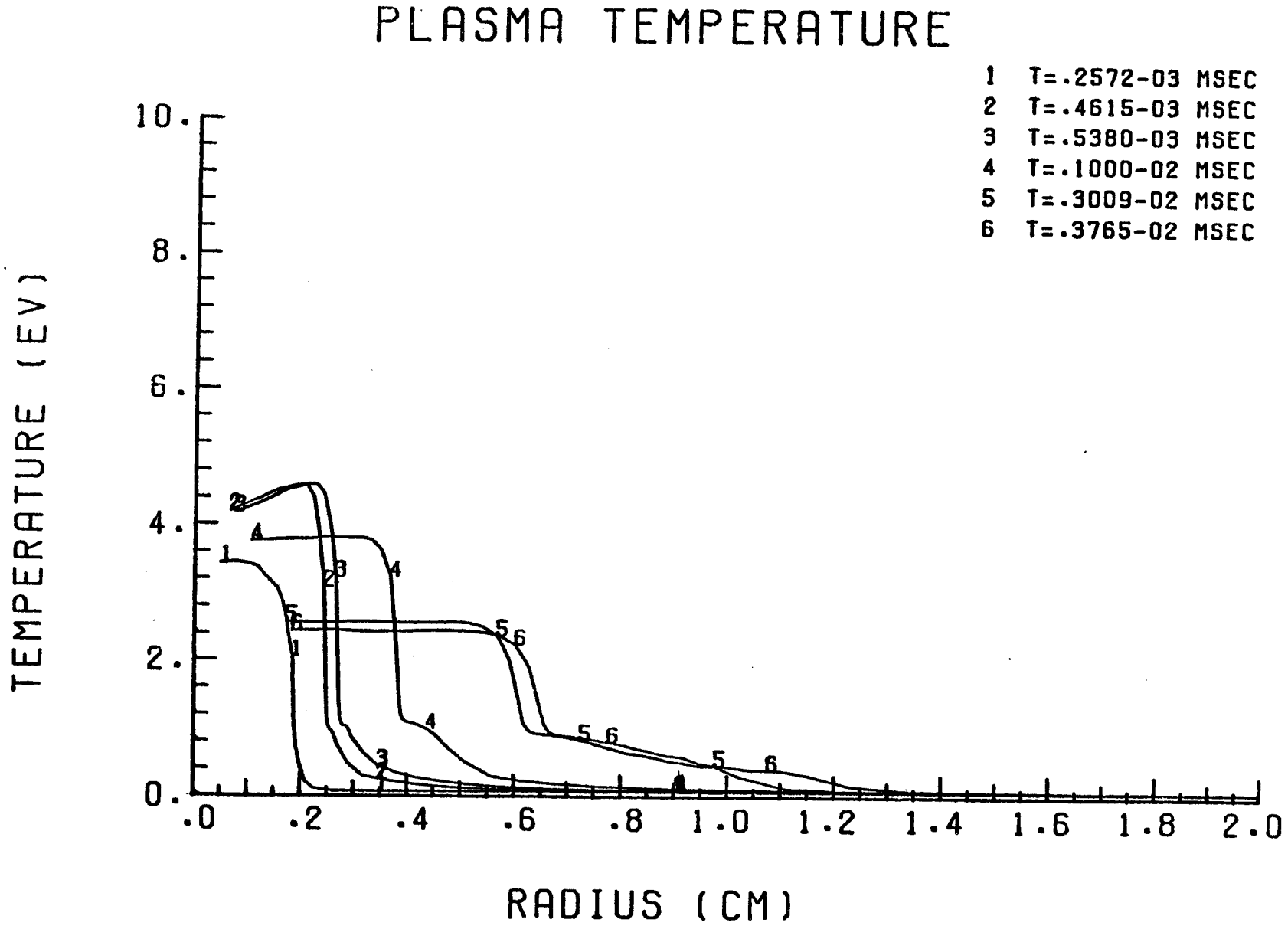

Fig. 2.4. Plasma temperature during first current pulse.

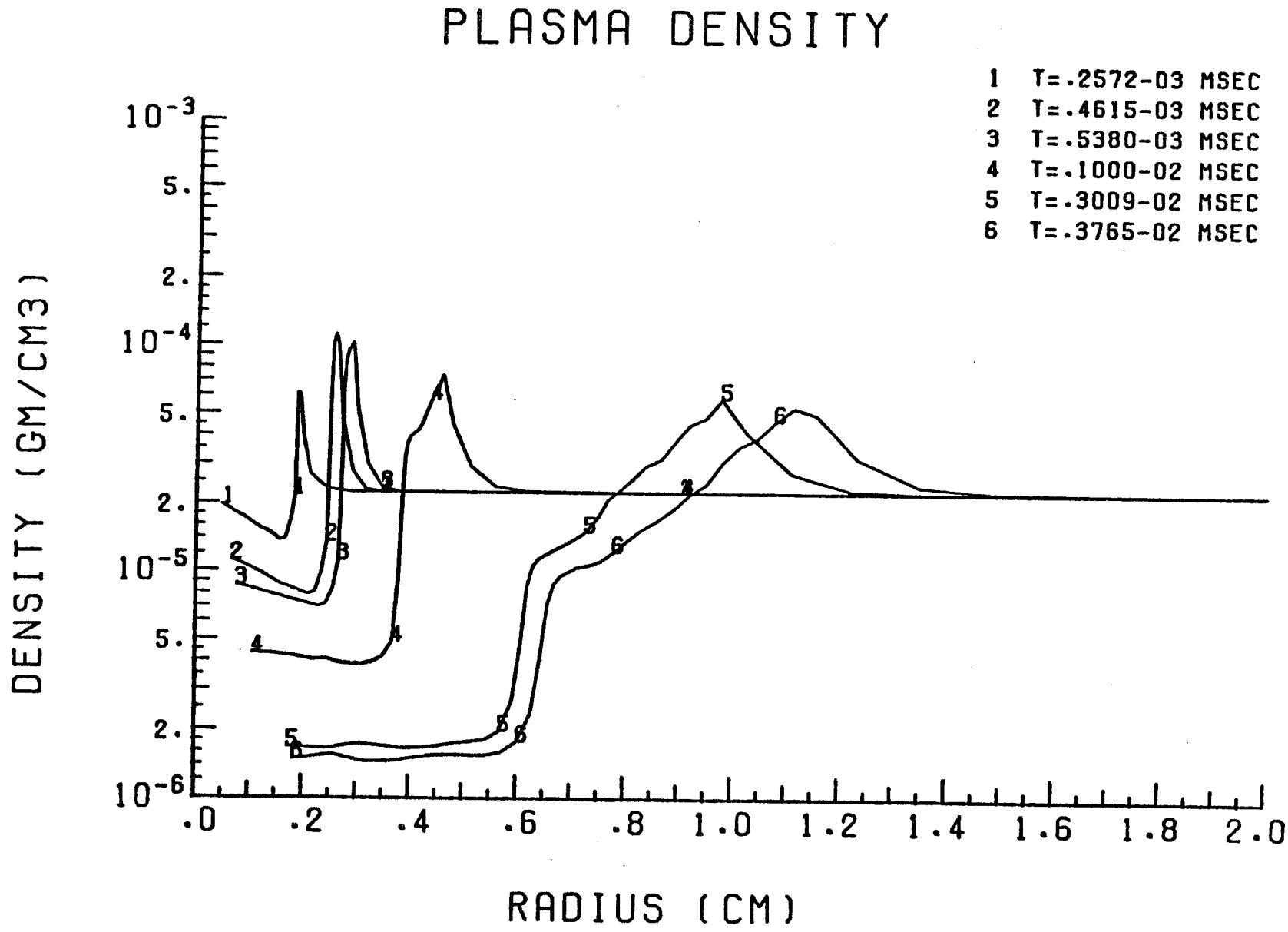

Fig. 2.5. Plasma density during first current pulse.

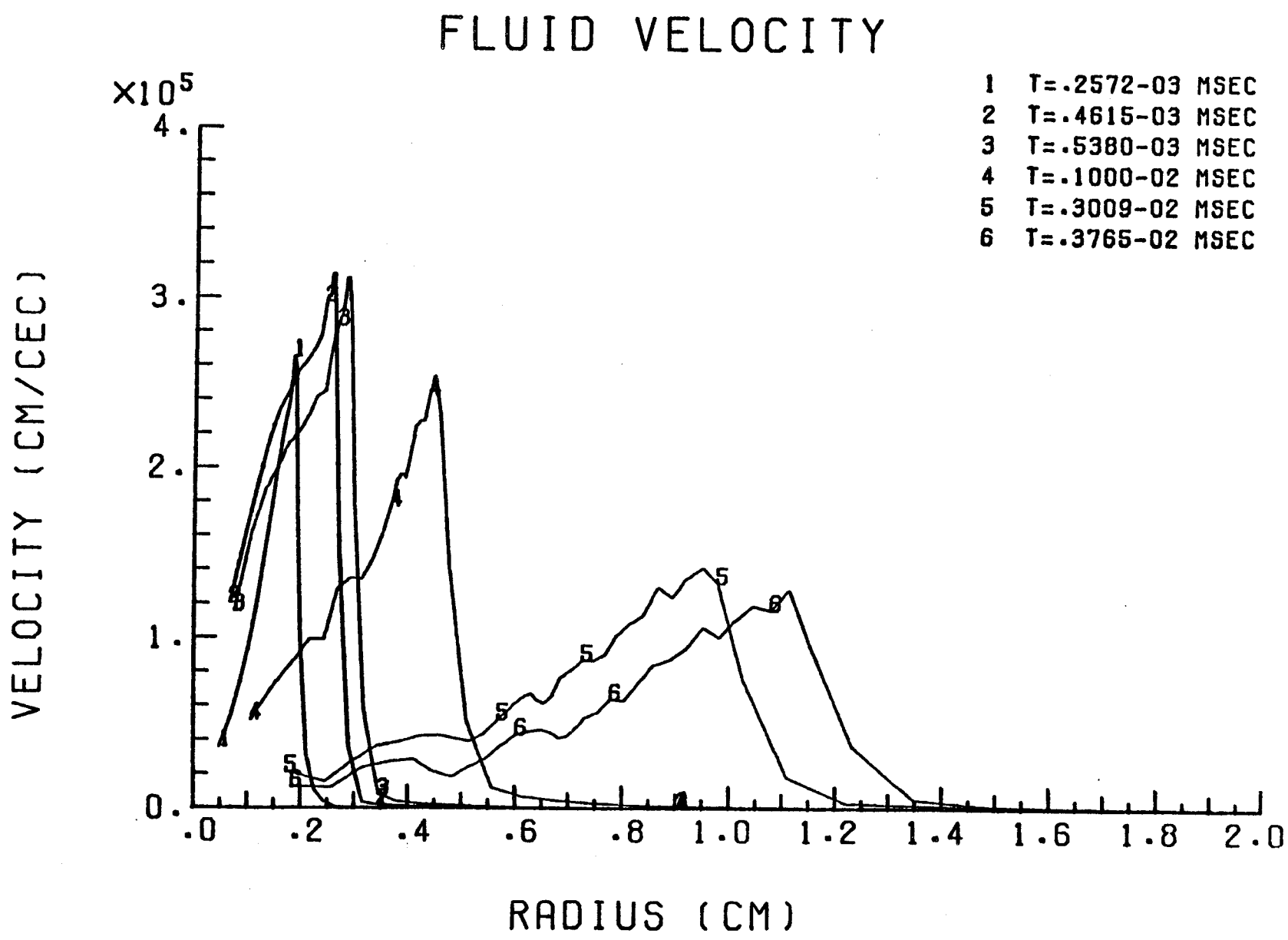

Fig. 2.6. Fluid velocity during first current pulse.

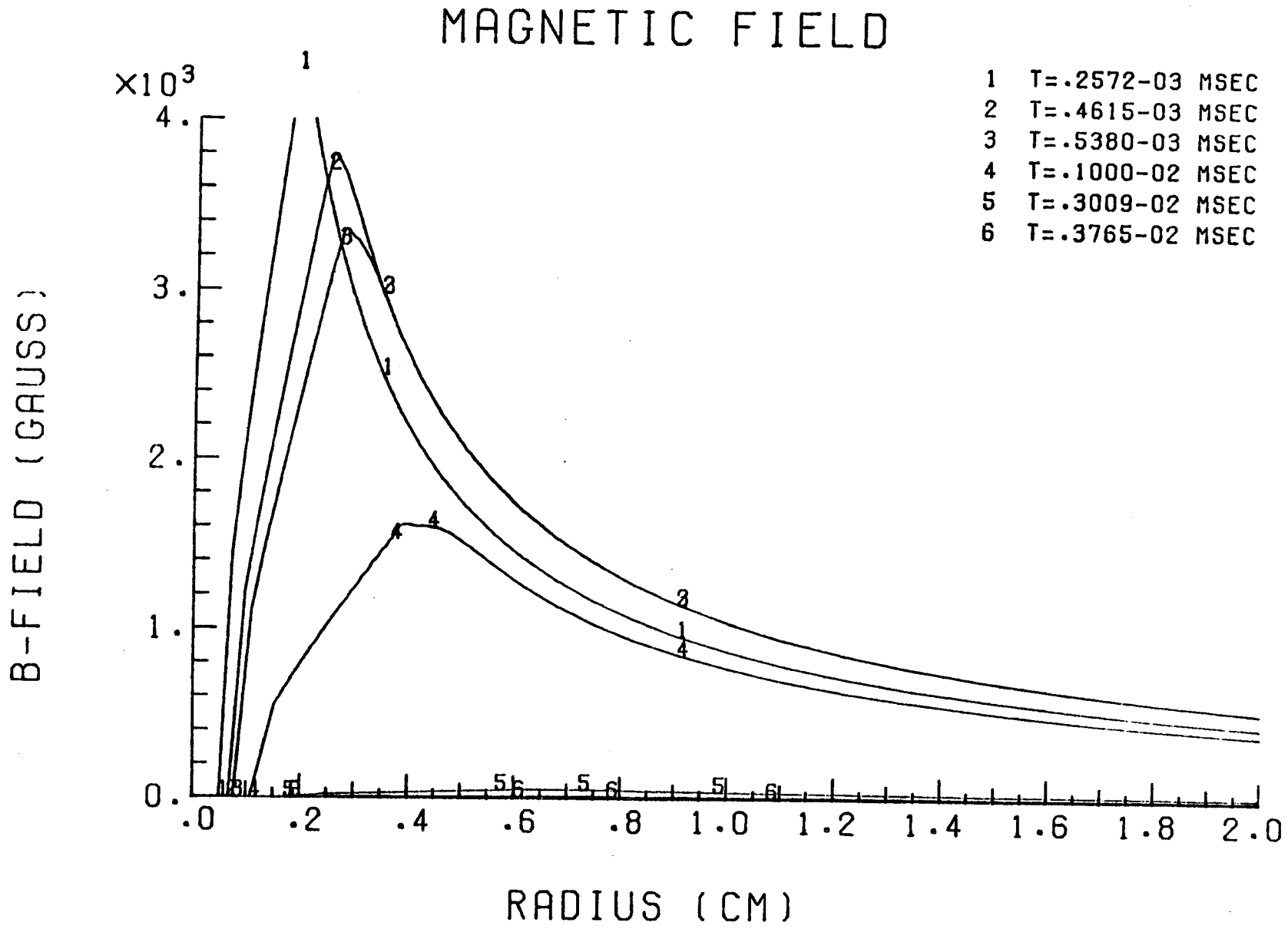

Fig. 2.7. Magnetic field during first current pulse.

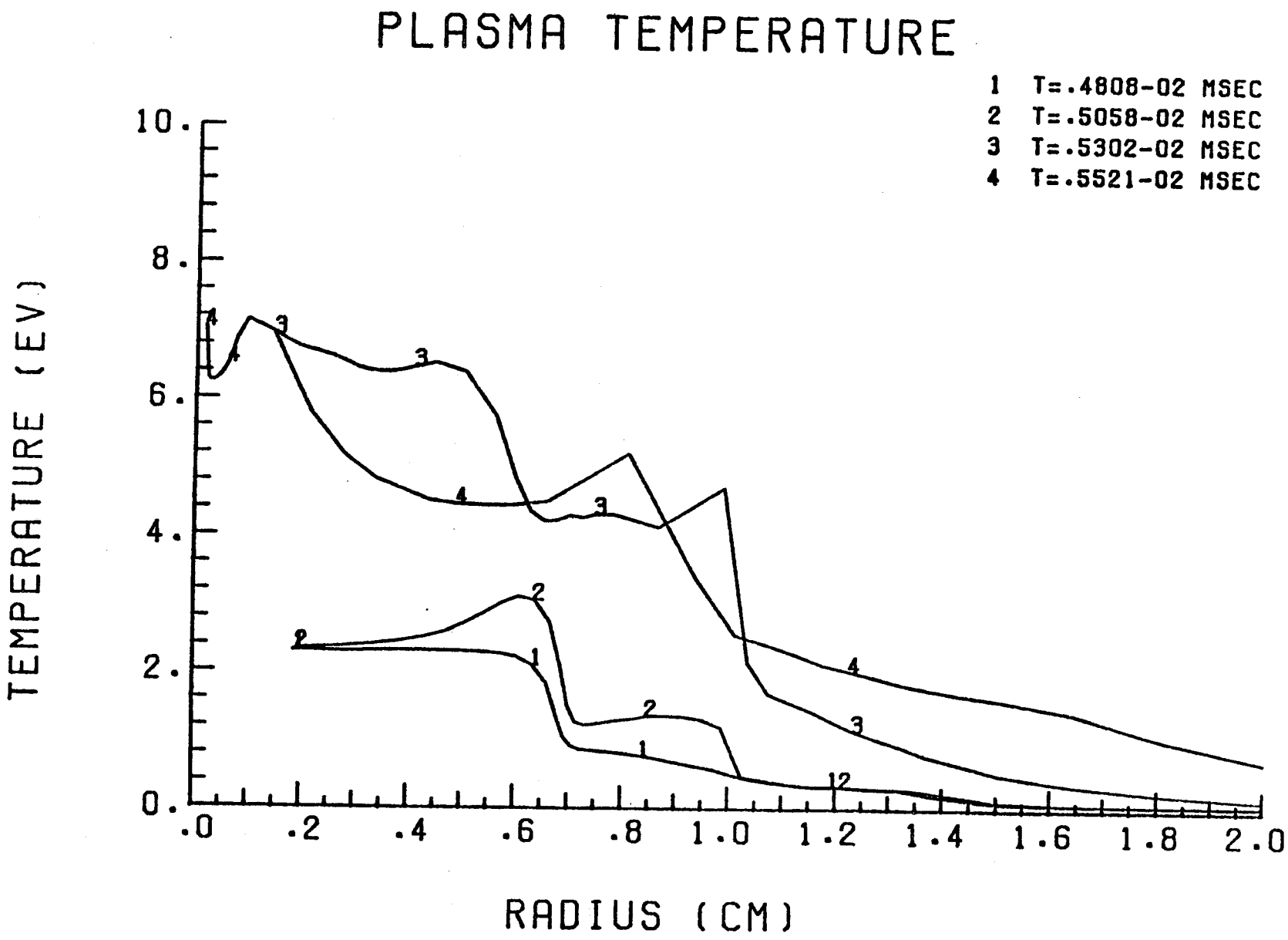

Fig. 2.8. Plasma temperature during second current pulse.

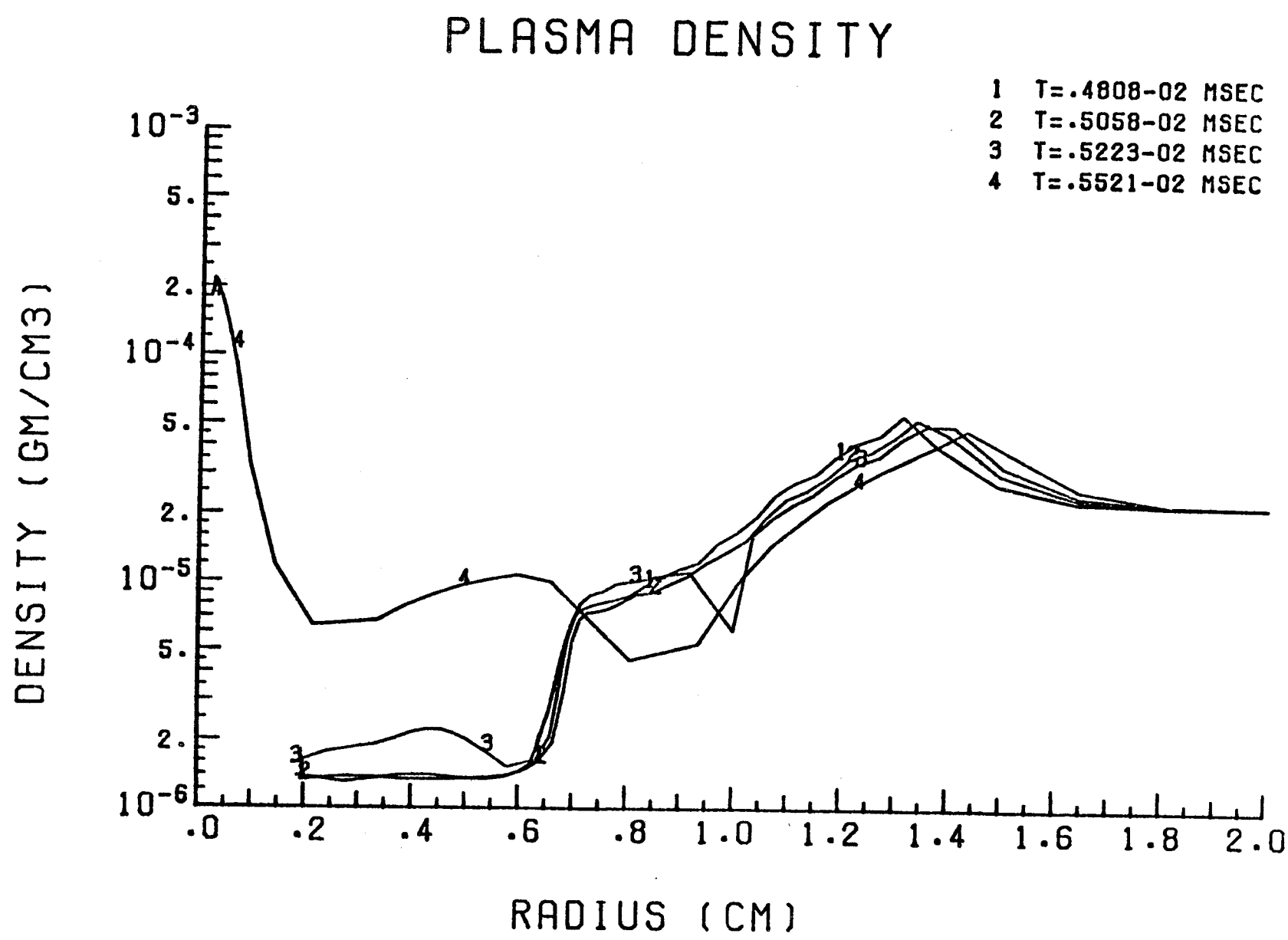

Fig. 2.9. Plasma density during second current pulse.

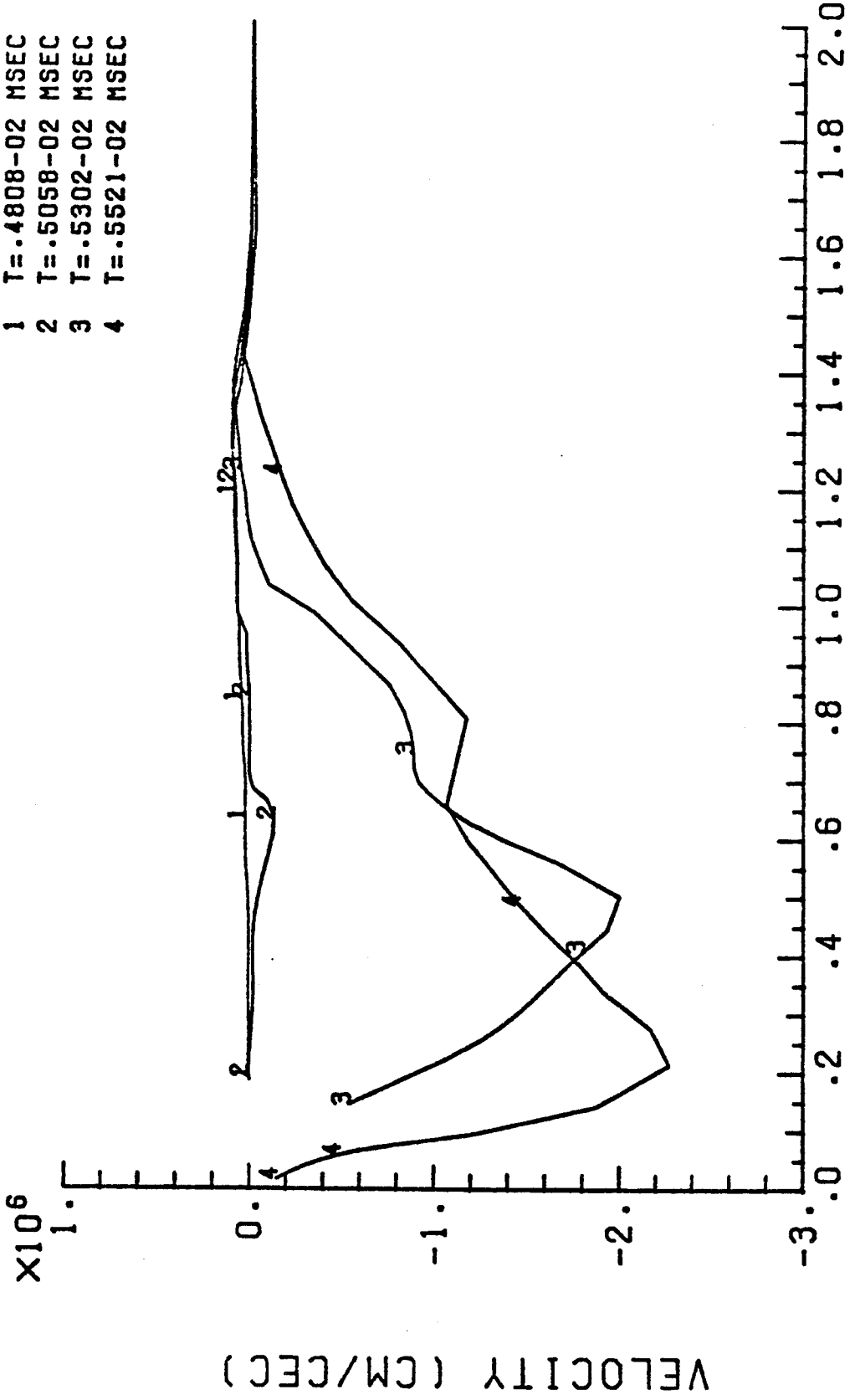

Fig. 2.10. Fluid velocity during second current pulse.

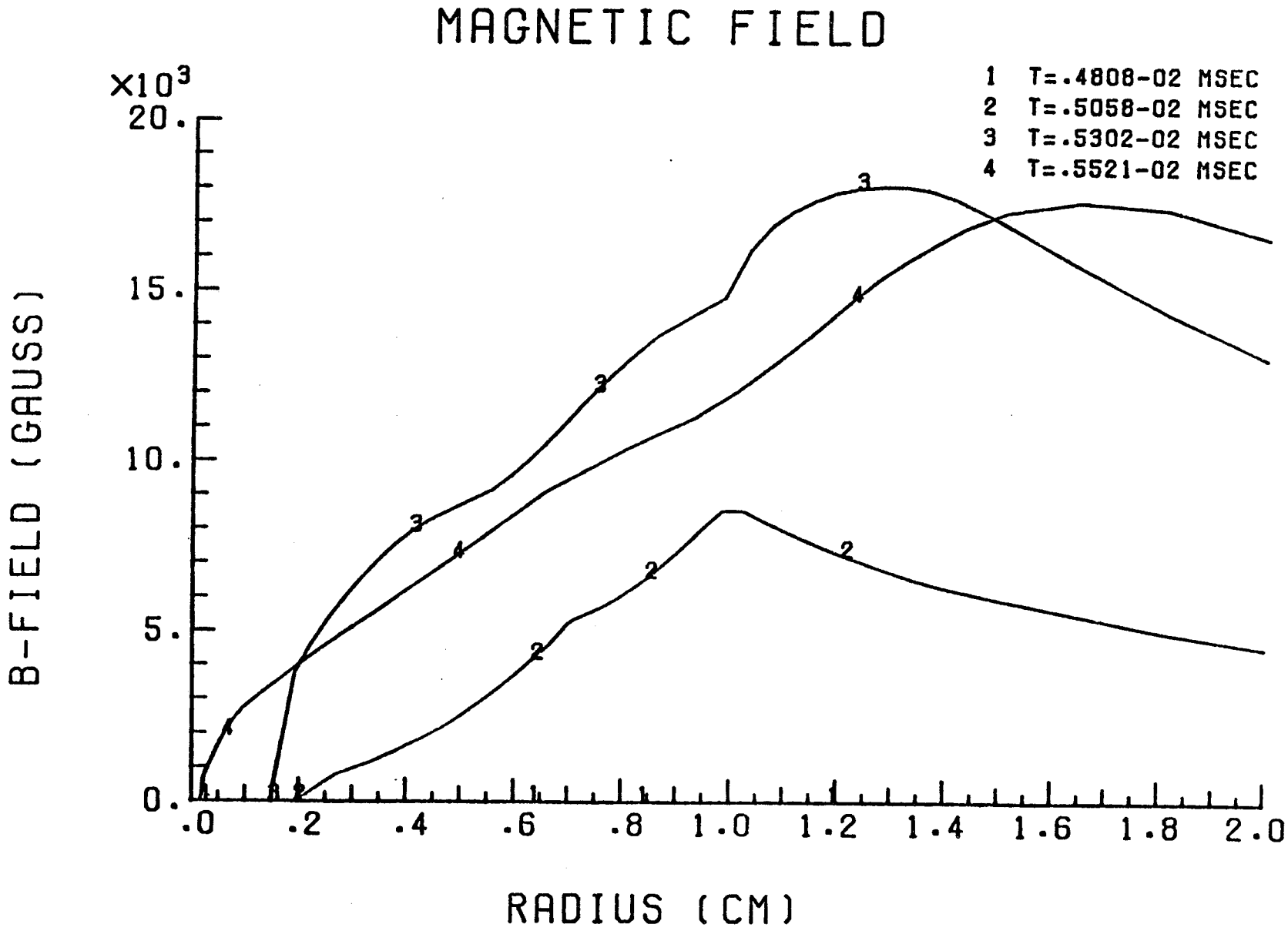

Fig. 2.11. Magnetic field during second current pulse.

The ion beam is modeled within the framework of the 1-D MHD model used to describe the discharge plasma. While this model is not completely valid on the beam timescale, it is able to represent the gross effects of the beam/channel interaction. These effects include heating of the discharge plasma due to collisional energy loss of the beam ions and a return current density induced by the beam current. The two main modifications necessary to include the beam in Z-PINCH are the addition of source terms to the magnetic diffusion equation and to the plasma energy equation.

The source term required for the magnetic diffusion equation may be obtained by rederiving that equation. The equation is obtained by combining Ampere's, Faraday's, and Ohm's Laws:

$$\overrightarrow{\nabla \times B} = \frac{4\pi}{c} (\vec{J}_{tot}) \; ; \; \vec{J}_{tot} = \vec{J}_d + \vec{J}_{return} + \vec{J}_{beam}$$

$$\overrightarrow{\nabla \times E} = - \frac{1}{c} \frac{\partial \vec{B}}{\partial t} \; ; \; \eta(\vec{J}_d + \vec{J}_{ret}) = \vec{E} + \frac{1}{c} \overrightarrow{u \times B} \; .$$

Note that the beam current appears as part of the source in Ampere's Law, but does not appear in Ohm's Law. Combining these equations by eliminating $\vec{J}_{tot}$ and $\vec{E}$ gives the magnetic diffusion equation:

$$\frac{\partial \vec{B}}{\partial t} + \vec{\nabla} \times \frac{\eta c^2}{4\pi} \overrightarrow{\nabla \times B} = \vec{\nabla} \times \overrightarrow{u \times B} - c \overrightarrow{\nabla \times (\eta \vec{J}_{beam})}$$

or, in the case of cylindrical geometry with axial and azimuthal symmetry,

$$\frac{\partial B}{\partial t} - \frac{\partial}{\partial r} \frac{\eta c^2}{4\pi} \frac{1}{r} \frac{\partial}{\partial r} rB = \frac{\partial}{\partial r} uB - c \frac{\partial}{\partial r} \eta J_{beam} \; .$$

Thus, the source term is $-c \frac{\partial}{\partial r} \eta J_{beam}$.

The source term to the plasma energy equation is obtained by considering the energy that a beam ion loses from collisions with the discharge plasma electrons. This may be calculated from the classical ion slowing formula from plasma kinetic theory:

$$\frac{d}{dt} \left(\frac{m_b v_b^2}{2}\right) = -\nu \left(\frac{m_b v_b^2}{2}\right)$$

where $$\nu = 2 \frac{m_b}{m_e} \left[\frac{4\pi q_b^2 e^2}{m_b^2 v_b^3} \ln \Lambda\right] .$$

Over a single timestep, the energy lost by a beam ion is

$$\Delta\varepsilon^{n+1/2} \simeq \Delta t^{n+1/2} (\nu^{n+1/2} \varepsilon^n) .$$

This energy loss is then summed over all the ions in the beam and added to the plasma energy.

It should be stressed that although the effect of the beam on the channel is included in this model, the effect of the channel on the beam is not. The beam parameters are specified by the user and do not change in the course of the calculation. The user must specify the energy, mass, and charge state of a beam ion, and the beam current density profile. The beam ions are currently assumed to be monoenergetic.

One series of tests of the beam-channel interaction have been performed. These tests consist of running Z-PINCH in a simplified mode where neither hydrodynamic motion nor changes in temperature are allowed. By inputting various beam current density profiles, the modified magnetic diffusion equation may be tested.

Figures 2.12 and 2.13 show the induced current density and total current density (sum of induced and beam currents) -- the discharge current was set to zero in these tests for a beam current profile given by

$$J_b(r,t) = \begin{cases} 1 \text{ MA/cm}^2 , & r \leq 0.25 \text{ cm} \\ 0 , & r > 0.25 \text{ cm} \end{cases}$$

The plots indicate nearly complete current neutralization occurring within ~ 100 ns. The current neutralization takes place on the resistive timescale, $\tau_R \simeq r_c^2/(\eta c^2/4\pi)$, which, for this problem, was 27 ns. Figures 2.14 and 2.15 show the induced current density and total current density for τ_R = 3.0 μs. For this case of higher conductivity, the induced current builds up much more slowly.

Figures 2.16 and 2.17 show the induced and net current density for a beam profile given by

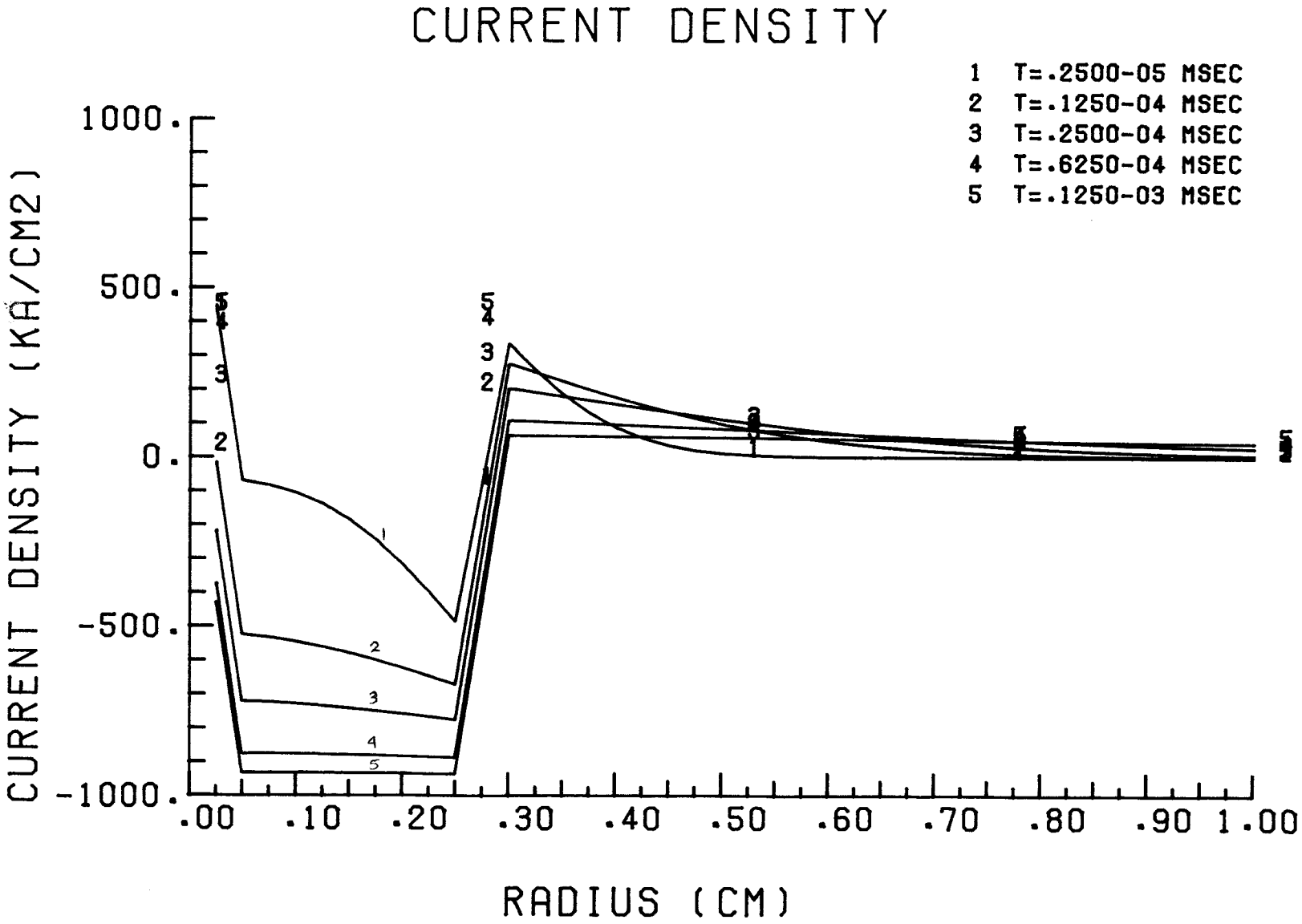

Fig. 2.12. Induced current density for 1 MA/cm^2 ion beam.

RUN ID = 6628

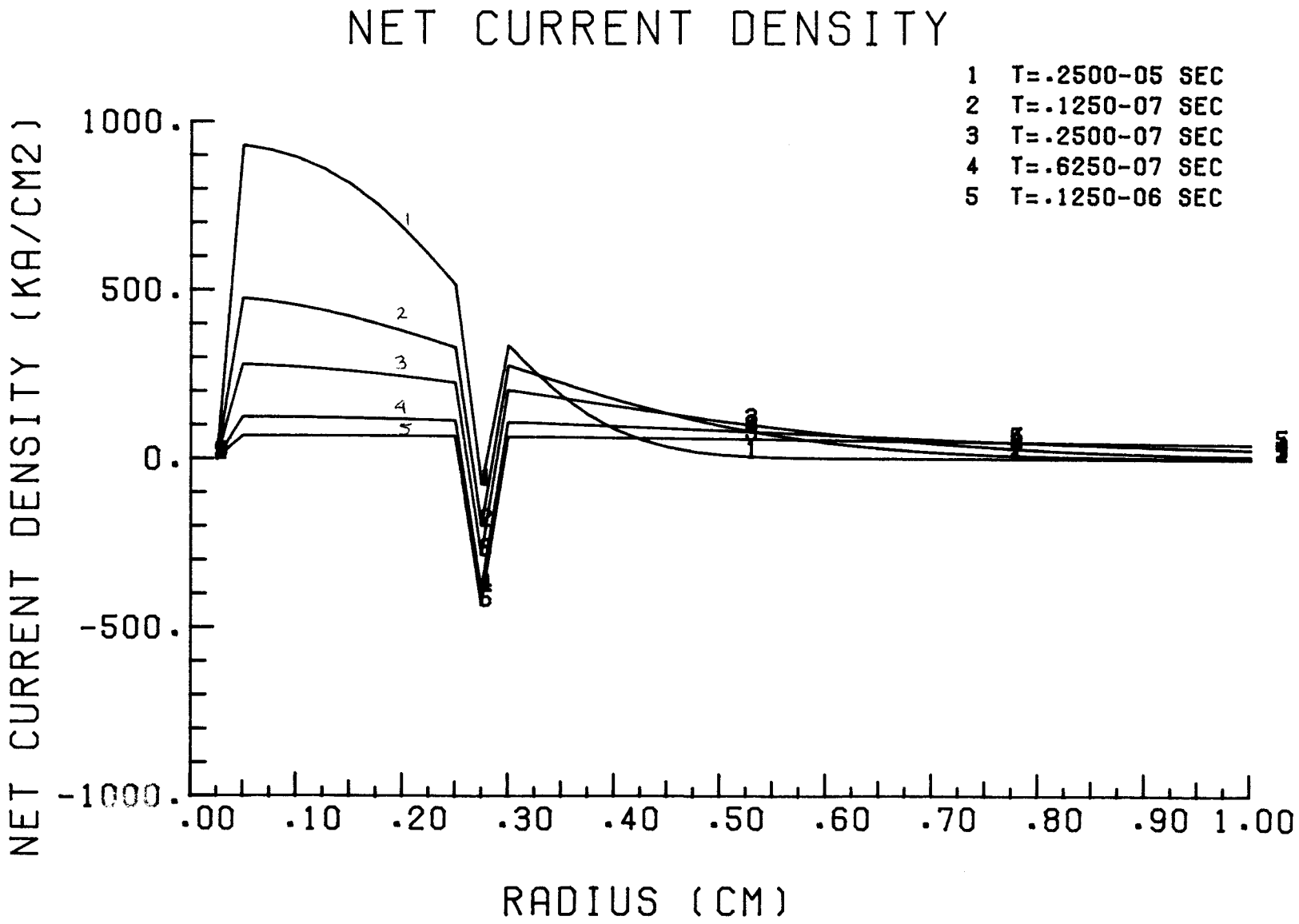

Fig. 2.13. Net current density for 1 MA/cm^2 ion beam.

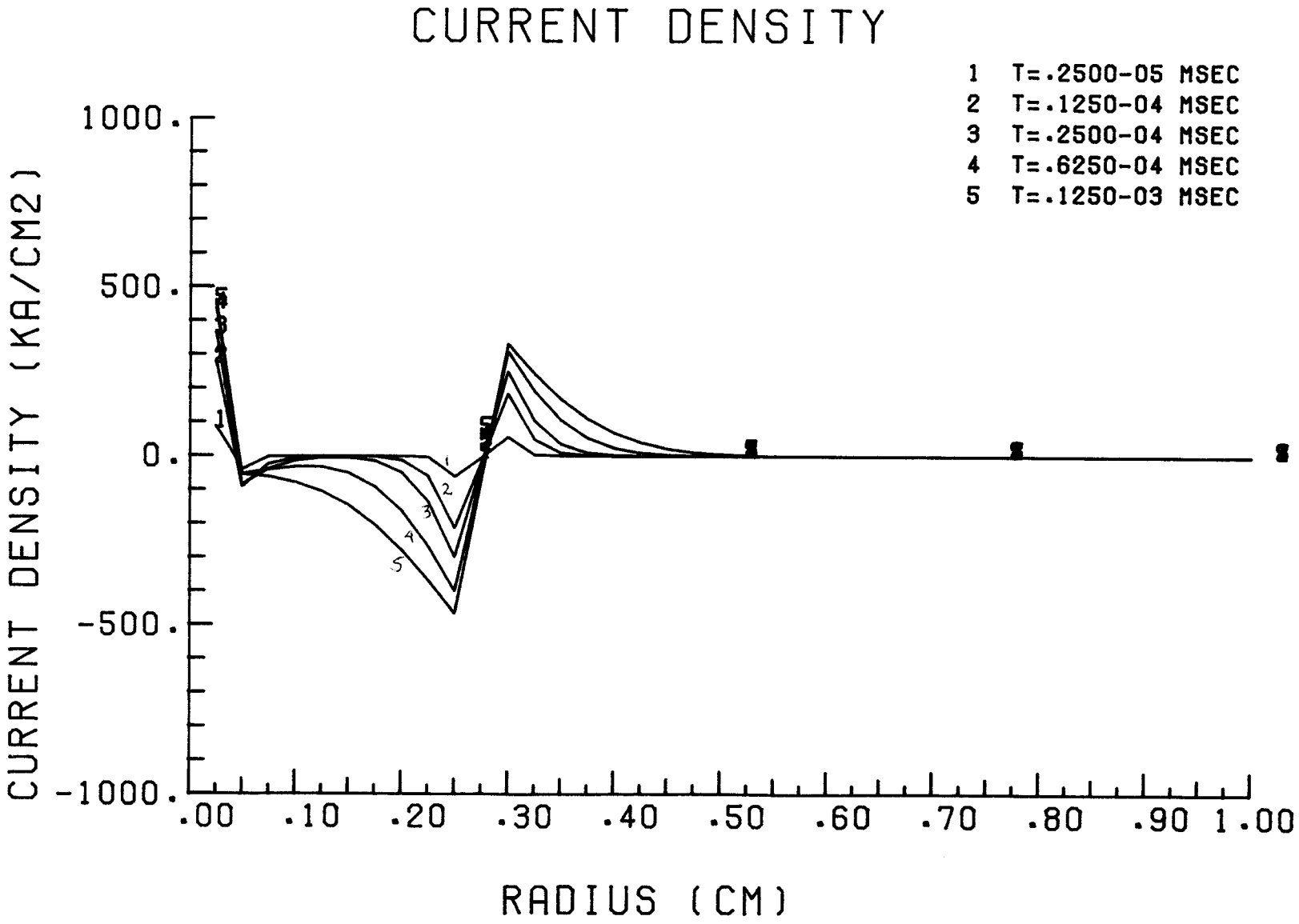

Fig. 2.14. Induced current density in low resistivity plasma channel.

RUN ID = 6589

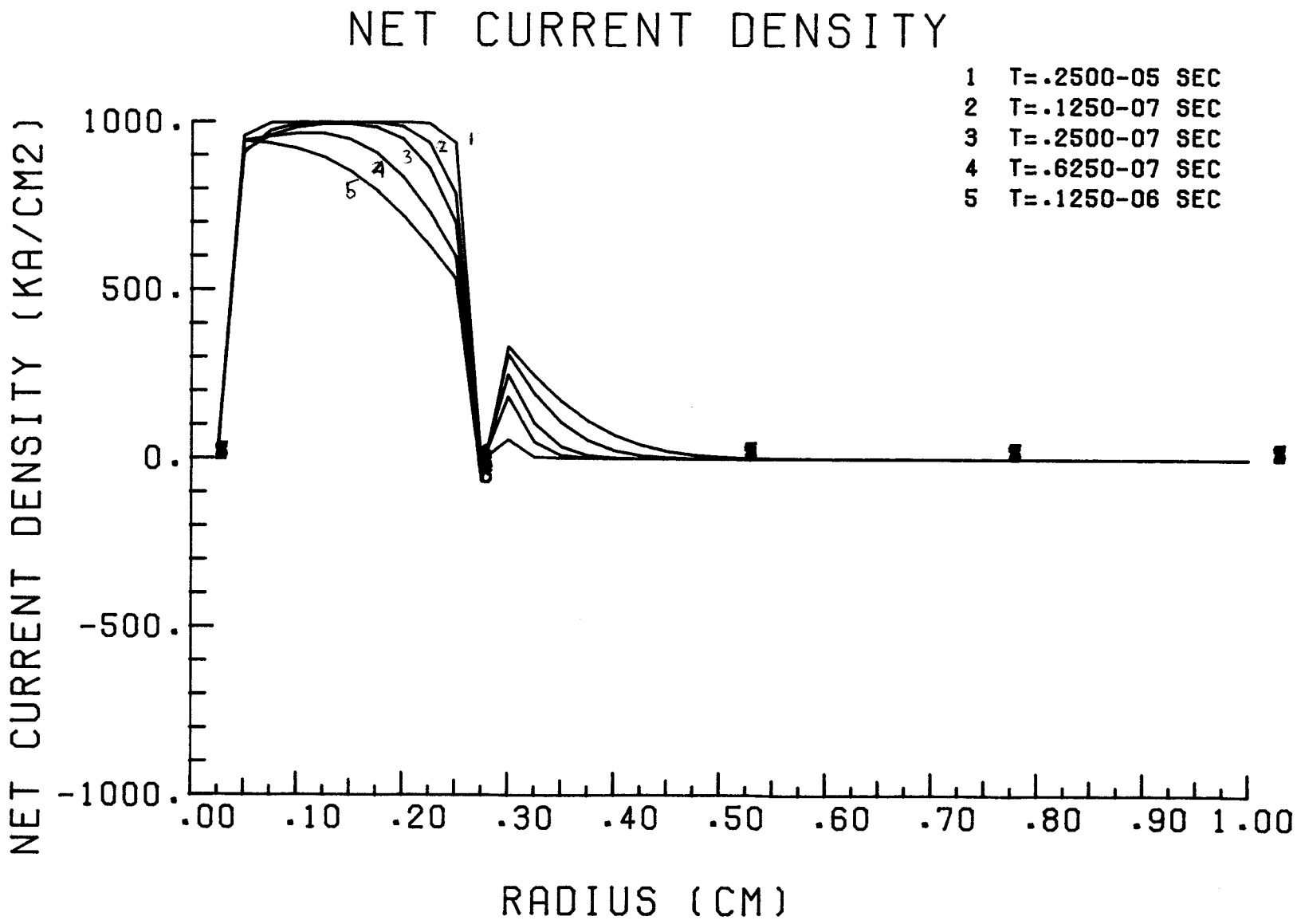

Fig. 2.15. Net current density in low resistivity plasma channel.

RUN ID = 6589

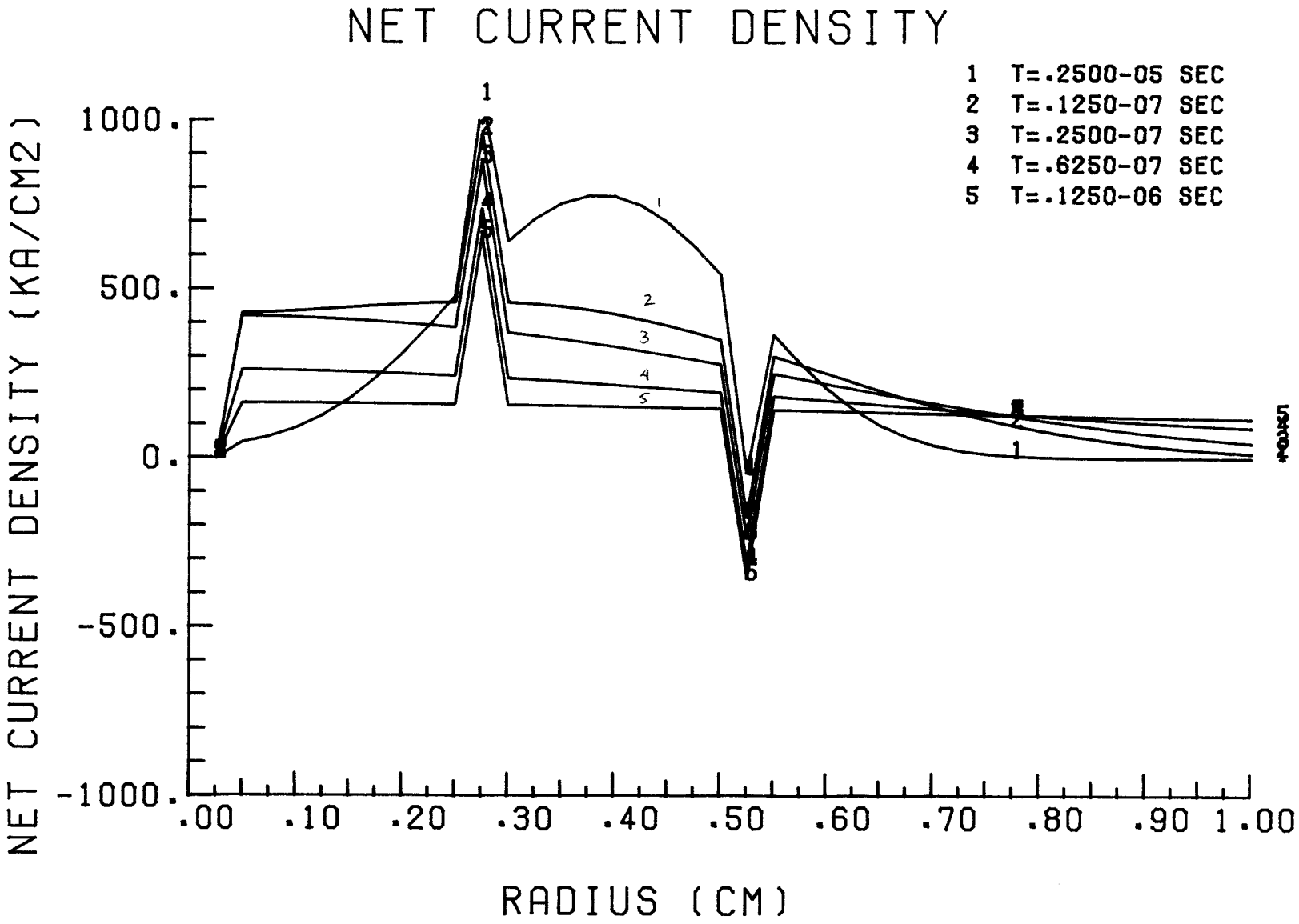

Fig. 2.16. Induced current density for annular ion beam profile.

RUN ID = 6589

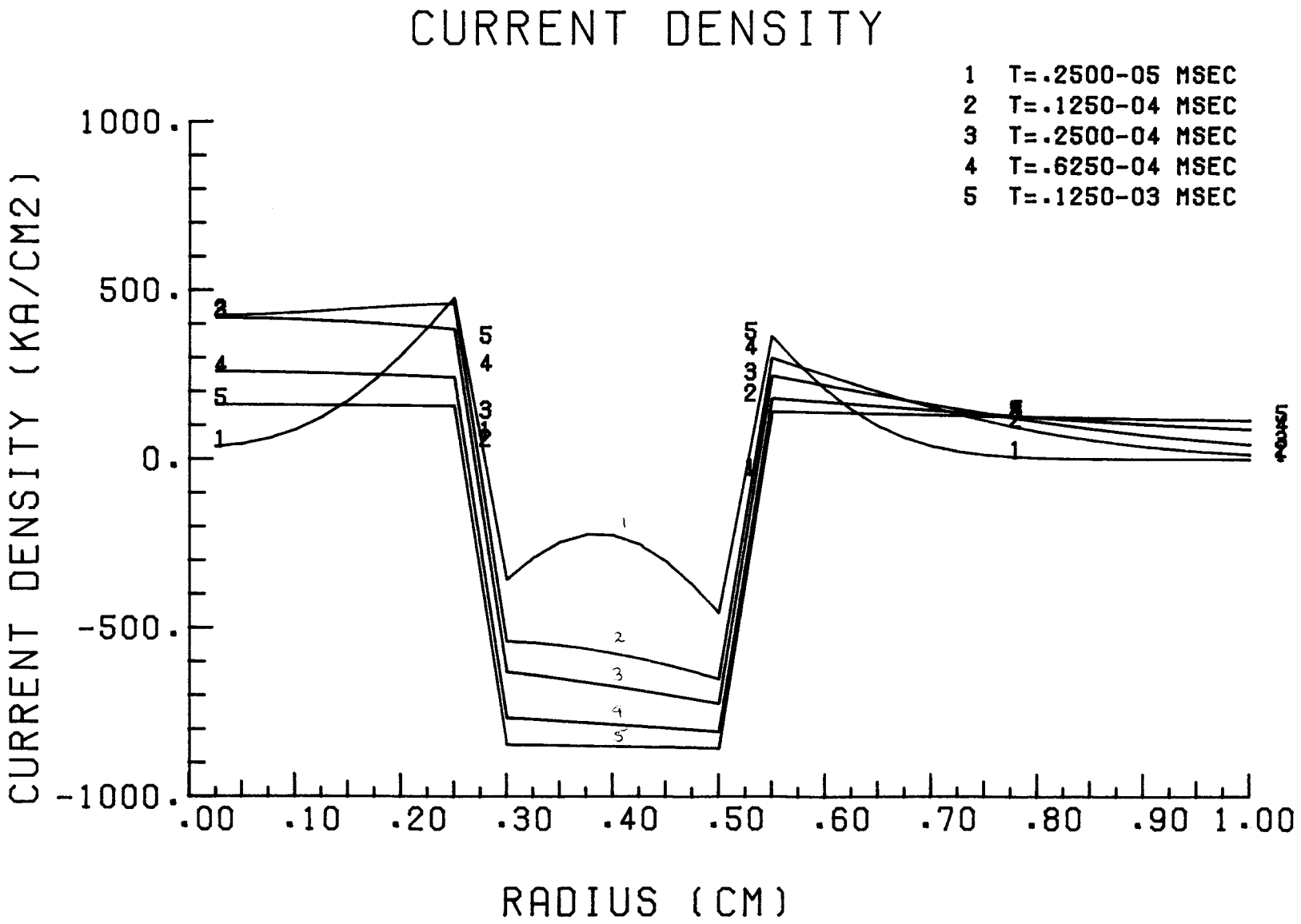

Fig. 2.17. Net current density for annular ion beam profile.

RUN ID = 6589

$$J_b(r,t) = \begin{cases} 10^{-3}\ \text{MA/cm}^2 , & r \leq 0.25\ \text{cm} \\ 1\ \text{MA/cm}^2 , & 0.25\ \text{cm} < r \leq 0.50\ \text{cm} . \end{cases}$$

Again, the beam current is almost completely neutralized within about 100 ns (τ_R = 27 ns).

This additional beam-channel model is currently being fully tested. These preliminary results indicate that the model is working properly and more extensive tests will soon be completed.

2.2 ION Trajectory Code

The ION code determines the trajectories of individual ions in a plasma channel assuming that the ideal conditions of perfect space charge and current neutralization are in effect. The only forces on the ions are the magnetic field due to the current driven through the channel plasma by an external circuit. By stochastically injecting ions into the channel according to some radial and angular distribution the ION code can graphically determine the envelope of the beam made up of these ions. This will allow the determination of the transport efficiency for varying diode focusing parameters and for different magnetic field configurations in the channel. The code is written in a modular fashion in standard FORTRAN 77 and can be easily modified to add new effects or to measure different beam parameters.

There are currently three different ion trajectory models implemented in the ION code. The first two are analytic in nature and are taken from the paper by Ottinger, Mosher, and Goldstein, "Propagation of Intense Ion Beams in Straight and Tapered Z-Discharge Plasma Channels," Ref. 7. These were in the first implementation of the ION code delivered to KfK in July 1984. The third model uses a numerical integration of the equations of motion of the ion in an arbitrary $B_\theta(r,z)$ field and has been added since that time.

An axially uniform plasma channel (confusingly called a "straight" channel in Ref. 7) with a radially uniform current density results in an azimuthal magnetic field of the form

$$B_\theta = B_o\, r/r_c \qquad r < r_c$$

$$B_\theta = B_o\, r_c/r \qquad r > r_c$$

where r_c is the radius of the uniform current profile and B_o is the magnetic field at this radius. The equations of motion for an ion of mass m_i and charge Q in this linear magnetic field are

$$\ddot{r} = -\omega_{cb}\dot{z}\, r/r_c$$

$$\ddot{z} = \omega_{cb}\dot{r}\, r/r_c$$

where the beam cyclotron frequency is

$$\omega_{cb} = QeB_o/m_i c \ .$$

It is assumed that there is no angular momentum component to the ion motion. Approximate solutions to these equations can be obtained for the condition $\dot{r}/\dot{z} \ll 1$ (i.e., the ions are injected at a shallow angle of injection). The initial conditions for these equations of motion are shown in Fig. 2.18. The approximate analytic solutions are[7]

$$z(t) = \left(V_o \cos\alpha_o - \frac{\omega_{cb}\bar{r}^2}{4r_c}\cos 2\phi\right)t$$

$$+ \frac{\bar{r}^2}{8r_c}\left(\frac{r_c\omega_b}{V_o\cos\alpha_o}\right)^{1/2}\left[\sin 2(\omega_\beta t + \phi) - \sin 2\phi\right] + O(\varepsilon^3)$$

$$r(t) = \bar{r}\cos(\omega_\beta t + \phi) + O(\varepsilon^3)$$

where

$$\omega_\beta = \Omega\left(1 - \frac{\omega_{cb}\bar{r}^2}{16\, r_c V_o \cos\alpha_o} + \frac{\tan^2\alpha_o}{4}\right)$$

$$\tan\phi = -\left(\frac{r_c V_o \cos\alpha_o}{\omega_{cb}\cos\alpha_o}\right)^{1/2}\tan\alpha_o$$

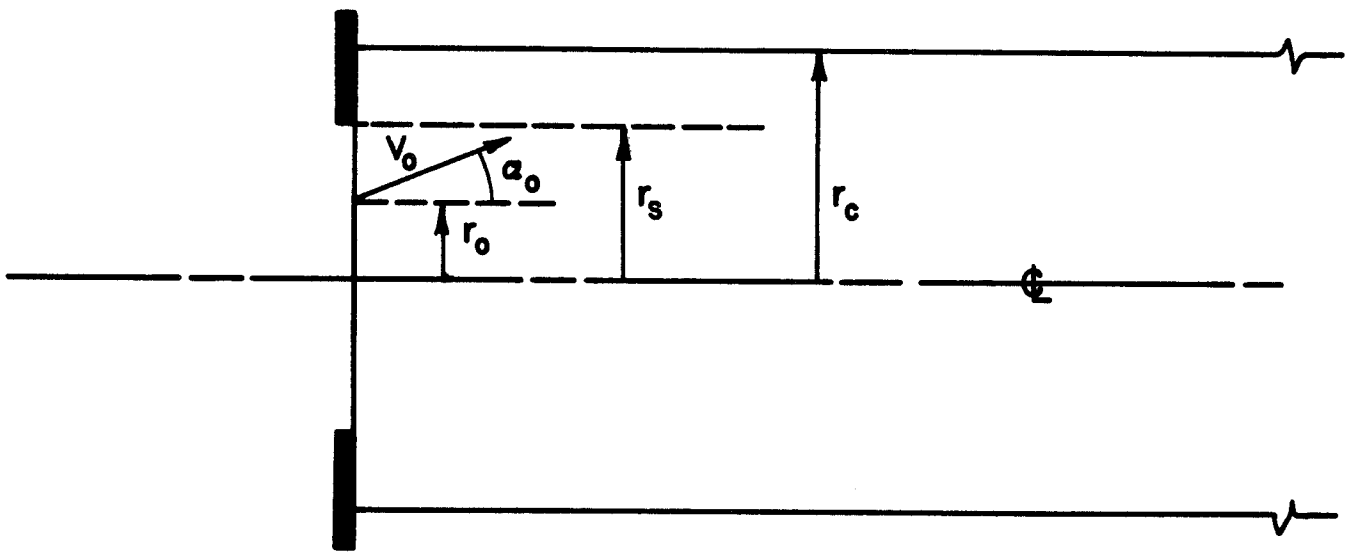

Fig. 2.18. Ion orbit initial conditions at channel entrance.

$$\bar{r} = \left(r_o^2 + \frac{r_c V_o \sin^2 \alpha_o}{\omega_{cb} \cos \alpha_o}\right)^{1/2}$$

$\Omega = (\omega_{cb} V_o \cos \alpha_o / r_c)^{1/2}$ = betatron frequency

V_o = constant speed of ion

α_o = angle of injection into the channel

$r(0) = r_o$ $\qquad$ $\dot{r}(0) = V_o \sin \alpha_o$

$z(0) = 0$ $\qquad$ $\dot{z}(0)\ V_o \cos \alpha_o$.

These conditions demand that the channel current satisfy[7]

$$I_o > (1.57 \times 10^7 \frac{m_i/m_p}{Q} \alpha_m^2 V_o/c)(1 - r_s^2/r_c^2)^{-1} \text{ amps}$$

to confine ions with a maximum injection angle of α_m, where m_p is the proton mass.

If the channel radius is assumed to decrease linearly along its length such that

$$r_c(z) = r_c(1 - z/L) ,$$

then $$B_\theta = \frac{2I_o r}{c r_c^2 (1 - z/L)^2} \qquad r < r_c(1 - z/L)$$

where L is the taper length, r_c is the channel radius at z = 0 and this expression only applies for

$$(L - z)^2 >> r^2 .$$

In this case the equations of motion for an ion take the form

$$\ddot{r} = - \frac{\omega_{cb} \dot{z} r}{r_c (1 - z/L)^2}$$

$$\ddot{z} = \frac{\omega_{cb}\dot{r}r}{r_c(1 - z/L)^2}$$

where $$\omega_{cb} = \frac{2\,QeI_o}{m_i c^2 r_c} .$$

Again, for $\dot{r}/\dot{z} << 1$, these equations may be solved approximately to give the ion orbit as[7]

$$z(t) = V_o t + O(\varepsilon^2)$$

$$r(t) = r_o(1 - t/T)^{1/2} \cos[-\Omega T \ln (1 - t/T)]$$

$$+ \left(V_o \sin \frac{\alpha_o}{\Omega}\right)(1 - t/T)^{1/2} \sin[-\Omega T \ln (1 - t/T)] + O(\varepsilon^2)$$

where $$T = L/V_o$$

$$\Omega^2 = \omega_{cb} V_o / r_c$$

$$r(0) = r_o \qquad \dot{r}(0) = V_o \alpha_o$$

$$\dot{z}(0) = V_o$$

$$\alpha_o << 1 \quad \text{and} \quad (\Omega T)^{-1} << 1 .$$

Rather than using either of the previous approximate analytic solutions to the ion orbit equations one can simply integrate the two second order O.D.E.'s

$$\ddot{r} = -\frac{Qe}{m_i c} B_\theta(r,z)\, \dot{z}$$

$$\ddot{z} = \frac{Qe}{m_i c} B_\theta(r,z)\, \dot{r} .$$

These are converted to four first order O.D.E.'s by a change of variables

$$r_t = \dot{r} \qquad z_t = \dot{z}$$

$$\dot{r}_t = -\frac{Qe}{m_i c} B_\theta(r,z)\, z_t$$

$$\dot{r} = r_t$$

$$\dot{z}_t = \frac{Qe}{m_i c} B_\theta(r,z)\, r_t$$

$$\dot{z} = z_t \,.$$

The initial conditions are

$$r(0) = r_o \qquad r_t(0) = V_o \sin \alpha_o$$
$$z(0) = 0 \qquad z_t(0) = V_o \cos \alpha_o \,.$$

These equations are solved using a standard fifth order Runge-Kutta algorithm using the IMSL library routine DVERK.

There are three different output options for each of the three orbit models, thus providing nine different kinds of calculations. These three output options are:

1. trace the trajectory of ions for a specified length of time;
2. show the positions of all ions at a selected instant in time;
3. plot the radial profile of ions as they pass through a plane at a specified position in the channel.

Other output options can be easily added to each orbit model by including another ELSE IF statement in the appropriate subroutine.

In all cases the ions are randomly injected into the channel in a Gaussian distribution in radius and a uniform distribution in angle. These are shown in Fig. 2.19. The initial radius r_o is selected by sampling the distribution

$$r_o = r_s \sqrt{-2 \ln \xi}$$

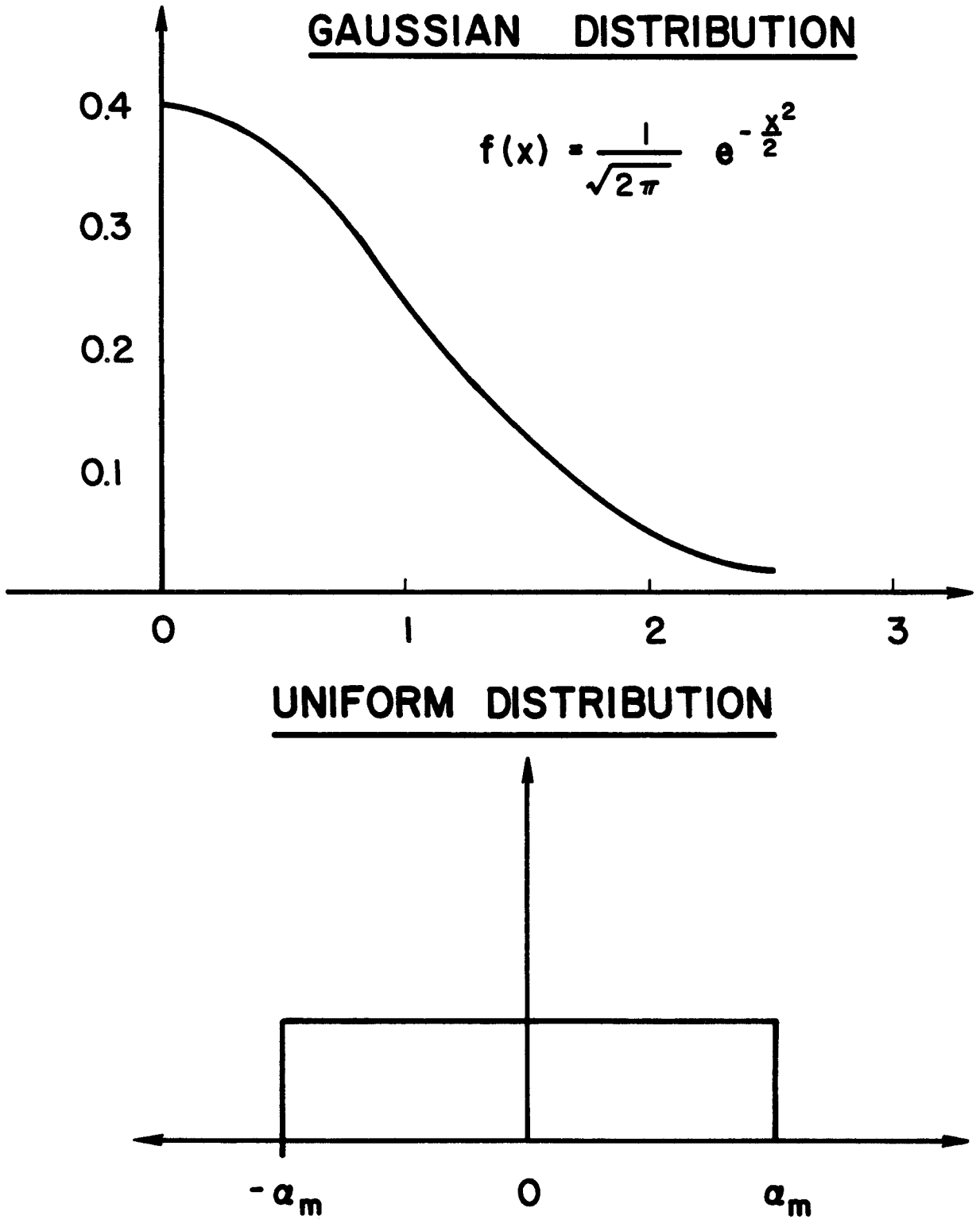

Fig. 2.19. Radial and angular distributions used for ion injection into channel.

and the angle of injection is selected by sampling

$$\alpha_o = \alpha_m (1 - 2\xi)$$

where ξ is a random number uniformly distributed in the interval [0,1]. The code uses pseudo-random numbers where the same initial seed number will produce the same sequence of random numbers. Random numbers are obtained by calling the IMSL routine GGUBFS.

This example demonstrates the use of the arbitrary $B_\theta(r,z)$ model of the channel with the ion trajectory output option. The input for the calculation is given in Table 2.1. The BTHETA subroutine computes $B_\theta(r,z)$ and can be programmed by the user to be anything that he wishes. In this example the form

$$B_\theta(r,z) = B_o(r/r_c)^n , \qquad n = 5$$

is used. This provides a small magnetic field in much of the channel with a strong rise near the edge of the channel. This can be used to simulate the magnetic field profile that the tail of the ion beam experiences after the head of the beam has "pushed" the field out of the channel. The trajectories shown in Fig. 2.20 demonstrate the nearly linear orbits of the ions with reflections from the walls of the channel. The polynomial magnetic field of order five only acts on the ions near the channel radius and thus does not allow enough time for the force to turn the ions around to confine them. Hence, more ions are lost using this model than in the linear magnetic field model.

2.3 WINDOW (FENSTER) Beam Stability Code

The WINDOW computer code[8] was developed as a design tool to find the power limits on ion beams propagating in plasma channels. In the initial version of WINDOW delivered to KfK in July 1984, the length of the channel, the power compression due to bunching, the energy spread in the beam, and the fractional energy loss by the beam while it is in the channel were fixed in the code so the user did not have control over them. In the new version of WINDOW reported here, the user is given the choice of channel length, power compression factor and fractional energy loss. The beam energy spread is

Table 2.1

```
 WHAT TYPE OF CHANNEL CALCULATION DO YOU WANT?
 0 = STOP THE CALCULATION
 1 = STRAIGHT CHANNEL - ANALYTIC SOLUTION
 2 = TAPERED CHANNEL  - ANALYTIC SOLUTION
 3 = ARBITRARY CHANNEL - NUMERICAL SOLUTION
3

 CHOOSE THE TYPE OF CALCULATION TO BE DONE
 1 = TRAJECTORIES FROM AN INSTANTANEOUS SOURCE
 2 = POSITIONS OF IONS FROM A TIME DEPENDENT SOURCE
 3 = RADIAL DISTRIBUTION OF IONS AT FIXED Z POSITION
1

 INITIAL ION ENERGY(MEV) AND DE / DT(MEV/SEC) IF A RAMP IS DESIRED
40,0

 ION CHARGE STATE AND ATOMIC WEIGHT(AMU)
3,7

 CHANNEL RADIUS(CM) LENGTH(CM) AND EITHER CURRENT(AMPS) OR B-ZERO(GAUSS)
PUT 0.0 IN THE ONE NOT CHOSEN
.6,500,45E3,0

 NUMBER OF IONS IN THE SOURCE DISTRIBUTION
FOCAL SPOT RADIUS(CM) IS FWHM OF A GAUSSIAN DISTRIBUTION
MAXIMUM DIVERGENCE ANGLE(RAD) IS MAXIMUM OF A UNIFORM DISTRIBUTION
5,.3,.089

 MAXIMUM TIME TO RUN THE PROBLEM AND NUMBER OF TIMES TO EVALUATE
30E-9,1000

 R-MAX AND Z-MIN AND Z-MAX PLOT DIMENSIONS.  IF SET
TO ZERO THEN THE CHANNEL RADIUS AND LENGTH ARE USED
0,0,100

 TYPE OF CHANNEL.....................   ARBITRARY
 TYPE OF CALCULATION.................TRAJECTORIES
 ION CHARGE..........................       3.000
 ION ATOMIC WEIGHT...................       7.000
 ION ENERGY(MEV).....................      40.000
 ION VELOCITY(CM/SEC)................  3.3087+009
 NUMBER OF ION TRAJECTORIES..........           5
 ION SOURCE FOCAL RADIUS(CM).........  3.0000-001
 ION SOURCE MAXIMUM DIVERGENCE(RAD)..  8.9000-002
 CHANNEL RADIUS(CM)..................       .600
 CHANNEL LENGTH(CM)..................     500.000
 CHANNEL CURRENT(STATAMPS)...........  1.3500+014
 MAXIMUM MAGNETIC FIELD(GAUSS).......  1.5011+004
 MAXIMUM TIME TO PLOT TRAJECTORY(SEC)  3.0000-008
 NUMBER OF TIMES TO EVALUATE TRAJ....       10000
 TIMESTEP FOR TRAJECTORY CALC........  3.0000-012

 WHAT TYPE OF CHANNEL CALCULATION DO YOU WANT?
 0 = STOP THE CALCULATION
 1 = STRAIGHT CHANNEL - ANALYTIC SOLUTION
 2 = TAPERED CHANNEL  - ANALYTIC SOLUTION
 3 = ARBITRARY CHANNEL - NUMERICAL SOLUTION
0
  ALL DONE
```

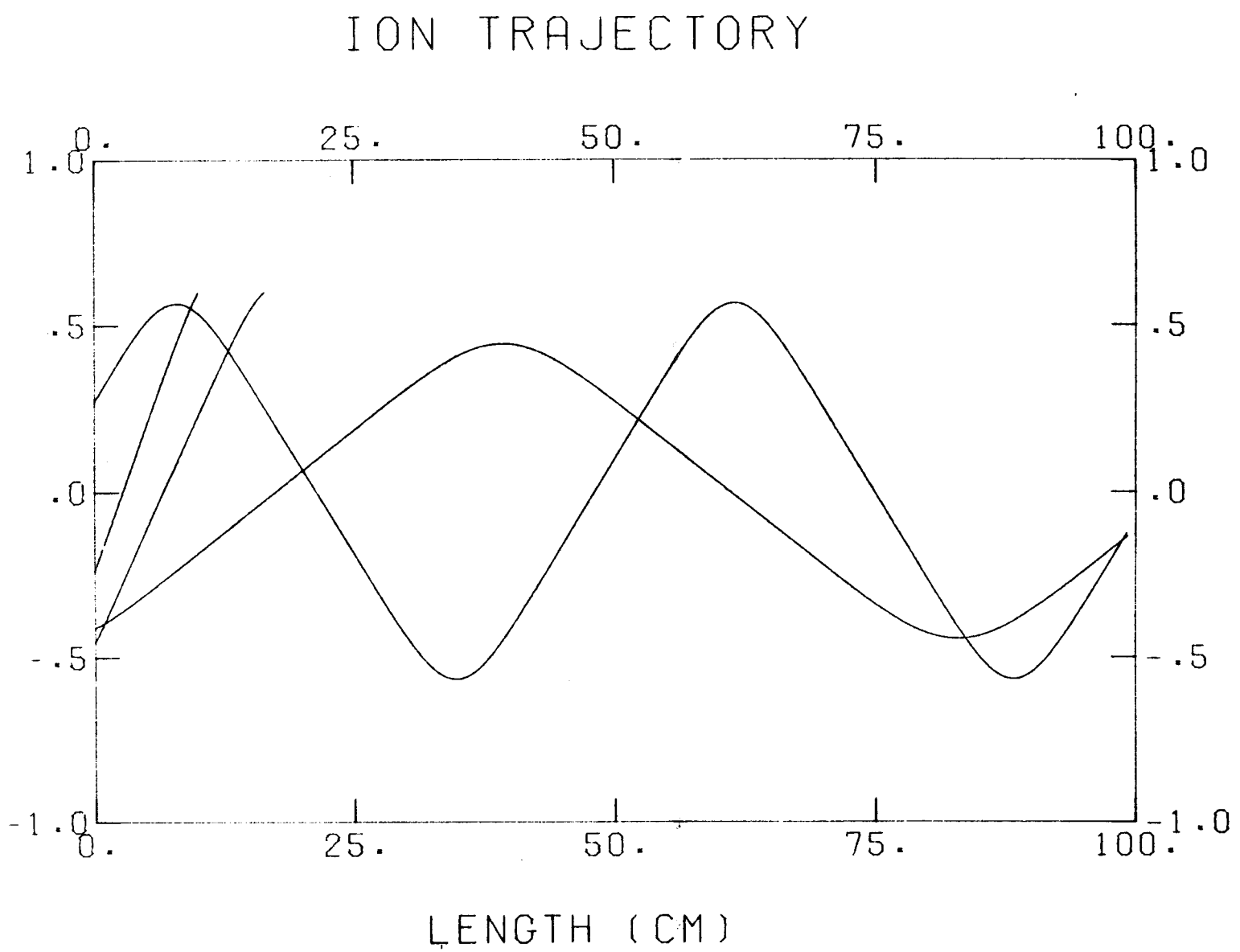

Fig. 2.20. Ion orbits in a channel with a surface current.

calculated by the code. Also, the optimum density for minimum energy loss is calculated while it was not in the earlier version.

The earlier work done on the WINDOW code[8] followed the formalism laid down in a series of articles written by researchers at NRL.[9-14] This work has provided limits on the beam power that may be transported down a plasma channel as functions of the many channel and beam parameters, most importantly the maximum angle of injection of ions into the channel. These power limits are derived from considerations of the growth of electrostatic microturbulence (ES), beam current filamentation (BFIL), channel current filamentation (CFIL), the avoidance of excessive magnetohydrodynamic motion of the channel during beam propagation (MHD) and beam energy loss in the channel (ELOSS).

For the present, the limits on beam power due to ES, BFIL, CFIL, and MHD are taken from the earlier work. Thus,

$$P_{ES} = 1.6 \times 10^{-3}[x^6(r_b)^8(\lambda_{ei})^4R^{12}/\{(Z_b)^{26}(\tau_b)^3F^{12}\}]^{1/7} \frac{\bar{E}^3}{(A_b)^{1/2}} , \quad (1)$$

$$(R/F)_{BFIL} = 2.5 \times 10^{-2} [(\lambda_{ei})^4(\bar{E})^2/\{(A_b)^6(Z_b)^8\}]^{1/8} , \quad (2)$$

$$P_{CFIL} = \{1.76 \times 10^5(x)^2(R)^4/F^4\}\{(\bar{E})^{14}(\tau_b)^2(A_b)^4/(Z_b)^{20}\}^{1/6} , \quad (3)$$

and $$P_{MHD} = 1.5 \times 10^{-21}(x)^2(r_b)^4(\bar{E})^2/\{(\tau_b)^3(Z_b)^2(A_b)\} \quad (4)$$

are also used in the present formalism. In these equations, the power per channel P is in TW, x is the ratio of the channel gas density to the optimum density and r_b is the channel radius in cm. R is the diameter of the diode in cm, F is the focal length of the diode in cm and λ_{ei} is the Coulomb logarithm,

$$\lambda_{ei} = 24 - \ln[(10^2\ Rr_b/FA_b)(\bar{E}^9x^2/\{(Z_b)^{10}P^3(\tau_b)^3\})^{1/4}] . \quad (5)$$

Z_b is the charge state of the beams ions in units of electronic charge, A_b is the ion mass in amu and τ_b is the pulse width of the beam before bunching in seconds. $\bar{E}$ is the average ion energy in the beam in MeV.

The bunching of the beam to compress the power through pulse width shorting is dependent on the waveform of the diode voltage and the length of the channel. The bunching factor and the energy spread of the beam are used

explicitly in an expression for the channel length. In the earlier work, values for these were assumed and the choice of channel length was removed. The channel length and the bunching factor must now be provided by the user and the energy spread is calculated by the code.

The diode voltage may be ramped to bunch the beam while it is in the channel. The ideal diode voltage waveform is

$$\phi(t) = \phi_o(1 - t/\tau_t)^{-2} \quad . \tag{6}$$

This leads to a velocity of ions leaving the diode which is also ramped

$$v_i(t) = v_i(t=0)(1 - t/\tau_t)^{-1} \quad . \tag{7}$$

The length which is required for the pulse to converge by a factor of α is[4]

$$L = 1.3 \times 10^9 \ (1 - \frac{1}{\alpha})(\tau_t - \tau_b)(\frac{E(\tau_b)}{A_b})^{1/2} \text{ cm} \quad . \tag{8}$$

$E(\tau_b)$ is the final ion energy at the end of the pulse in MeV and τ_b is the initial duration of the pulse.

From Eq. (7), one can find τ_t in terms of the voltage spread between the end and beginning of the pulse

$$\frac{\phi(\tau_b)}{\phi(0)} = \frac{1}{(1 - \frac{\tau_b}{\tau_t})^2} \quad , \tag{9}$$

which converts to

$$\tau_t = \tau_b\left(\frac{1}{1 - \frac{1}{(1 + \delta)^{1/2}}}\right) \tag{10}$$

if one expresses the energy spread of the beam as

$$\phi(\tau_b) \equiv \phi(0)(1 + \delta) \quad . \tag{11}$$

Thus the channel length L can be written in terms of α, δ and τ_b with Eqs. (8) and (10),

$$L = 1.3 \times 10^9 \left(1 - \frac{1}{\alpha}\right) \tau_b \frac{\bar{E}^{1/2}}{A_b^{1/2}} \left(\frac{(1 + \frac{\delta}{2})^{1/2}}{(1 + \delta)^{1/2} - 1}\right) \quad \text{cm} . \tag{12}$$

While the ion beam is propagating through the plasma channel, it will lose some of its energy. The energy loss consists of a collisional slowing down component and a loss due to work done by the beam ions against an axial electric field.[10,11] This electric field has an ohmic term and an inductive term proportional to the inverse of the channel gas density. The inductive part of the axial electric field is due to the radial hydrodynamic motion of the channel and the azimuthal magnetic field of the channel. We will neglect the ohmic contribution to the axial electric field. The collisional energy loss is proportional to the channel gas density. Because of the inverted dependence on the plasma density of the collisional and inductive terms, there is an optimum density where the energy loss is a minimum.[11] For a deuterium gas, the optimum channel plasma density is

$$\rho_{opt} = 0.167\ E^{1/2} p^{1/2} (\tau_b)^{1/2} (\theta_m)^2 / \{(r_b)^2 Z_b\} \tag{13}$$

where θ_m is the maximum angle at which ions are injected into the channel and is equal to R/F for most cases of interest. This equation depends on an expression for the radial expansion of the plasma channel which was derived for a deuterium channel.[9] This equation and those that follow dealing with the energy loss are only strictly valid for deuterium.

With the help of expressions found in Refs. 10 and 11, the fractional energy loss for the beam ions can be written as

$$f_E = \frac{1.7 \times 10^2 (x + 1/x)\ A_b \theta_m^2 Z_b^{1/2} I_b^{1/2} \tau_b^{1/2} L}{\bar{E} r_b^2} \tag{14}$$

where I_b is the beam ion current. There is a strong dependence on f_E of θ_m because the main energy loss mechanism occurs through a $v_r \times B_\theta$ force on the beam ions. B_θ is the confining field, whose required magnitude is $\propto \theta_m^2$. One can invert this expression and find the power limit on the beam due to energy loss,

$$P_{ELOSS} = \frac{I_b \bar{E}}{Z_b} = \frac{3.5 \times 10^{-5} f_E^2 \bar{E}^3 r_b^4}{(x + 1/x)^2 A_b^2 Z_b^2 \tau_b L^2 \theta_m^4} . \quad (15)$$

The WINDOW computer code uses the theory outlined above to study the constraints on the propagation of an ion beam in a plasma channel. The code calculates the limits on the beam power per channel for a range of R/F. The optimum mass density of the gas in the channel is also found at the maximum allowable beam power as a function of R/F. Results are both printed out and are stored in files for plotting. WINDOW is written in FORTRAN 77, is 199 lines long including comments, and requires 51 kilobytes of memory on an IBM personal computer for just the executable code.

The WINDOW computer code can be used to find that region of beam power per channel versus R/F space where ion beam propagation is possible from the points of view of ES, CFIL, BFIL, MHD, and ELOSS. The power limits due to these five constraints are shown plotted against R/F in Fig. 2.21 for the base case light ion fusion reactor design specified in Table 2.2. The cross-hatched region is where all of these constraints are met. One can see that the optimum value for R/F is 0.06 radians and the maximum power per channel is roughly 2.5 TW. This means that about 44 such channels would be required to transport the needed 240 TW to the target when one considers the power compression due to bunching and the energy lost during transport in the channel.

The WINDOW code can also be used to study the interrelations between the parameters governing bunching of the beam. The fractional energy spread is shown in Fig. 2.22, plotted against the channel length for a few values of the power compression factor, α. The base case parameters of a 10 m channel length and a 3-fold power compression yield a fractional energy spread of 0.2. There is a minimum achievable fractional energy spread for today's diodes somewhere around 0.1 that puts an upper limit on the channel length. One can see that at moderate and large channel lengths the fractional energy spread, δ, has only a rather weak dependence on the power compression factor, α.

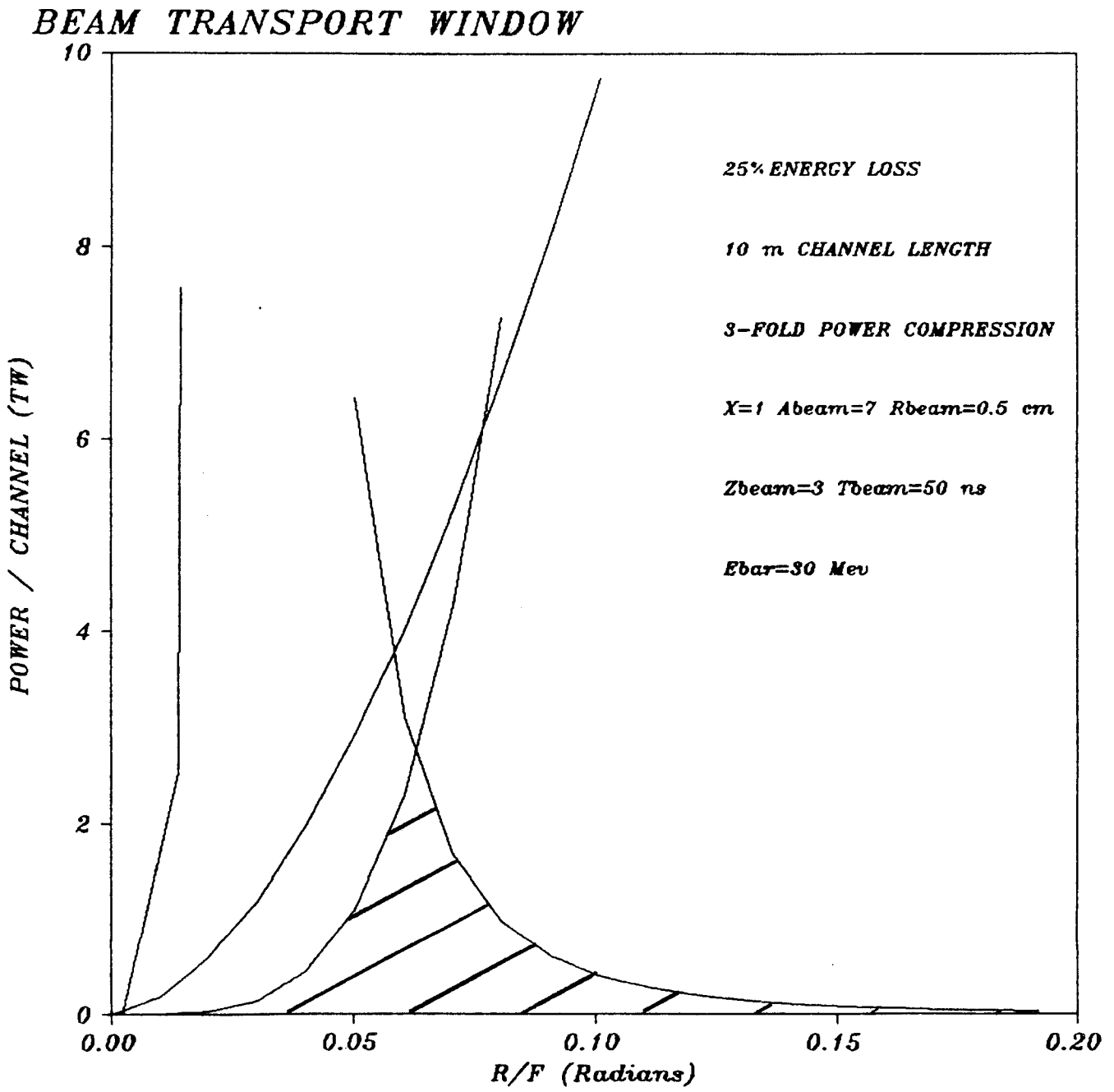

Fig. 2.21. Power limit window for base case parameters.

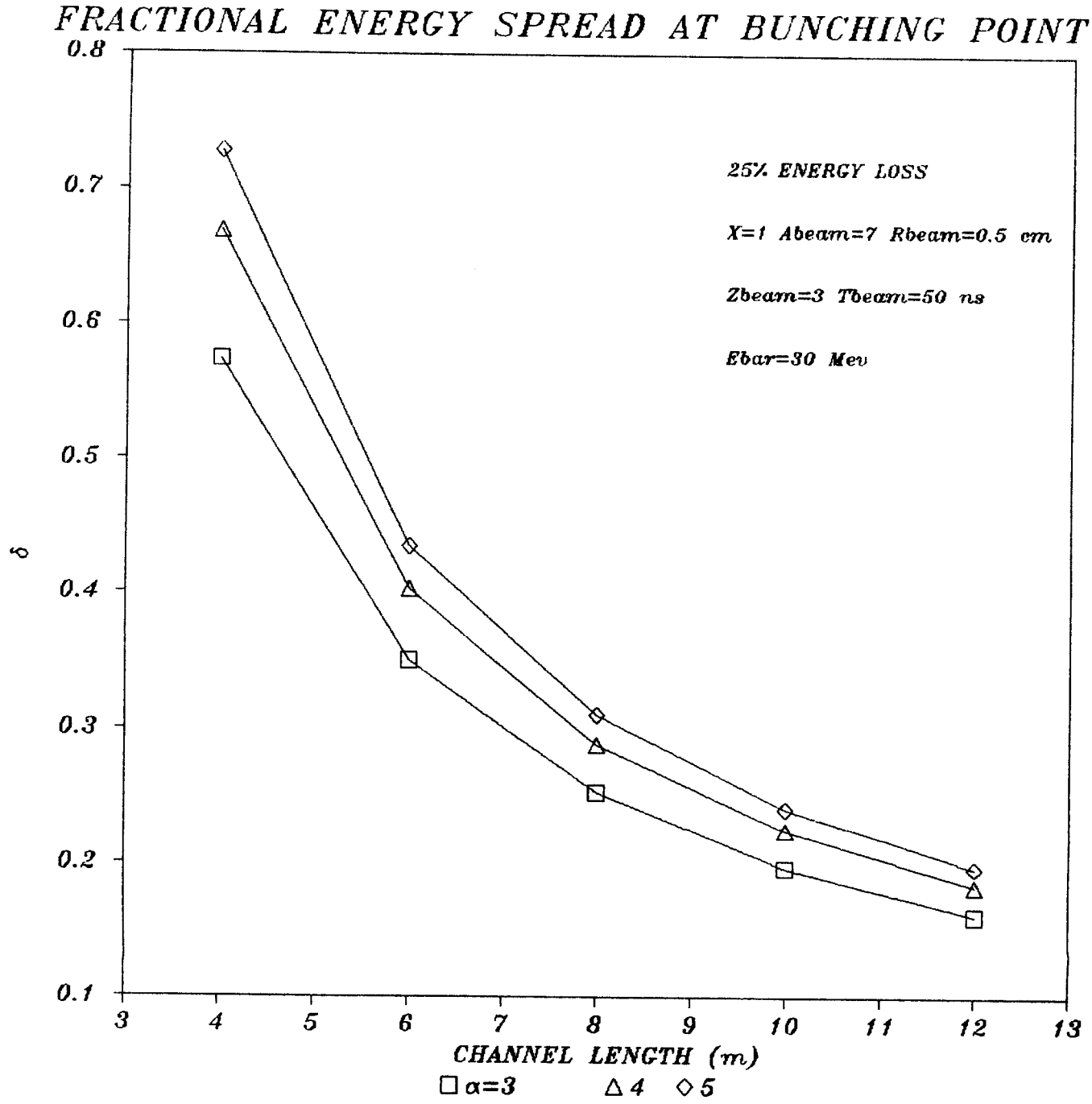

Fig. 2.22. Fractional energy spread vs. channel length for different bunching factors.

Table 2.2. Base Case Reactor Design Channel Parameters

Channel Length (cm)	1000
Channel Radius (cm)	0.5
Ratio of Channel Density to Optimum Density	1.0
Average Beam Ion Energy (MeV)	30
Fractional Energy Spread	0.2
Power Compression Factor	3.0
Ion Type	Li^{+3}
Beam Pulse Width at Diode (ns)	50
Fractional Beam Ion Energy Loss During Transport	0.25

References for Chapter 2

1. J.J. Watrous, G.A. Moses and R.R. Peterson, "Z-PINCH - A Magnetohydrodynamic Radiative Transfer Computer Code," University of Wisconsin Fusion Engineering Program Report UWFDM-584, June 1984.

2. G.A. Moses, T.J. McCarville and R.R. Peterson, "MF-FIRE - A Multifrequency Radiative Transfer Hydrodynamics Code," University of Wisconsin Fusion Engineering Program Report UWFDM-458, December 1982.

3. R.R. Peterson and G.A. Moses, "MIXERG - An Equation of State and Opacity Computer Code," Comp. Phys. Comm. 28, 405 (1983).

4. D. Steinberg, R. Kidder and A. Cecil, "A One-Dimensional Magnetohydrodynamics Code," Lawrence Livermore National Laboratory Report UCRL-14931, June 1966.

5. D.G. Colombant and M. Lampe, "WHYRAC - A New Modular One-Dimensional Exploding Wire Code," Naval Research Laboratory Memorandum Report 3726, February 1978.

6. J. Freeman, L. Baker and D. Cook, "Plasma Channels for Intense-Light-Ion-Beam Reactors," Nucl. Fusion 22, 383 (1982).

7. P.F. Ottinger, D. Mosher, and S.A. Goldstein, "Propagation of Intense Ion Beams in Straight and Tapered z-Discharge Plasma Channels," Phys. Fluids 23, 909 (1980).

8. B. Badger et al., "Progress Report for the LIBRA Light Ion Beam Fusion Reactor Project for the Period January-June 1984," Fusion Power Associates Report FPA-84-1 (July 1984).

9. D.G. Colombant, S.A. Goldstein and D. Mosher, "Hydrodynamic Response of Plasma Channels to Propagating Ion Beams," Phys. Rev. Lett. 45, 1253 (1980).

10. D. Mosher, D.G. Colombant and S.A. Goldstein, "Beam Requirements for Light-Ion-Driven Inertial-Confinement Fusion," Comments Plasma Physics 6, 101 (1981).

11. P.F. Ottinger, S.A. Goldstein and D. Mosher, "Constraints on Transportable Ion Beam Power," Naval Research Laboratory Memorandum Report 4948 (November 1982).

3. ION TRANSPORT CALCULATIONS

The design of a self-consistent power flow consisting of: (1) pulsed power machinery, (2) ion diodes, (3) plasma channels, and (4) light ion beam driven target for LIBRA involves many "free" parameters and many constraints that help to define the allowable operating range of these parameters. In July 1984 WINDOW calculations were reported[1] that followed the pulsed power designs of Ian Smith[2] but did not include self-consistent diode-channel coupling. These calculations are summarized in Table 3.1. During the summer of 1984 private discussions with W. Schmidt[3] and others at KfK led to the realization that the allowable diode geometry vis a vis the maximum entrance angle of the ions into the channel and the maximum allowable anode current density could severely limit the window in parameter space where acceptable ion propagation could be achieved. An exhaustive parametric study could be done to determine the operating range of all of the important parameters in the system. This has not been done. Instead, specific values for a few important parameters were selected and all other parameters were adjusted to accommodate the self-consistency constraint. To be specific, we assume that the ions are either 30 MeV Li^{+1} or 15 MeV D^{+1} and that 240 TW are delivered to the target. The 30 MeV Li ion is appropriate for target designs currently being investigated at Sandia National Laboratory while the 15 MeV D ion has a range that makes it suitable for driving the "HIBALL-type" targets that are studied at Kernforschungszentrum Karlsruhe. Furthermore, the pulsed power equipment necessary for generating these two driving voltages was analyzed by Ian Smith and reported in Ref. 2. Following the results of Smith we assume that the channel length is 10 meters in all cases and that the ion transport efficiency is 75%. This power loss is completely attributed to ion energy loss in our calculations. Again following Ref. 2 we assume that there are 18 modules and hence 18 channels for the 30 MeV Li cases and 24 channels for the 15 MeV D cases. In all cases we assume that a 3:1 bunching factor reduces the pulse length from 50 ns to 17 ns. Hence the power at the diodes must be 107 TW. The anode current density in the diode is chosen to be 5 kA/cm^2 and 1 kA/cm^2 to form four different cases:

Table 3.1. Propagation of Ions in Plasma Channels

Case #	1	2	3	4	5	6
Ion species	D^{+1}	D^{+1}	Li^{+3}	Li^{+3}	Li^{+3}	Li^{+3}
Particle energy (MeV)	15	15	30	30	64	64
Pulse width at diode (ns)	50	17	50	17	50	17
Pulse width at target (ns)	17	17	17	17	17	17
Optimum beam divergence (radians)	0.11	0.135	0.09	0.13	0.09	0.125
Maximum power per channel at diode (TW)	15	125	3	20	18	140
Proposed power per channel at diode (TW)	5	14	6	19	19.2	32
Proposed power per channel at target (TW)	10	10	13.5	13.5	41.6	24
Proposed # of channels	27	27	18	18	6	10

---

(1) 30 MeV Li, 5 kA/cm^2
(2) 30 MeV Li, 1 kA/cm^2
(3) 15 MeV D, 5 kA/cm^2
(4) 15 MeV D, 1 kA/cm^2 .

Case 1 20 MeV Li - 5 kA/cm^2 Anode Current Density

In this first case we will investigate the diode and channel parameters for 30 MeV Li ions using diodes with a current density of 5 kA/cm^2. The 30 MeV Li ion is the choice of Sandia National Laboratory for driving hohlraum targets. The 5 kA/cm^2 current density is state-of-the-art for single shot diodes. There is a significant uncertainty whether a rep rateable diode could operate at this high current density. The power to be delivered to the target is 240 TW and there is a 75% transport efficiency assumed. We assume that there is a bunching factor in the channel of 3:1, hence the power that must be delivered into the channel by the diodes is

$$P_{Diodes} = \frac{240}{(0.75)(3)} = 107 \text{ TW} .$$

Following the work of Ian Smith[2] we assume there are 18 pulsed power modules and hence 18 diodes and channels. We assume the channel length to be 10 meters in accordance with Smith's design of the pulsed power equipment. This allows the 18 modules to be placed around the reactor vessel all on the same level. The pulse length at the diode is assumed to be 50 ns, again to be consistent with Smith's work. For 107 TW delivered into 18 channels we are required to transport 6 TW/channel. Using the WINDOW calculations of Peterson (Figs. 3.1-3.10) we find that the power per channel is limited by the radius and a radius of about 0.8 cm is required to allow stable transport of 6 TW. The maximum injection angle is limited to 0.071 radians (using Figs. 3.1 and 3.2). If the ions are focused to a spot size of 0.4 cm (HWHM) then a channel current of 27.5 kA and a corresponding maximum magnetic field of 6.9 kG are required to confine the ions, using

$$I_c(A) = 1.57 \times 10^7 \frac{A}{Z} \beta(1 - r_s^2/r_c^2)^{-1} \alpha_m^2$$

$$B_c(G) = 3.14 \times 10^6 \frac{A}{Z} \frac{\beta}{r_c} (1 - r_s^2/r_c^2)^{-1} \alpha_m^2$$

where $\beta = 0.1$ for 30 MeV Li. This channel radius is larger than the anticipated radius of the target, which is about 0.5 cm. However, little can be done about this unless more channels and hence more modules are used. The alternative is to taper the channel or actively focus at the target. If the channel is somewhat tapered as shown in Fig. 3.11 then the results of ION calculations show that the ions can be radially compressed into a 0.5 cm radius at a position of 10 meters down the channel, Fig. 3.12. The channel current of 27.5 kA is a reasonable value and does not represent a problem to this design.

Now we must determine diode parameters that are consistent with these channel parameters. To deliver 107 TW of 30 MeV Li^{+1} ions requires a current of 3.567 MA or 0.198 MA/diode. An allowable current density of 5 kA/cm^2 implies a diode radius of 3.55 cm using

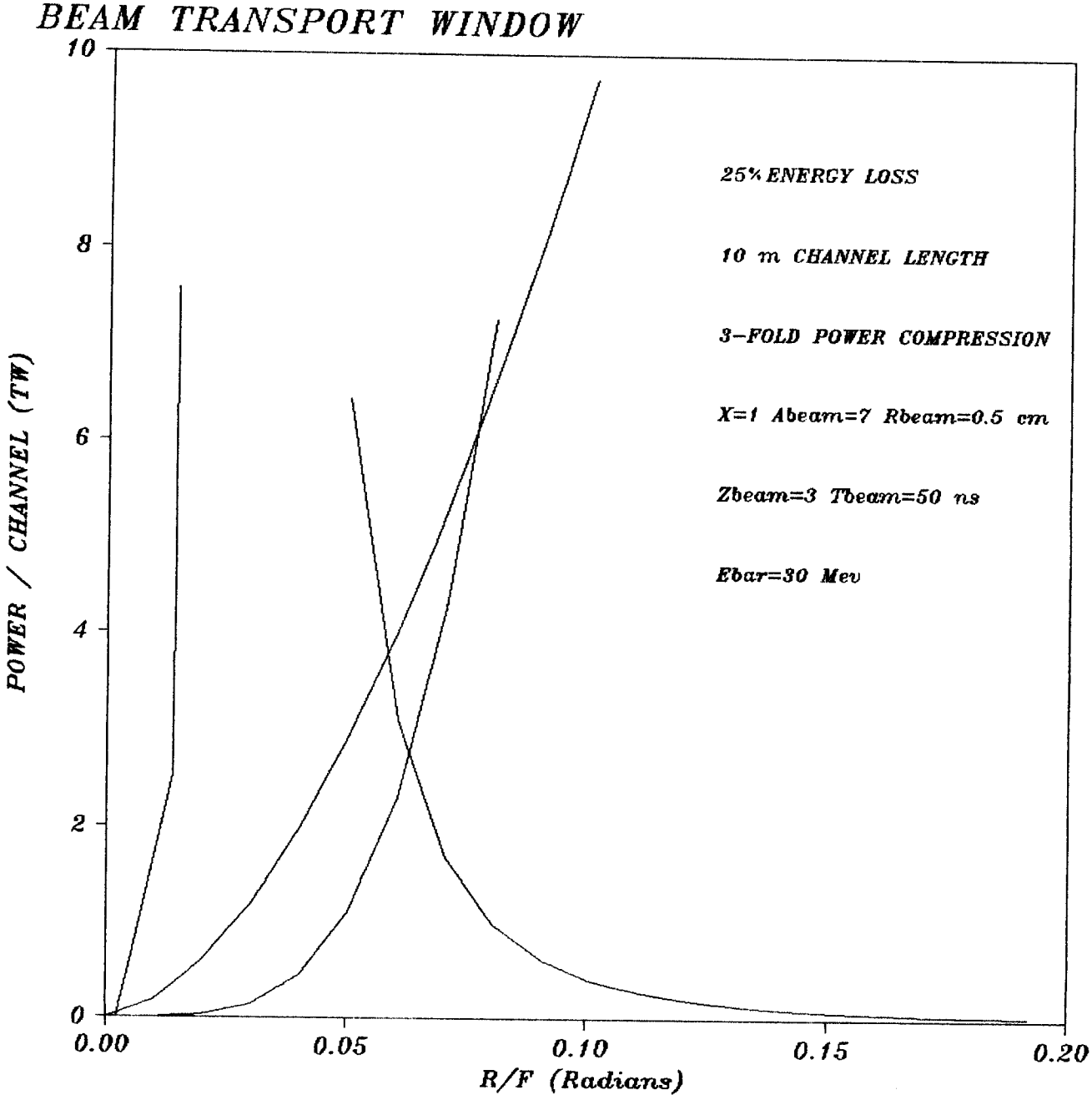

Fig. 3.1. Transportable window for 30 MeV Li, 0.5 cm channel radius.

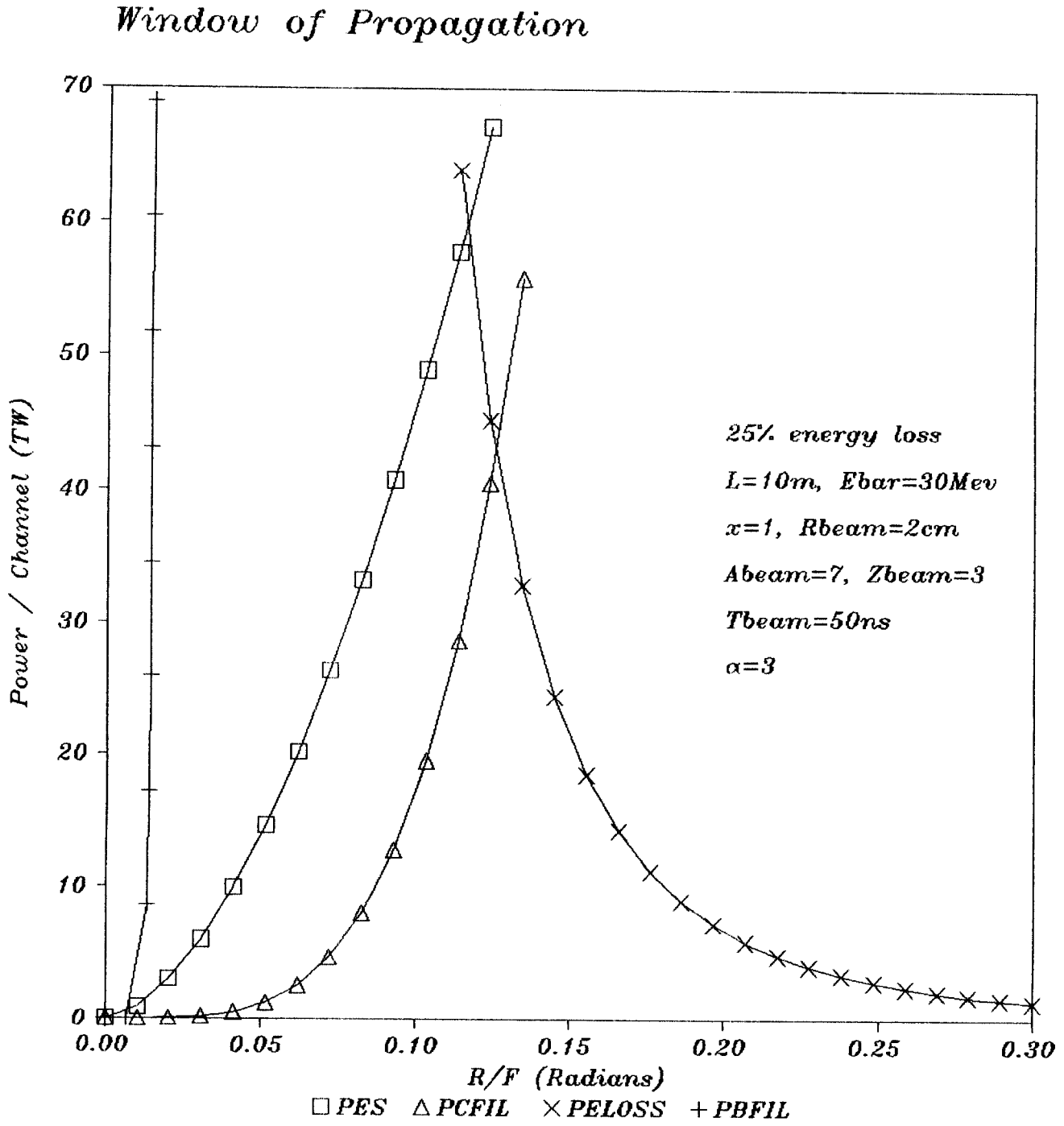

Fig. 3.2. Transportable window for 30 MeV Li, 1.0 cm channel radius.

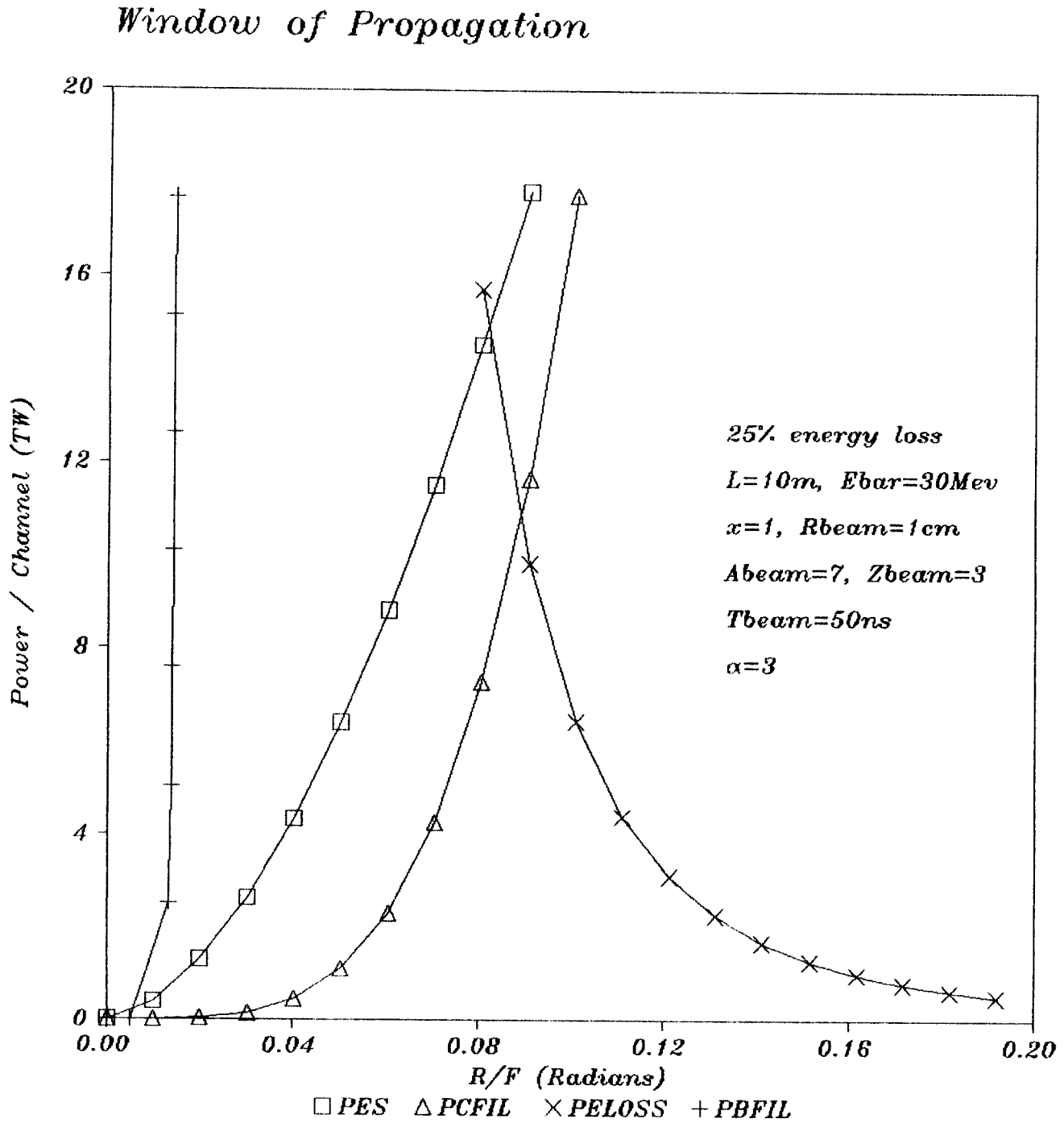

Fig. 3.3. Transportable window for 30 MeV Li, 2.0 cm channel radius.

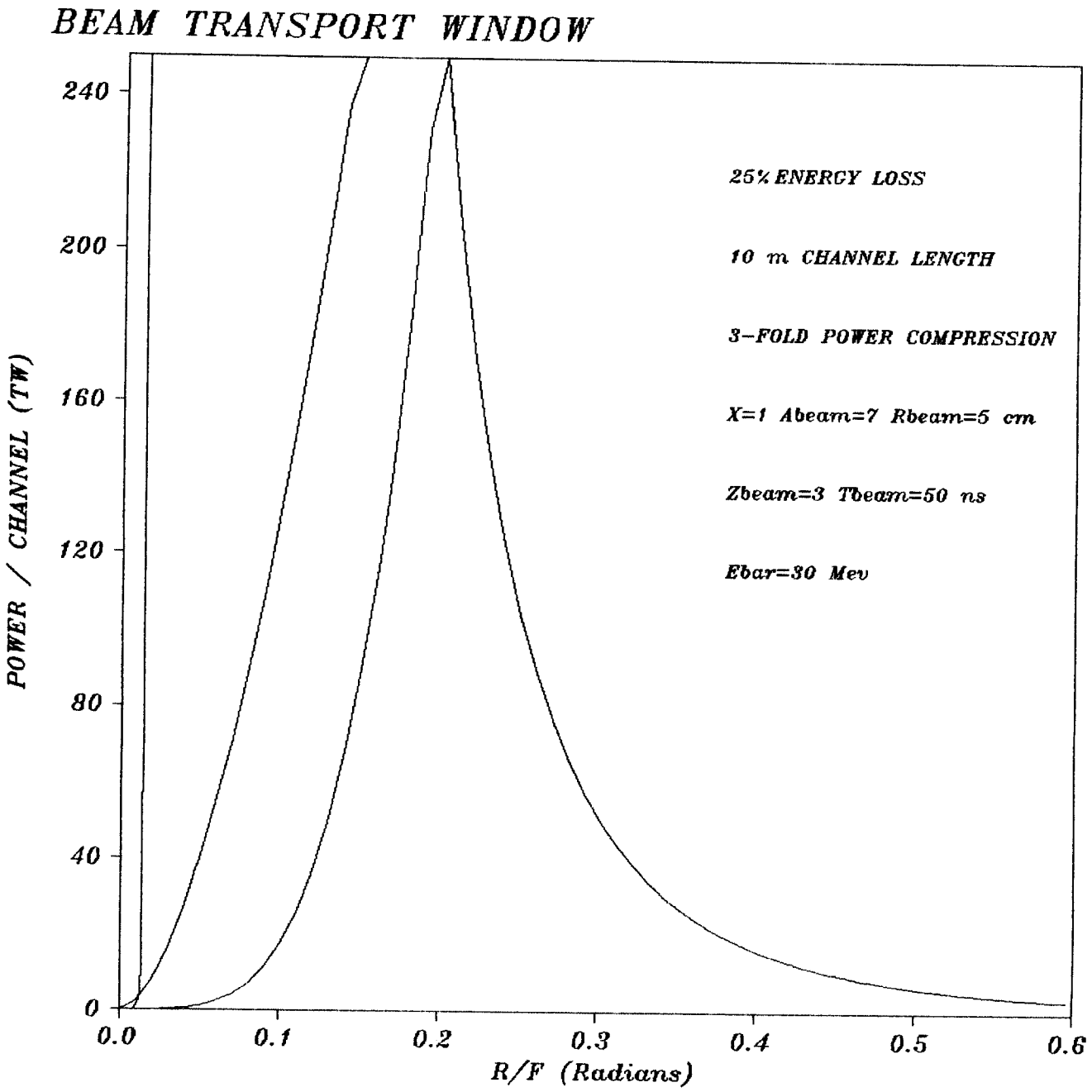

Fig. 3.4. Transportable window for 30 MeV Li, 5.0 cm channel radius.

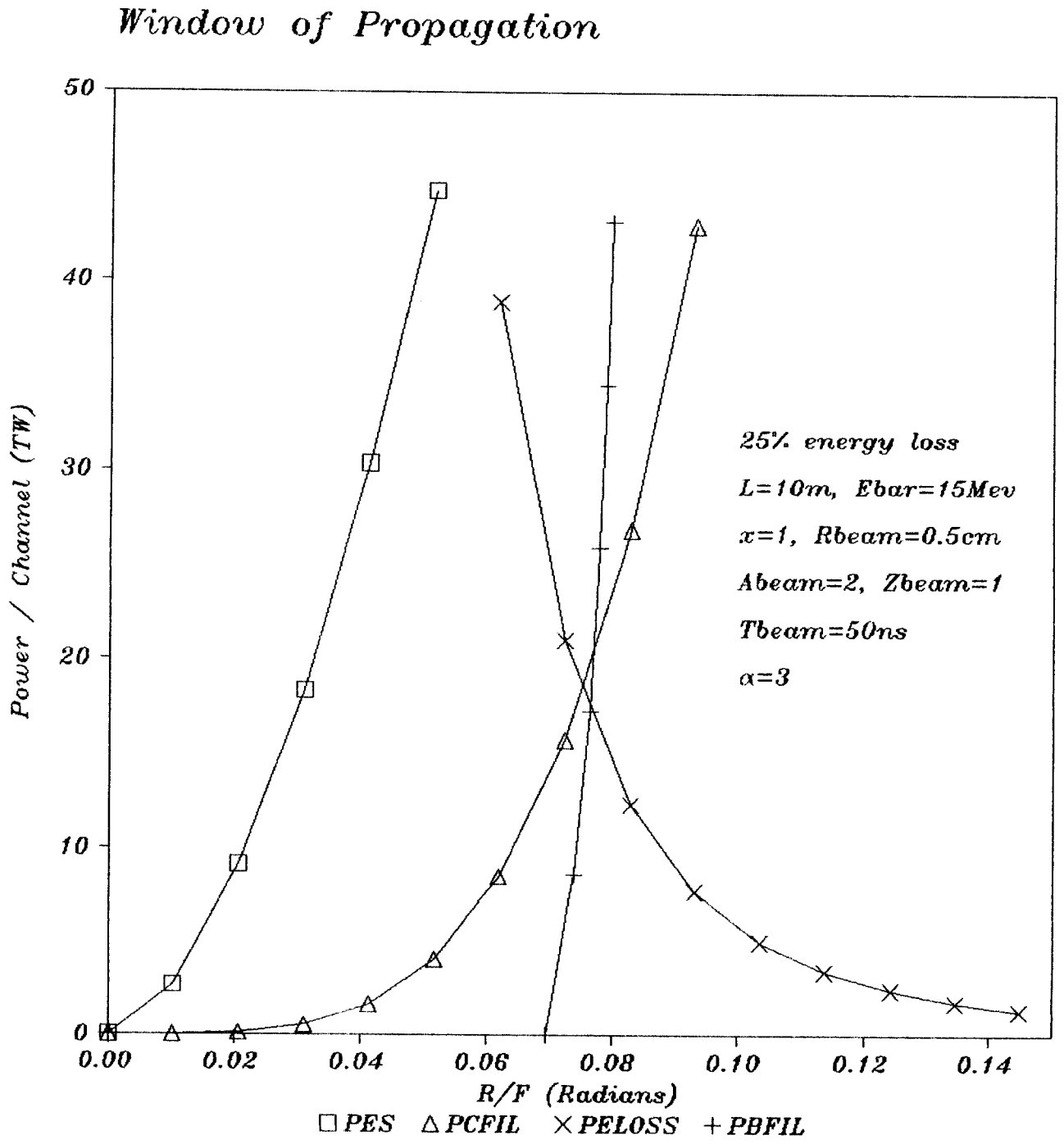

Fig. 3.5. Transportable window for 15 MeV Li, 0.5 cm channel radius.

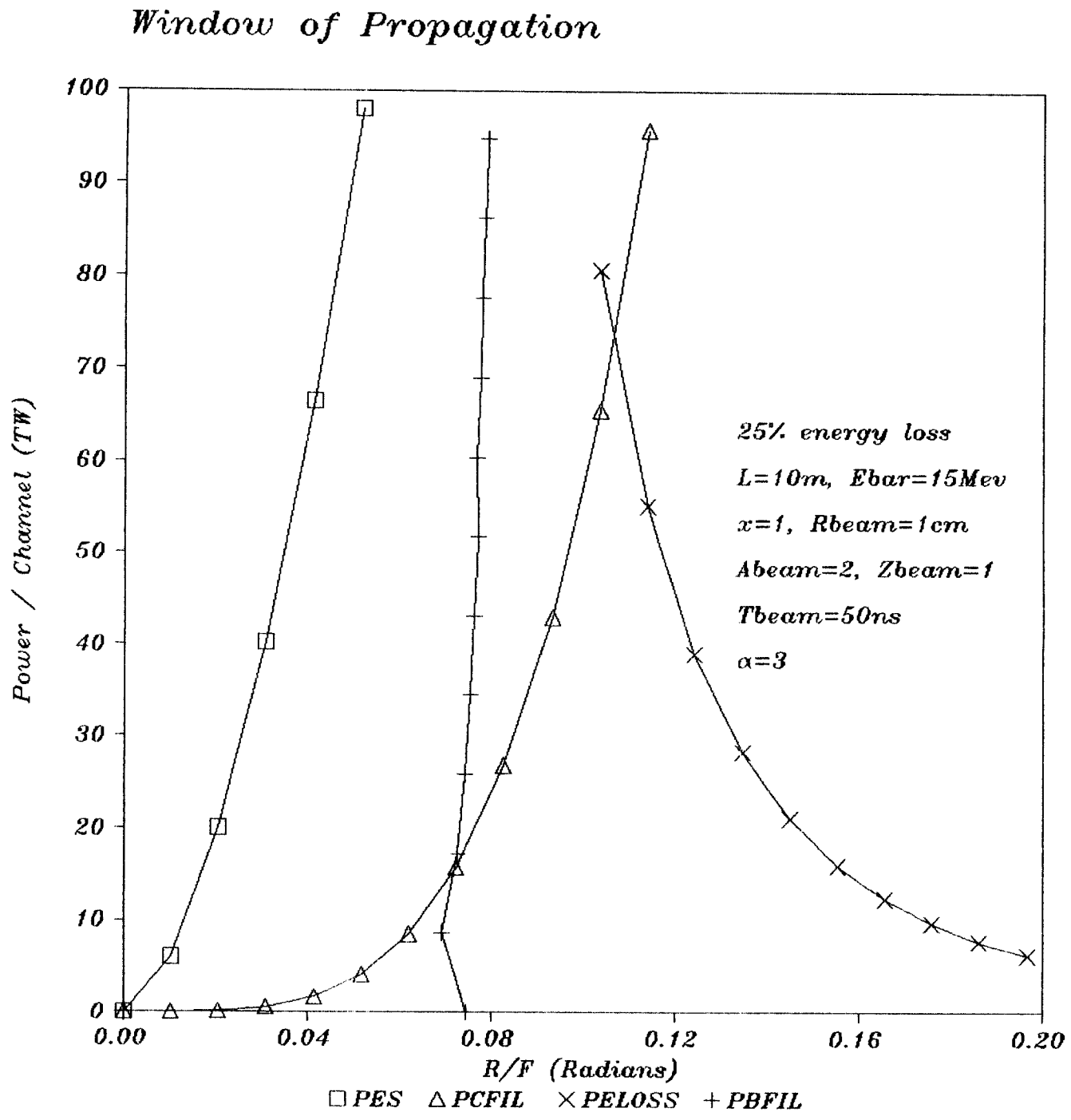

Fig. 3.6. Transportable window for 15 MeV Li, 1.0 cm channel radius.

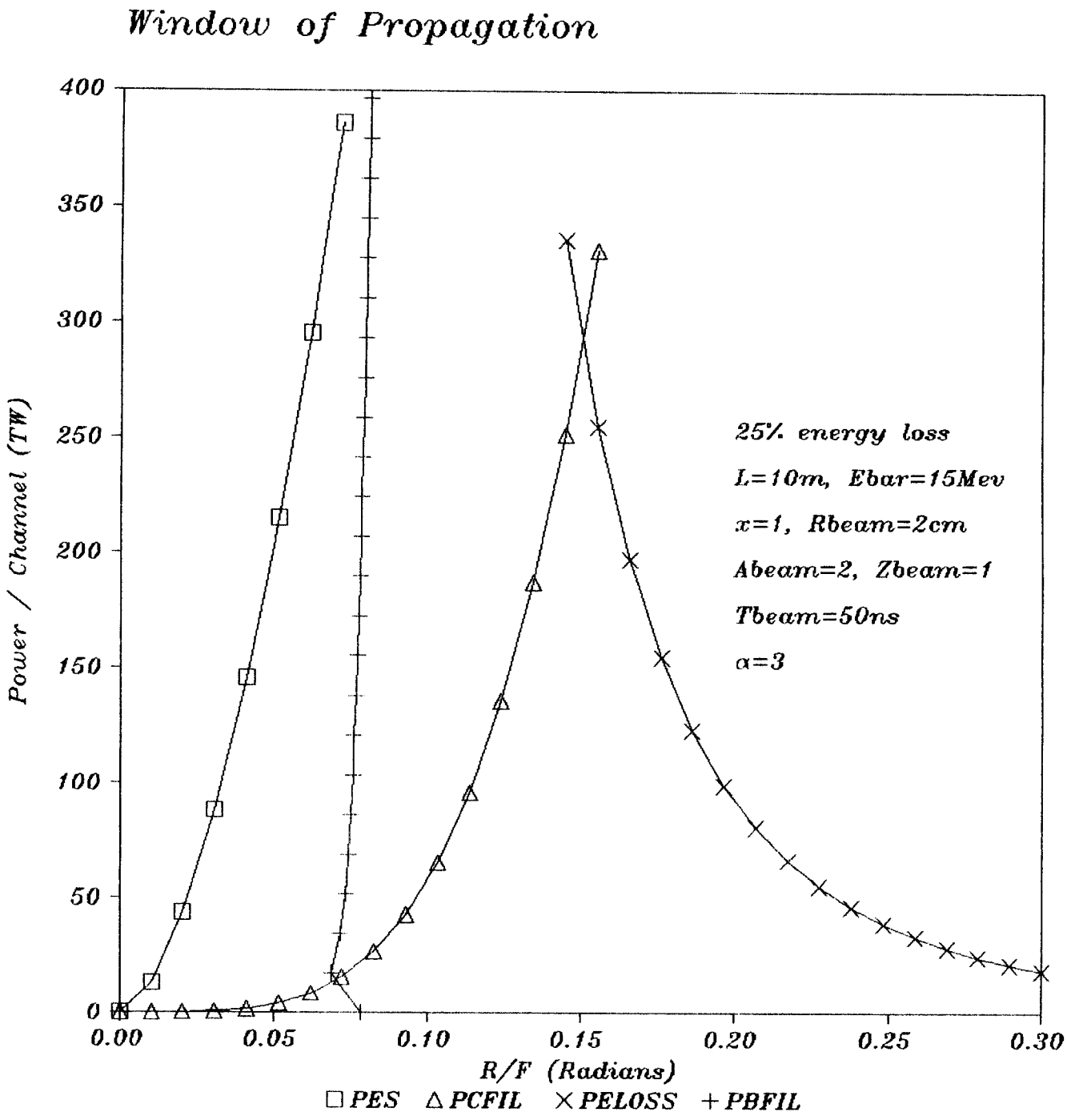

Fig. 3.7. Transportable window for 15 MeV Li, 2.0 cm channel radius.

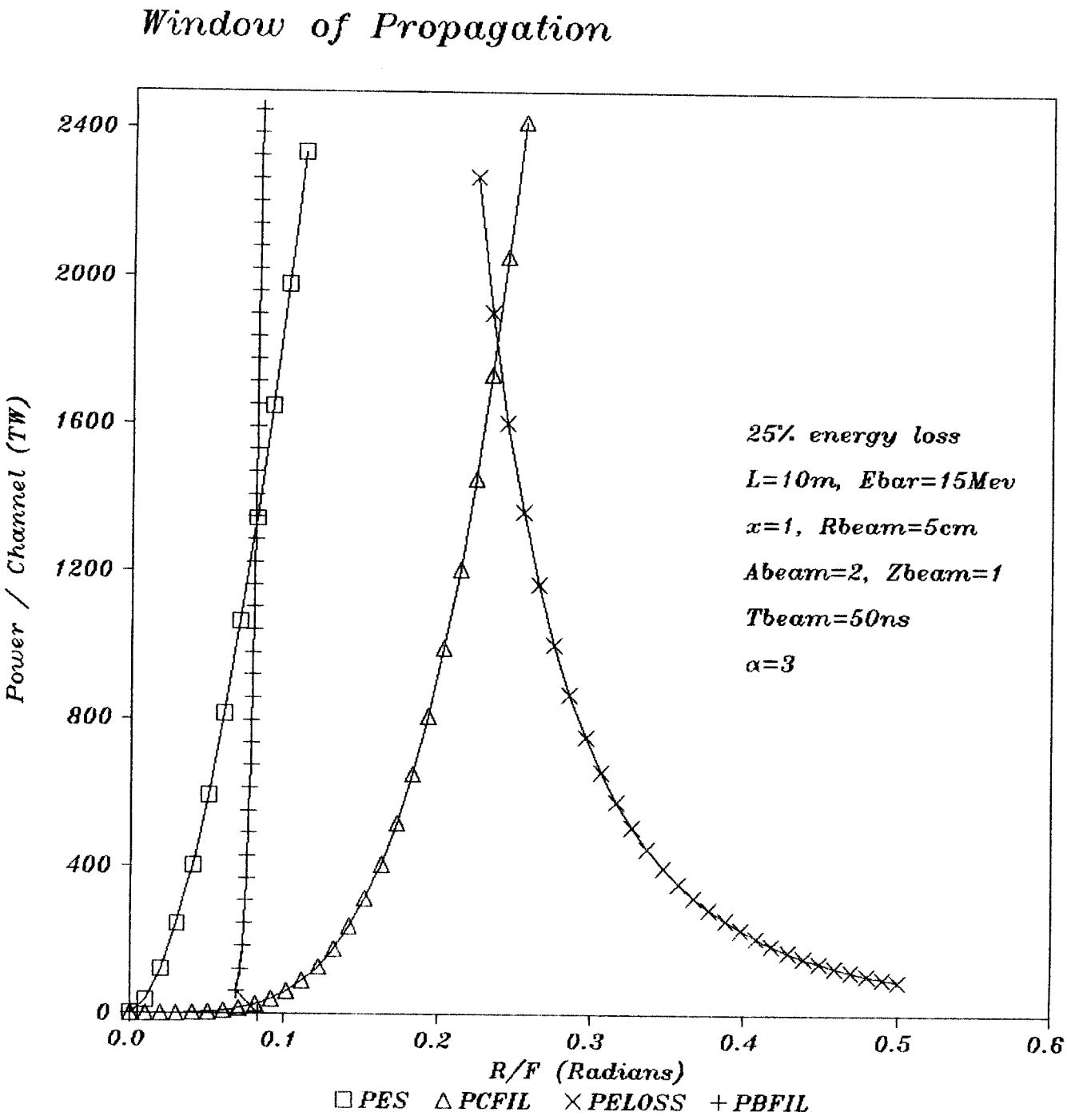

Fig. 3.8. Transportable window for 15 MeV Li, 5.0 cm channel radius.

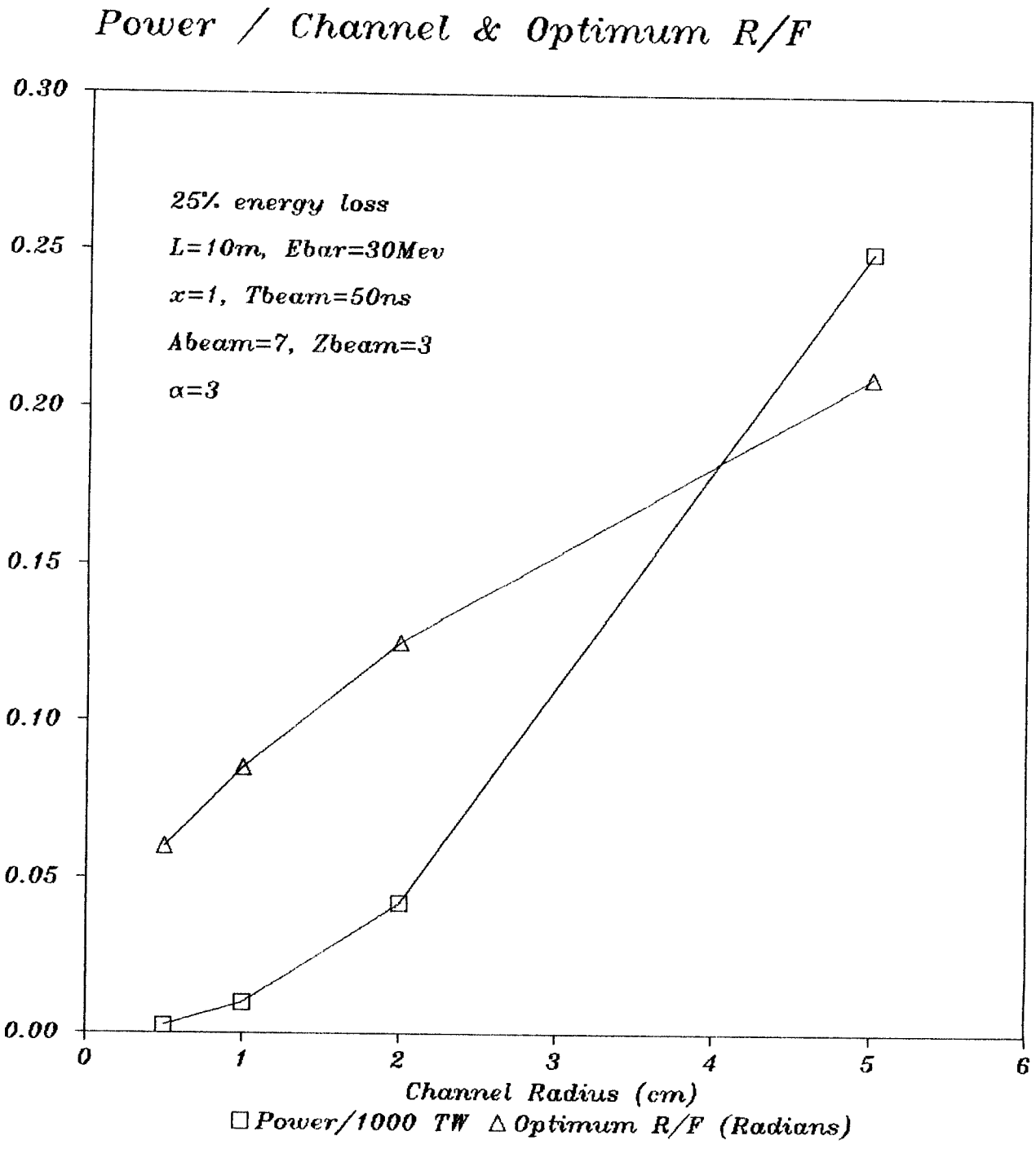

Fig. 3.9. Transportable power and optimum maximum entrance angle vs. channel radius for 30 MeV Li.

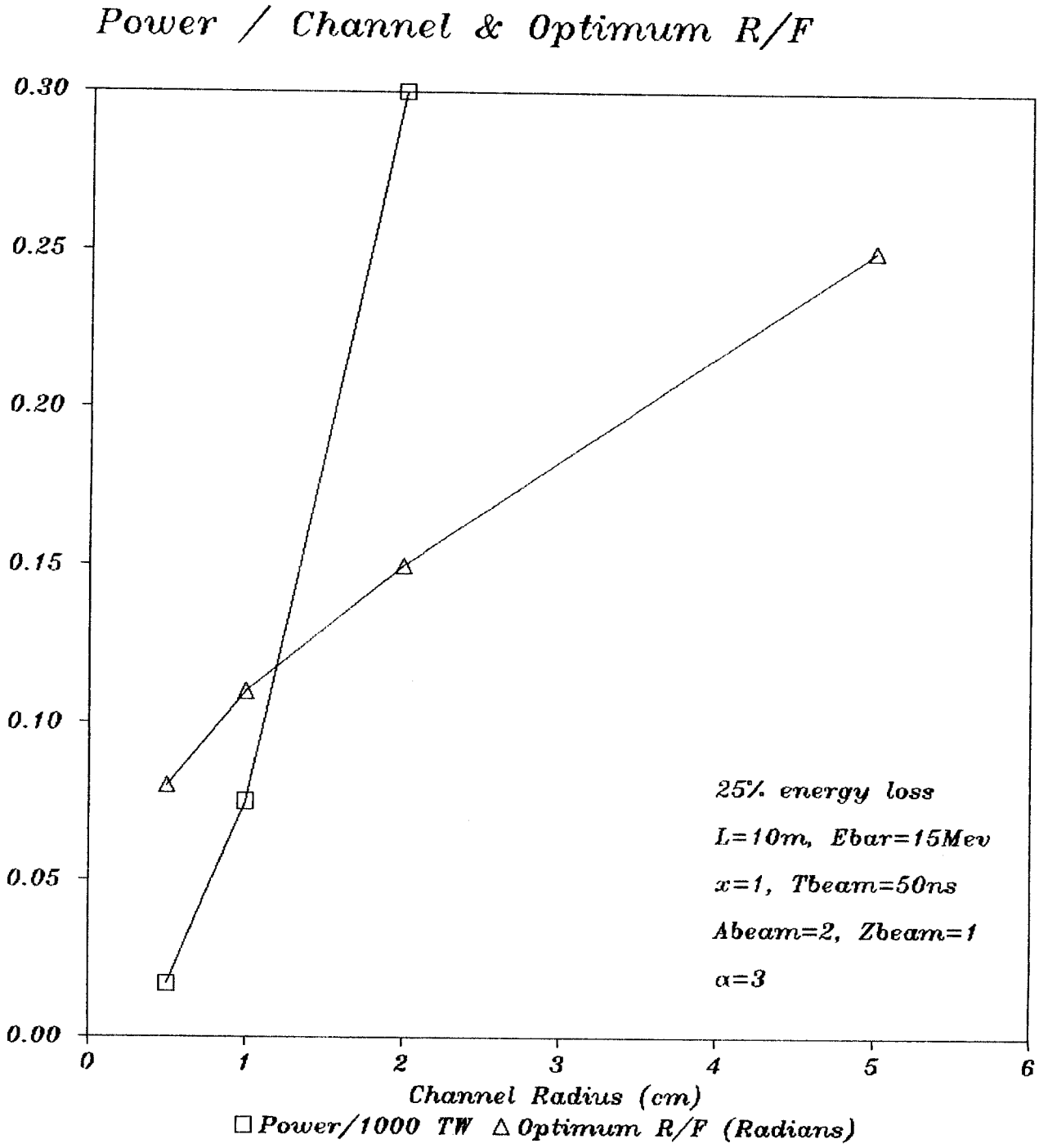

Fig. 3.10. Transportable power and optimum maximum entrance angle vs. channel radius for 15 MeV D.

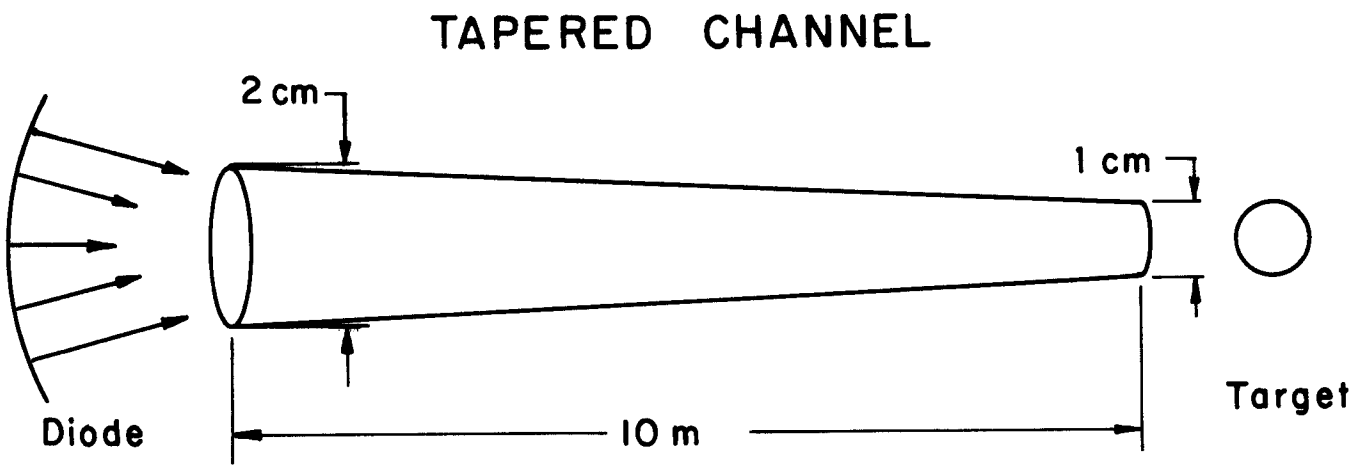

Fig. 3.11. Tapered plasma channel.

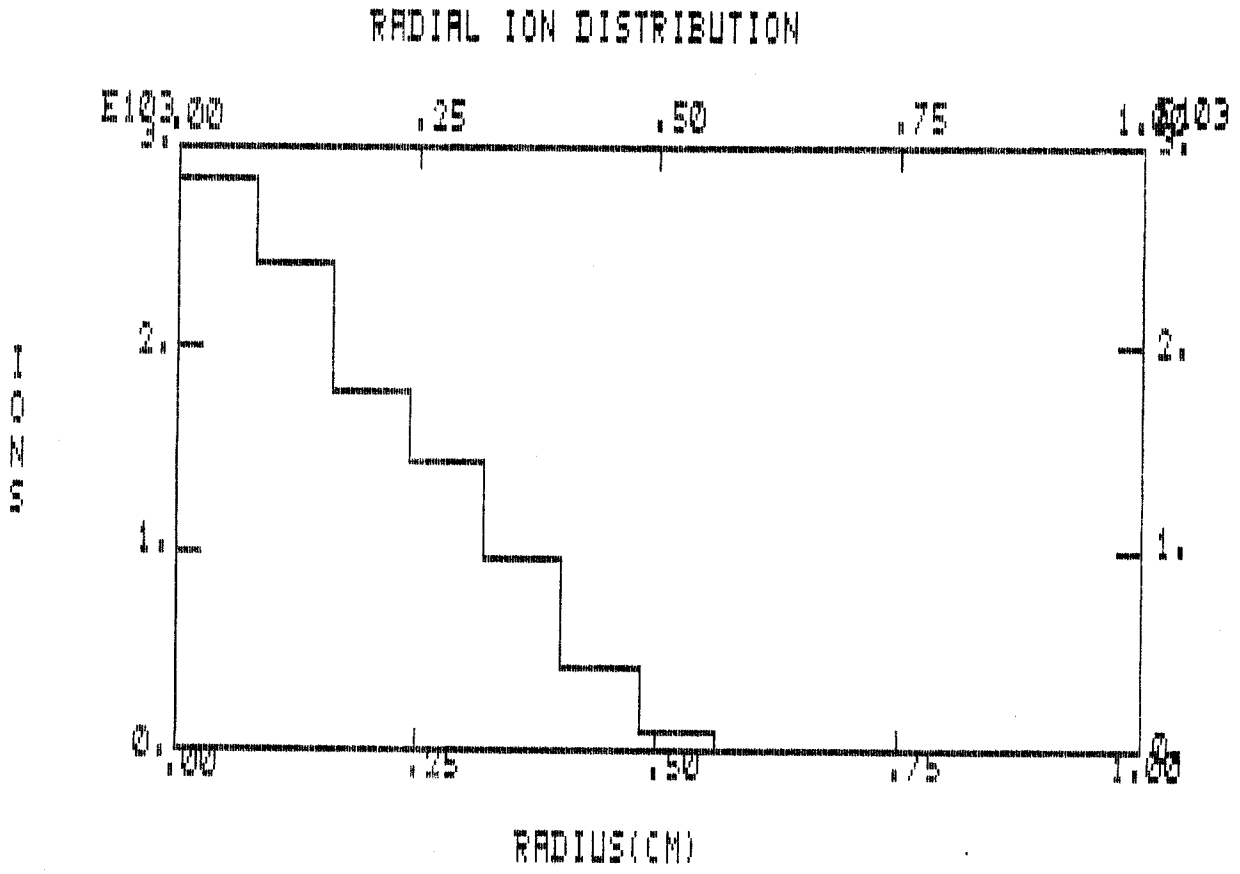

Fig. 3.12. Radial ion distribution at the target plane in a tapered channel.

$$A_{diode} = I_{diode}/J_{diode}$$

$$R_{diode} = (A_{diode}/\pi)^{1/2} .$$

To limit the entrance angle to 0.071 radians requires a focal length of F = 50 cm, using

$$R/F = \sin \alpha_m$$

with reference to Fig. 3.13. The brightness half-angle of the diode defined as (see Fig. 3.13)

$$r_s/F = \sin \theta_m$$

is therefore equal to 8 mrad. This is a reasonable value considering that 14 mrad is achievable today at much lower voltage. The drift length of 50 cm is probably manageable, but is at the upper bound of its reasonable range.

The conclusions of this analysis are that to deliver 240 TW of 30 MeV Li ions to a target through 18 plasma channels without seriously violating our current understanding of beam and channel stability requires the use of a high current density anode and a long drift region. Furthermore the channel must be tapered (by some unspecified mechanism) by a factor of 0.625 in order to focus upon a 1 cm diameter target.

Case 2 30 MeV Li - 1 kA/cm^2 Anode Current Density

In this case we will investigate the diode and channel parameters for 30 MeV Li ions using diodes with a current density of 1 kA/cm^2. This current density is degraded from the state-of-the-art to allow for potential problems associated with repetition rate. The power to be delivered to the target is again 240 TW with a 75% transport efficiency and a 3:1 bunching factor and 50 ns pulse. For 18 modules we are again required to transport 6 TW/channel. Working on the diode first we find that the anode radius must be 7.94 cm to maintain the 1 kA/cm^2 limit. If we continued to use a 50 cm drift length then the maximum injection angle would be 0.16 radians. This injection angle would require a channel current of 125 kA and a maximum magnetic field of 31 kG to confine the ions. Experiments by Olsen[4] indicate the onset of kink insta-

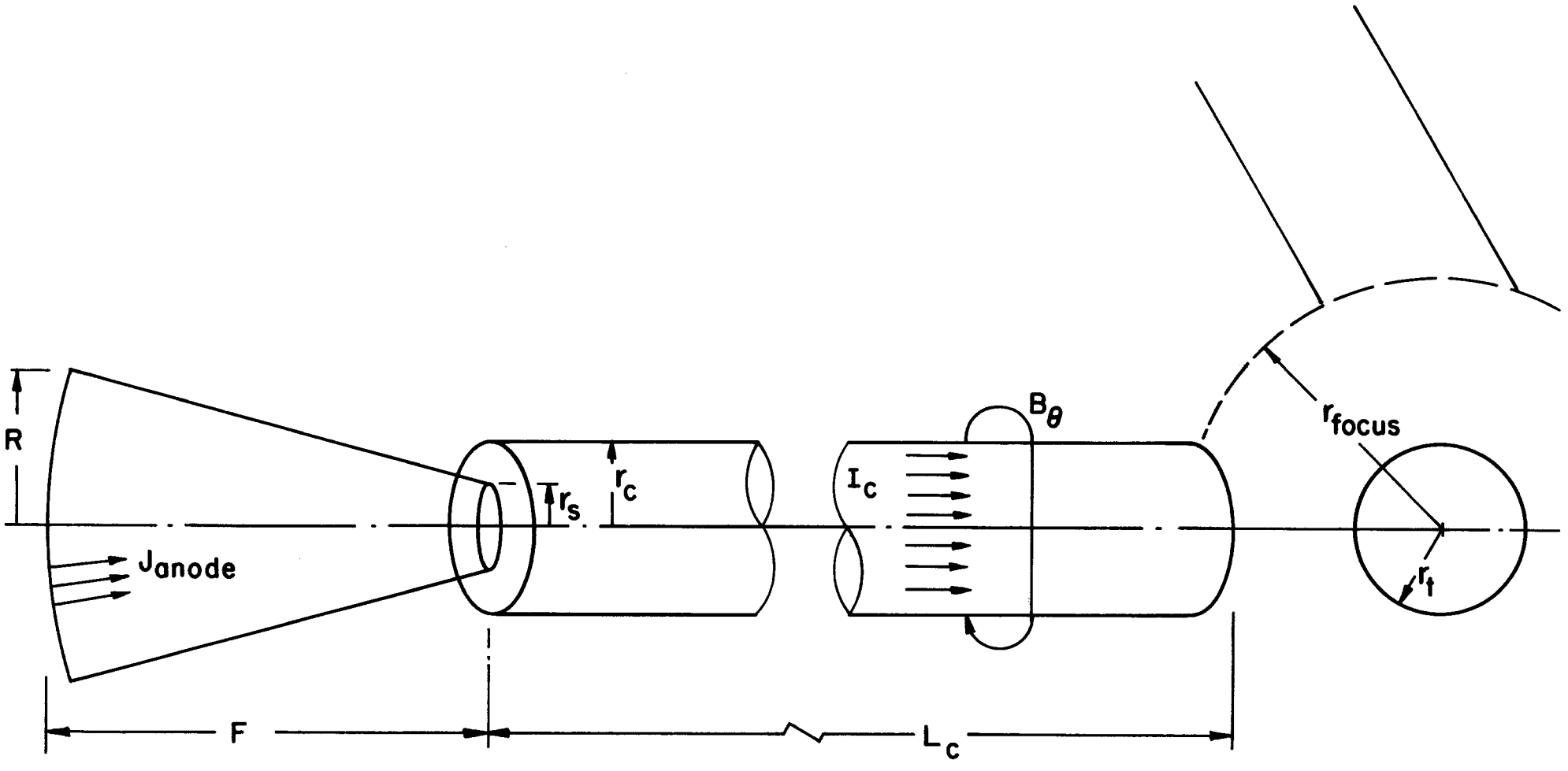

Fig. 3.13. Ion diode geometry.

bilities at channel currents in excess of 45 kA. If we use this as a guide and limit the maximum channel current to 45 kA then the maximum entrance angle can be no greater than 0.1 radians. Choosing this as our value we find that the drift length must be 79.4 cm in order for the diode to deliver ions with a maximum entrance angle of 0.1 radians. In this case the channel radius is 1 cm to be consistent with the value of α_m = 0.1 radian. Again, this channel radius is larger than the target and the ions must be actively focused.

In conclusion, the constraint of 1 kA/cm^2 anode current density puts severe constraints on the drift region length, the channel radius and the channel current.

Case 3 15 MeV D - 5 kA/cm^2 Anode Current Density

In this case we investigate the propagation of 15 MeV D^{+1} ions from a diode with 5 kA/cm^2 maximum current density. The total power delivered to the target must be 240 TW. This choice of ion energy is consistent with "HIBALL-type" target designs studied at KfK. With a 75% transport efficiency and 3:1 bunching factor the diodes are required to supply 107 TW. In this case there are 24 modules, following Smith's design, hence each channel must transport 4.5 TW. The combination of lower voltage and more diodes implies that each diode must supply 0.3 MA and a limiting current density of 5 kA/cm^2 means that each diode has a radius of 4.34 cm. Using Fig. 3.5 we see that 4.5 TW can be stably transported so long as $\alpha_m \geq 0.075$ radians. If we choose this value, then the drift length is

$$F = \frac{4.34}{\sin 0.075} = 58 \text{ cm} .$$

This is quite excessive, so instead we choose the maximum entrance angle to be 0.1 radians, then the drift length is 43.4 cm. The channel radius is 0.5 cm and the focal spot size is chosen to be 0.25 cm. This requires a brightness half angle of 5.8 mrad. With these parameters the channel current is 45 kA and the maximum magnetic field is 18 kG. Using the ION code we see in Fig. 3.14 that at 10 meters down the channel 75% of the ions are confined to a radius of 0.5 cm.

In conclusion, this is a relatively good set of parameters. The only real difficulty is the 5 kA/cm^2 anode current density.

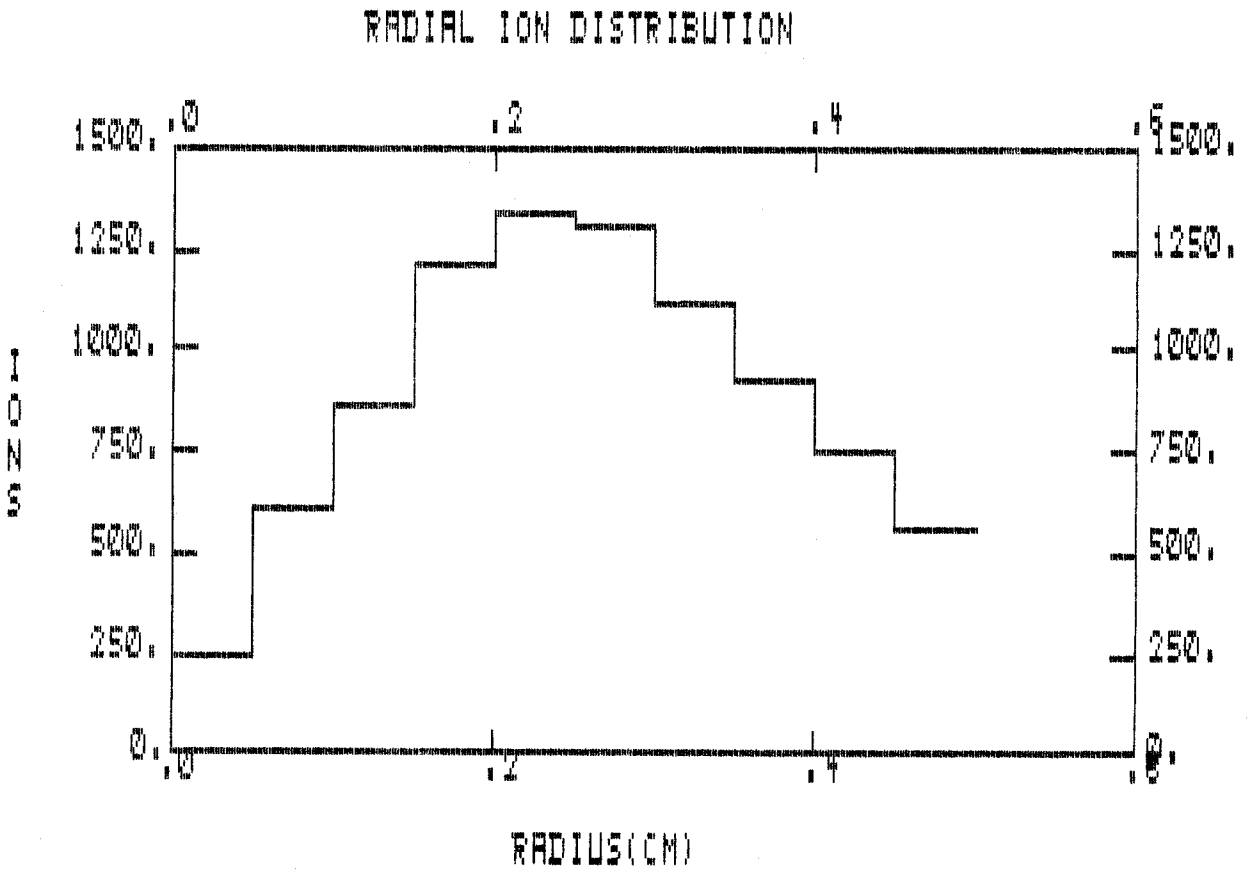

Fig. 3.14. Radial ion distribution at the target plane in a uniform channel.

Case 4 15 MeV D - 1 kA/cm^2 Anode Current Density

In this case we investigate 15 MeV D^{+1} ions with an anode current density of 1 kA/cm^2. We require 240 TW to be delivered to the target with 75% transport efficiency and 3:1 bunching factor. The lower current density means that the diode radius must be increased to 9.7 cm. For a maximum entrance angle of 0.1 radian the drift length must be 97 cm, a very long distance. The required brightness half angle is now 2.6 mrad. With these choices the remaining parameters are the same as the previous case. The channel radius is 0.5 cm and the channel current is 45 kA.

General Summary and Conclusions

The results of the previous analysis are summarized in Table 3.2. There appears to be a very small operating range for the parameters important to ion generation and propagation. The major issues are:

1. allowable anode current density;
2. allowable drift region length; and
3. allowable channel current.

The maximum transportable ion power was an issue for the 30 MeV Li with 18 channels but was not an issue for 15 MeV D with 24 channels. The concern about maximum allowable channel current severely limited the maximum entrance angle and thus made diode design difficult. Obviously, higher voltage and a greater number of channels would help to alleviate these problems. The question remains, how do we make the trade-offs between conservative and non-conservative design choices for each component of the power flow system? For the specific cases that have been evaluated, the 15 MeV D^{+1} with 5 kA/cm^2 anode current density represents the best set of parameters for the LIBRA design. Fine tuning could probably improve these slightly, but the restricted range of acceptable values for parameters in this analysis points out the difficulty in making significant improvements.

Table 3.2. Self-Consistent Ion Propagation Parameters

	CASE 1	2	3	4
Power on target (TW)	240	240	240	240
Ion energy (MeV)	30	30	15	15
Ion specie	Li	Li	D	D
Number of channels	18	18	24	24
Diode radius (cm)	3.55	7.94	4.34	9.7
Drift length (cm)	50	79.4	43.4	97
Anode current density (kA/cm^2)	5	1	5	1
Max. entrance angle (radian)	0.071	0.1	0.1	0.1
Channel radius (cm)	0.8	1.0	0.5	0.5
Focus spot size (cm)	0.4	0.5	0.25	0.25
Channel current (kA)	27.5	45	45	45
Max. magnetic field (kG)	6.9	9	18	18
Bunching factor	3	3	3	3
Channel length (cm)	1000	1000	1000	1000
Brightness half angle (radians)	0.008	0.006	0.058	0.003
Propagation efficiency	0.75	0.75	0.75	0.75
Ion power supplied by diodes (TW)	107	107	107	107
EM power supplied to diodes (TW)	143	143	143	143

References for Chapter 3

1. B. Badger et al., "Progress Report for the LIBRA Light Ion Beam Fusion Reactor Project for the Period January-June 1984," Fusion Power Associates Report FPA-84-1, July 1984.

2. Ian D. Smith, Leland G. Schlitt, and Hart N. Nishimoto, "High Voltage Ion Diode Drivers Based on the Helia Approach," Pulse Sciences Inc. Report PSI-FR-184, September 1984.

3. Private discussion, W. Schmidt, KfK, July 1984.

4. J.N. Olson and R.J. Leeper, "Ion Beam Transport in Laser-Initiated Discharge Channels," J. Appl. Phys. 53, 3397 (1982).

4. MECHANICAL ANALYSIS OF INPORT UNITS

4.1 Introduction

Rigorous derivations of the equations of motion for INPORT have been developed. These are necessary for mechanical stability analysis and the determination of out-of-plane response following in-plane excitation. Results have been obtained for the vibrational mode shapes and corresponding frequencies of INPORTs for which the axial tension gradient from gravity is accurately assessed. Exact solutions and an approximate verification have been determined. Complete details of this work can be found in reports FPA-84-2[1] and FPA-84-3.[2] The description which follows summarizes this work.

4.2 Model Description

The system under consideration (Fig. 4.1) consists of a uniform tube of length ℓ supported at each end. It has a cross-sectional area A_t, mass per unit length m_t and flexural rigidity EI. The internal fluid flows axially with velocity c, cross-sectional flow area A_f and mass per unit length m_f. The mean pressure within the tube is p, measured above atmospheric.

In its undeformed (equilibrium) position the longitudinal axis of the tube coincides with the x axis. With this vertical configuration, gravity effects will be assessed. Free and forced response of the tube is allowed in both the x-y and x-z planes along with longitudinal deformations.

In the problem formulation, various assumptions have been made concerning both the tube and the fluid. They include:

1. The effects of rotary inertia and shear deformation of the tube are neglected.
2. Nominal dimensions of the tube do not change significantly with internal pressure or displacements.
3. External drag forces are neglected.
4. The fluid is viscous and incompressible.
5. Secondary flow effects and radial variations in the flow velocity are neglected.
6. Only the mechanical response of the tube is considered; thermal effects are not assessed.

4.3 Derivation of the Equations of Motion

An energy approach has been used to derive the equations of motion for the system. The kinetic energy associated with the motion of the tube is

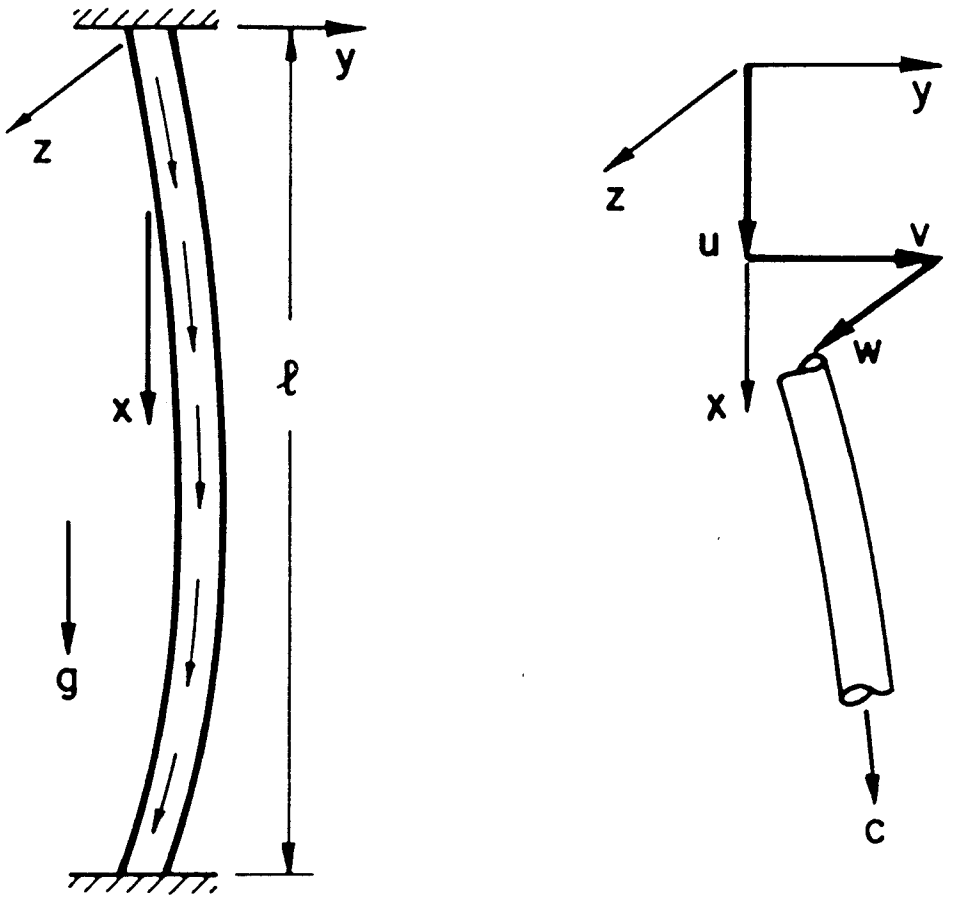

Fig. 4.1. Tube geometry and coordinate system.

given by

$$K_{tube} = \frac{1}{2} m_t \int_0^{\ell} [(\frac{\partial u}{\partial t})^2 + (\frac{\partial v}{\partial t})^2 + (\frac{\partial w}{\partial t})^2] \, dx \tag{1}$$

where u, v and w are the displacement components in the x, y and z directions, respectively, and t denotes time. For the fluid, the magnitude of the flow velocity c may have a harmonic component to include the possibility of pulsating flow, i.e.,

$$c = c_o(1 + \mu \cos \Omega t) \tag{2}$$

where c_o is the mean velocity, μ is the amplification factor and Ω is the forcing frequency. The velocity components of the fluid flow can be described using Fig. 4.1, which shows the direction of c tangent to the deformed tube centerline. Thus, the kinetic energy due to the flowing fluid can be expressed as

$$K_{fluid} = \frac{1}{2} m_f \int_0^{\ell} [(\frac{\partial u}{\partial t} + c)^2 + (\frac{\partial v}{\partial t} + c \frac{\partial v}{\partial x})^2 + (\frac{\partial w}{\partial t} + c \frac{\partial w}{\partial x})^2] \, dx \, . \tag{3}$$

It should be noted that nonlinear inertia effects from the fluid have not been included.

The potential energy of the system consists of the elastic energy stored in tension and the elastic strain energy due to bending. The contribution from the axial load is

$$U_{tension} = \frac{1}{2A_t E} \int_0^{\ell} T^2 \, dx \tag{4}$$

where T is the absolute tension in the tube and E denotes the elastic modulus. In general, this tension is comprised of a number of components including a static pretensile load T_o and the weight of the tube and fluid which results in a linear axial variation. Also, since the lower end of the tube is not free and the fluid is allowed to discharge into a pool, there will be an additional tensile term equal to $pA_t(2\nu - 1)$ for a thin tube, where ν denotes Poisson's ratio. In order to take into account the possibility of large amplitude motion, nonlinear tension effects can be included by considering

higher order terms in the expression for the tube extension. Thus, the tension can be written as

$$T = T_o - pA_t(1 - 2\nu) + (m_f + m_t)g(\ell - x) + EA_t \left(\frac{ds - dx}{dx}\right) \tag{5}$$

where

$$\frac{ds}{dx} = \left[\left(1 + \frac{\partial u}{\partial x}\right)^2 + \left(\frac{\partial v}{\partial x}\right)^2 + \left(\frac{\partial w}{\partial x}\right)^2\right]^{1/2} . \tag{6}$$

The strain energy due to bending is given by

$$U_{bending} = \frac{1}{2EI} \int_0^{\ell} \left[\left(\frac{EI \frac{\partial^2 v}{\partial x^2}}{\left[1 + \left(\frac{\partial v}{\partial x}\right)^2\right]^{3/2}}\right)^2 + \left(\frac{EI \frac{\partial^2 w}{\partial x^2}}{\left[1 + \left(\frac{\partial w}{\partial x}\right)^2\right]^{3/2}}\right)^2\right] dx \tag{7}$$

where I represents the cross sectional moment of inertia of the tube.

The work done by nonconservative damping forces can be expressed as

$$\int_{t_1}^{t_2} \delta W_{nc}\, dt = \int_{t_1}^{t_2} \int_0^{\ell} \kappa_o m_t \left[\frac{\partial u}{\partial t}\, \delta u\, dx + \frac{\partial v}{\partial t}\, \delta v\, dx + \frac{\partial w}{\partial t}\, \delta w\, dx\right] dt \tag{8}$$

where κ_o is considered to be an equivalent damping coefficient that includes both internal structural damping and viscous damping due to the friction of the tube with the surrounding medium. It should be noted that κ_o can be adjusted to comply with the conditions of the problem.

Finally, employing variational calculus, the three-dimensional equations of motion are

$$(m_f + m_t)\frac{\partial^2 u}{\partial t^2} + m_f \frac{\partial c}{\partial t} + \kappa_o m_t \frac{\partial u}{\partial t} - \frac{T^*(m_f + m_t)g}{A_t E} + (m_f + m_t)g\left[1 - \frac{\partial u}{\partial x}\right.$$

$$\left. - \frac{1}{2}\left(\frac{\partial v}{\partial x}\right)^2 - \frac{1}{2}\left(\frac{\partial w}{\partial x}\right)^2 + \frac{1}{2}\left(\frac{\partial u}{\partial x}\right)\left(\frac{\partial v}{\partial x}\right)^2 + \frac{1}{2}\left(\frac{\partial u}{\partial x}\right)\left(\frac{\partial w}{\partial x}\right)^2\right] - EA_t \frac{\partial^2 u}{\partial x^2} \tag{9}$$

$$- \frac{\partial}{\partial x}\left\{(EA_t - T^*)\left[\frac{1}{2}\left(\frac{\partial v}{\partial x}\right)^2 + \frac{1}{2}\left(\frac{\partial w}{\partial x}\right)^2 - \left(\frac{\partial u}{\partial x}\right)\left(\frac{\partial v}{\partial x}\right)^2 - \left(\frac{\partial u}{\partial x}\right)\left(\frac{\partial w}{\partial x}\right)^2\right]\right\} = 0$$

$$(m_f + m_t)\frac{\partial^2 v}{\partial t^2} + 2m_f c\frac{\partial^2 v}{\partial x \partial t} + m_f c^2\frac{\partial^2 v}{\partial x^2} + m_f\frac{\partial c}{\partial t}\frac{\partial v}{\partial x} + \kappa_o m_t\frac{\partial v}{\partial t} - \frac{\partial}{\partial x}\{T^*\frac{\partial v}{\partial x}$$

$$+ (EA_t - T^*)[\frac{\partial u}{\partial x} - (\frac{\partial u}{\partial x})^2 + \frac{1}{2}(\frac{\partial v}{\partial x})^2 + \frac{1}{2}(\frac{\partial w}{\partial x})^2]\frac{\partial v}{\partial x}\} + EI\frac{\partial^4 v}{\partial x^4} \qquad (10)$$

$$- 3EI(\frac{\partial v}{\partial x})^2\frac{\partial^4 v}{\partial x^4} - 12EI(\frac{\partial v}{\partial x})(\frac{\partial^2 v}{\partial x^2})(\frac{\partial^3 v}{\partial x^3}) - 3EI(\frac{\partial^2 v}{\partial x^2})^3 = 0$$

where $$T^* = T_o - pA_f(1 - 2\nu) + (m_f + m_t)g(\ell - x) \ . \qquad (11)$$

The equation for the displacement component w is not given here but is structured the same as Eq. (10). These equations are presented in general form with the order of the nonlinear terms high enough to cover a wider range of potential problems. When different categories of problems are analyzed, simplifications will reduce the complexity of the equations, e.g., negligible flexural stiffness, axial displacements which are much smaller than lateral and transverse components, etc. Such reductions will be developed for particular forced response cases.

4.4 Planar Vibrations of LIBRA INPORTs Including Gravity Gradient Effects

In order to determine the basic modal characteristics of the tube, Eq. (10) has been linearized to decouple the lateral and longitudinal displacements. For transverse motion it is assumed that the effect of the Coriolis acceleration of the fluid, given by $2m_f c(\partial^2 v/\partial x \partial t)$, can be neglected. Also, since the INPORTs are considered as completely flexible tubes, Eq. (10) becomes

$$\frac{\partial}{\partial x}\{[(T_o - pA_f(1 - 2\nu) + (m_t + m_f)g(\ell - x) - m_f c^2]\frac{\partial v}{\partial x}\}$$

$$- \kappa_o(m_t + m_f)\frac{\partial v}{\partial t} - (m_t + m_f)\frac{\partial^2 v}{\partial t^2} = 0 \ . \qquad (12)$$

The equation of motion may be expressed in dimensionless terms by defining the

following dimensionless quantities:

$$\bar{v} = \frac{v}{\ell}$$

$$\xi = \frac{T_o - pA_f(1 - 2\nu) + (m_t + m_f)g(\ell - x) - m_f c^2}{(m_t + m_f)g\ell} \tag{13}$$

$$\tau = \sqrt{\frac{g}{\ell}}\, t \ .$$

Substitution into Eq. (12) yields

$$\frac{\partial}{\partial \xi}\left\{\xi \frac{\partial \bar{v}}{\partial \xi}\right\} - \kappa \frac{\partial \bar{v}}{\partial \tau} - \frac{\partial^2 \bar{v}}{\partial \tau^2} = 0 \tag{14}$$

where the damping parameter κ is given by

$$\kappa = \kappa_o \sqrt{\frac{\ell}{g}} \ . \tag{15}$$

Equation (14) can be reduced to an ordinary differential equation by assuming a harmonic solution of the form

$$\bar{v}(\xi, \tau) = \mathrm{Re}\left\{\phi(\xi)\bar{X}e^{i\bar{\omega}\tau}\right\} \tag{16}$$

where $\phi(\xi)$ is a complex function and $\bar{\omega}$ is the dimensionless frequency. Substitution of Eq. (16) into (14) gives

$$\frac{d}{d\xi}\left(\xi \frac{d\phi(\xi)}{d\xi}\right) + (\bar{\omega}^2 - i\kappa\bar{\omega})\ \phi(\xi) = 0 \ . \tag{17}$$

The solution to Eq. (17) involves Bessel functions of the first and second kind of zero order, namely

$$\phi(\xi) = AJ_0(\lambda\sqrt{\xi}) + BY_0(\lambda\sqrt{\xi}) \tag{18}$$

where

$$\lambda = \left\{4(\bar{\omega}^2 - i\kappa\bar{\omega})\right\}^{1/2} \ . \tag{19}$$

For a general solution A and B must be complex constants.

A closer look at the argument of J_o and Y_o indicates

$$\lambda\sqrt{\xi} = \{4\bar{\omega}^2(\bar{T} - \frac{x}{\ell}) - 4i\kappa\bar{\omega}(\bar{T} - \frac{x}{\ell})\}^{1/2} \tag{20}$$

where the dimensionless tension and frequency are given by

$$\bar{T} = \frac{T_o - pA_f(1 - 2\nu) + (m_t + m_f)g\ell - m_f c^2}{(m_t + m_f)g\ell} \tag{21}$$

$$\bar{\omega} = \sqrt{\frac{\ell}{g}}\,\omega \ . \tag{22}$$

Finally, the complete solution to Eq. (14) can be expressed as a superposition of an infinite set of the normal modes of the tube, i.e.,

$$\bar{v}(\xi,\tau) = \mathrm{Re}\{\sum_{n=1}^{\infty} \phi_n(\xi)\bar{X}_n e^{i\bar{\omega}_n\tau}\} \tag{23}$$

which also includes the complex constant

$$\bar{X}_n = X_n e^{i\alpha_n} \tag{24}$$

where X_n and α_n are determined by initial conditions. Here $\phi_n(\xi)$ represents the eigenfunctions of the tube which must satisfy the boundary conditions of the problem. For this case

$$\bar{v}(\xi,\tau) = \phi_n(\xi) = 0 \qquad \text{at } x = 0 \text{ and } x = \ell \ . \tag{25}$$

Equation (25) can then be used to determine the dimensionless frequencies $\bar{\omega}_n$ and complex constants A_n and B_n of Eq. (9).

For convenience, Eq. (23) has been rewritten so it contains only the real part. Complex terms can be broken up into their real and imaginary parts by letting

$$A_n = A_{Rn} + iA_{In}$$

$$B_n = B_{Rn} + iB_{In}$$

$$J_o(\lambda_n\sqrt{\xi}) = J_{oR}(\lambda_n\sqrt{\xi}) + iJ_{oI}(\lambda_n\sqrt{\xi}) \tag{26}$$

$$Y_o(\lambda_n\sqrt{\xi}) = Y_{oR}(\lambda_n\sqrt{\xi}) + iY_{oI}(\lambda_n\sqrt{\xi})$$

where R and I represent the real and imaginary parts, respectively. Also, let

$$\bar{X}_n e^{i\bar{\omega}_n\tau} = X_n e^{i(\bar{\omega}_n\tau - \alpha_n)} . \tag{27}$$

Equations (26) and (27) are substituted into (18) and (23). After simplifying and retaining the real part only

$$\bar{v}(\xi,\tau) = \sum_{n=1}^{\infty} X_n[A_{Rn}J_{oR}(\lambda_n\sqrt{\xi}) - A_{In}J_{oI}(\lambda_n\sqrt{\xi}) + B_{Rn}Y_{oR}(\lambda_n\sqrt{\xi}) - B_{In}Y_{oI}(\lambda_n\sqrt{\xi})]$$
$$\times \cos(\bar{\omega}_n\tau - \alpha_n) - X_n[A_{Rn}J_{oI}(\lambda_n\sqrt{\xi}) + A_{In}J_{oR}(\lambda_n\sqrt{\xi}) + B_{Rn}Y_{oI}(\lambda_n\sqrt{\xi})$$
$$+ B_{In}Y_{oR}(\lambda_n\sqrt{\xi})] \times \sin(\bar{\omega}_n\tau - \alpha_n) \tag{28}$$

which is the general solution to Eq. (14).

To determine natural frequencies and mode shapes, the eigenfunctions $\phi_n(\xi)$ are required to satisfy the boundary conditions given in Eq. (25). This results in the following set of equations

$$A_{Rn}J_{oR}(\lambda_n\sqrt{\xi_1}) - A_{In}J_{oI}(\lambda_n\sqrt{\xi_1}) + B_{Rn}Y_{oR}(\lambda_n\sqrt{\xi_1}) - B_{In}Y_{oI}(\lambda_n\sqrt{\xi_1}) = 0$$

$$A_{Rn}J_{oI}(\lambda_n\sqrt{\xi_1}) + A_{In}J_{oR}(\lambda_n\sqrt{\xi_1}) + B_{Rn}Y_{oI}(\lambda_n\sqrt{\xi_1}) + B_{In}Y_{oR}(\lambda_n\sqrt{\xi_1}) = 0$$
$$\tag{29}$$
$$A_{Rn}J_{oR}(\lambda_n\sqrt{\xi_2}) - A_{In}J_{oI}(\lambda_n\sqrt{\xi_2}) + B_{Rn}Y_{oR}(\lambda_n\sqrt{\xi_2}) - B_{In}Y_{oI}(\lambda_n\sqrt{\xi_2}) = 0$$

$$A_{Rn}J_{oI}(\lambda_n\sqrt{\xi_2}) + A_{In}J_{oR}(\lambda_n\sqrt{\xi_2}) + B_{Rn}Y_{oI}(\lambda_n\sqrt{\xi_2}) + B_{In}Y_{oR}(\lambda_n\sqrt{\xi_2}) = 0$$

where ξ_1 and ξ_2 have been used to represent ξ evaluated at $x = 0$ and $x = \ell$, respectively. For a nontrivial solution to (29) the n determinants of the terms multiplying the A's and B's must equal zero, i.e.,

$$\begin{vmatrix} J_{oR}(\lambda_n\sqrt{\xi_1}) & -J_{oI}(\lambda_n\sqrt{\xi_1}) & Y_{oR}(\lambda_n\sqrt{\xi_1}) & -Y_{oI}(\lambda_n\sqrt{\xi_1}) \\ J_{oI}(\lambda_n\sqrt{\xi_1}) & J_{oR}(\lambda_n\sqrt{\xi_1}) & Y_{oI}(\lambda_n\sqrt{\xi_1}) & Y_{oR}(\lambda_n\sqrt{\xi_1}) \\ J_{oR}(\lambda_n\sqrt{\xi_2}) & -J_{oI}(\lambda_n\sqrt{\xi_2}) & Y_{oR}(\lambda_n\sqrt{\xi_2}) & -Y_{oI}(\lambda_n\sqrt{\xi_2}) \\ J_{oI}(\lambda_n\sqrt{\xi_2}) & J_{oR}(\lambda_n\sqrt{\xi_2}) & Y_{oI}(\lambda_n\sqrt{\xi_2}) & Y_{oR}(\lambda_n\sqrt{\xi_2}) \end{vmatrix} = 0 \quad n = 1,2,3,\ldots,\infty \tag{30}$$

The solution procedure, then, involves choosing a value of $\bar{\omega}$, calculating the argument given by Eq. (20) and corresponding Bessel function, and finally checking the value of the determinant. After $\bar{\omega}$ is found, the relative values of the complex constants A and B can be determined from (30). This procedure is repeated until the number of modes identified is sufficient to completely describe the tube motion.

4.5 Numerical Results for Frequencies and Mode Shapes

An analysis was performed to determine natural frequencies and mode shapes for the special case of zero damping. Setting the damping parameter, κ, to zero in Eq. (20), eliminates the imaginary term of the argument. With the restriction $\bar{T} > 1.0$, J_o and Y_o are assured to be real. Consequently, the equations in (29) will uncouple giving the following two sets of equations

$$\begin{aligned} A_{Rn}J_{oR}(\lambda_n\sqrt{\xi_1}) + B_{Rn}Y_{oR}(\lambda_n\sqrt{\xi_1}) &= 0 \\ A_{Rn}J_{oR}(\lambda_n\sqrt{\xi_2}) + B_{Rn}Y_{oR}(\lambda_n\sqrt{\xi_2}) &= 0 \\ A_{In}J_{oR}(\lambda_n\sqrt{\xi_1}) + B_{In}Y_{oR}(\lambda_n\sqrt{\xi_1}) &= 0 \\ A_{In}J_{oR}(\lambda_n\sqrt{\xi_2}) + B_{In}Y_{oR}(\lambda_n\sqrt{\xi_2}) &= 0 \ . \end{aligned} \tag{31}$$

From the above, it is obvious that

$$\begin{aligned} A_{Rn} &= A_{In} \\ B_{Rn} &= B_{In} \end{aligned} \tag{32}$$

and the necessary condition for a nontrivial solution is

$$J_{oR}(\lambda_n\sqrt{\xi_1})Y_{oR}(\lambda_n\sqrt{\xi_2}) - Y_{oR}(\lambda_n\sqrt{\xi_1})J_{oR}(\lambda_n\sqrt{\xi_2}) = 0 \quad . \tag{33}$$

Therefore, Eq. (33) is used to define the natural frequencies of the system.

Along the same lines, the eigenfunctions describing the mode shapes can be simplified to:

$$\phi_n(\xi) = C_n\left[J_o(\lambda_n\sqrt{\xi}) - \frac{J_o(\lambda_n\sqrt{\xi_1})}{Y_o(\lambda_n\sqrt{\xi_1})} Y_o(\lambda_n\sqrt{\xi})\right] \tag{34}$$

where C_n is an arbitrary constant and can be incorporated into X_n in (27).

Equations (33) and (34) have been programmed to cover a range of tensions, $\bar{T}$. Accuracy problems arise when solving these equations since the arguments of the Bessel functions given in (20) can become "relatively" large. Therefore, to eliminate the possibility of round-off errors, calculations were done on a Cray computer. Function subroutines from IMSL were used to calculate J_o's and Y_o's. These allowed arguments in the following ranges

Function	Range of Argument
J_o	$<< 1.3 \times 10^8$
Y_o	2.9×10^{-39} to 1.3×10^8

where both single and double precision are supported. Also, the method of bisection, based on the use of sign changes to detect a zero, was used to determine the roots of (33).

The first ten natural frequencies computed are shown in Fig. 4.2. Tabular values to three decimal places corresponding to these curves are given in FPA-84-3.[2] Calculations were performed letting $\bar{T}$ approach 1 since $Y_o(0)$ is negatively infinite. Figures 4.3-4.5 show the first, second and tenth mode shapes for dimensionless tensions of 1.1, 2.0 and 3.0. For convenience, each has been individually normalized. Asymmetry is considerably noticeable with the lower tensions. Figure 4.6 shows the shifts of the maximum amplitude and zero crossing for modes 1 and 2 due to the nonlinear effects of the tension. Consequently, as $\bar{T}$ becomes much greater than the weight the natural frequencies and mode shapes will approach that of a classic string.

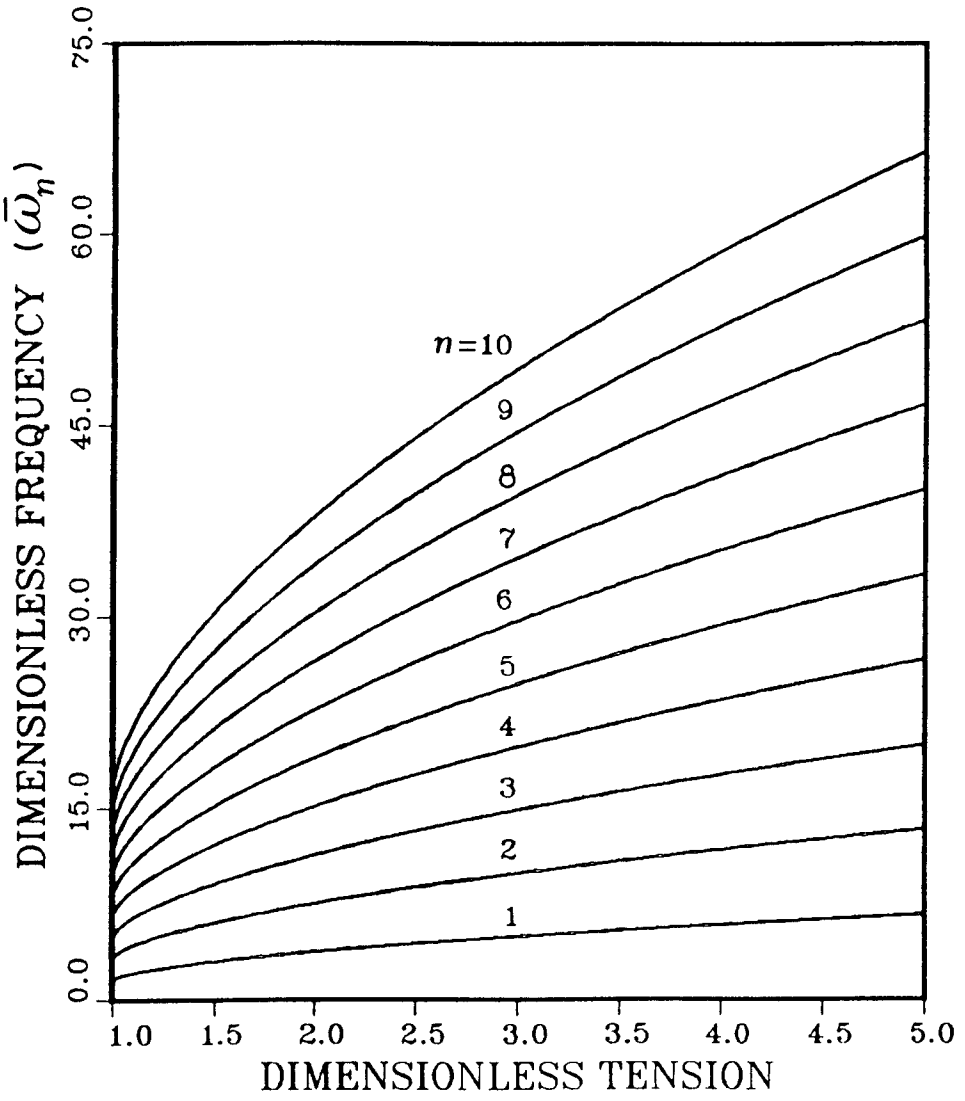

Fig. 4.2. Natural frequencies of heavy tubes.

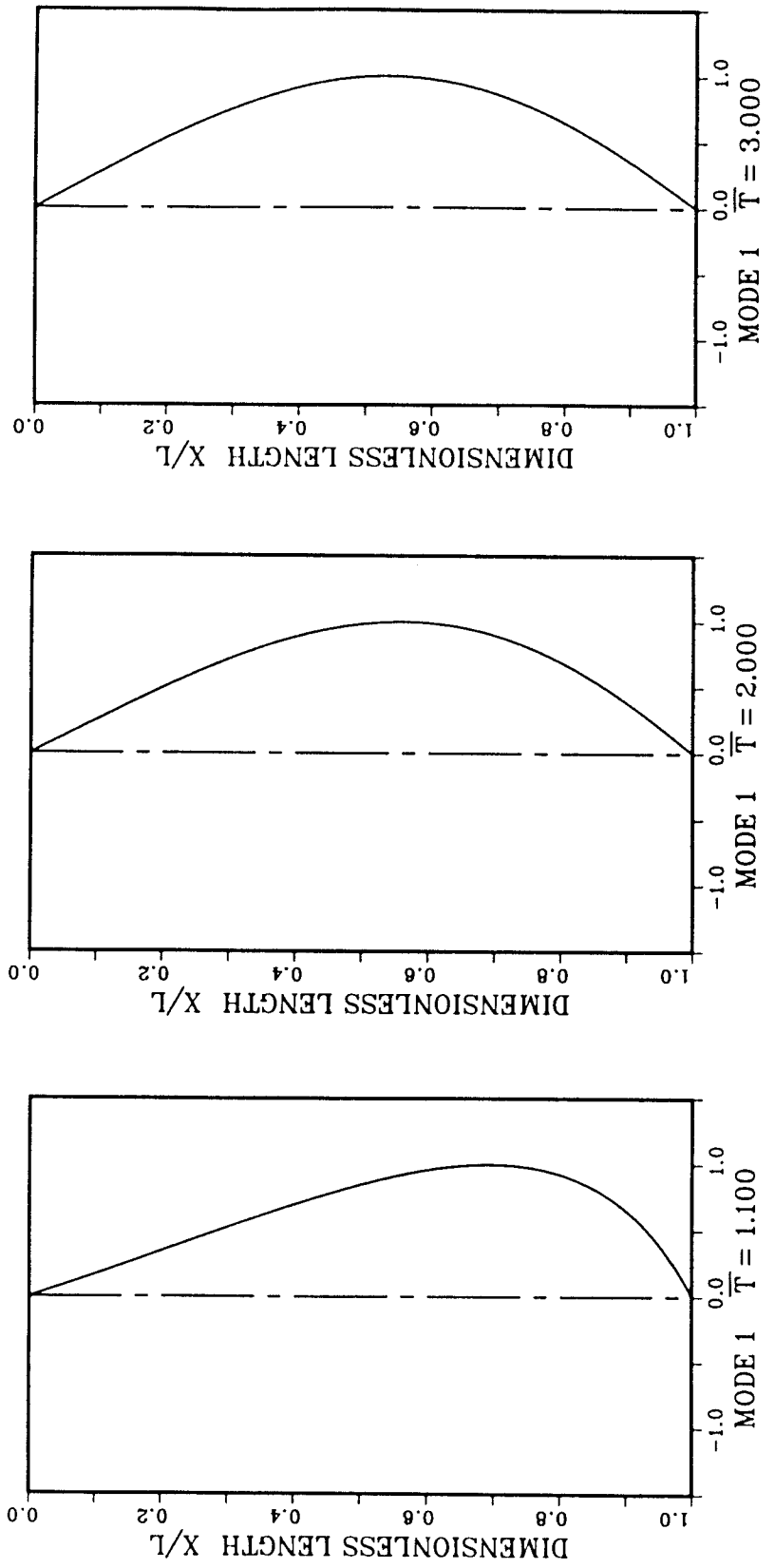

Fig. 4.3. Mode shape 1 for dimensionless tensions of 1.1, 2.0 and 3.0.

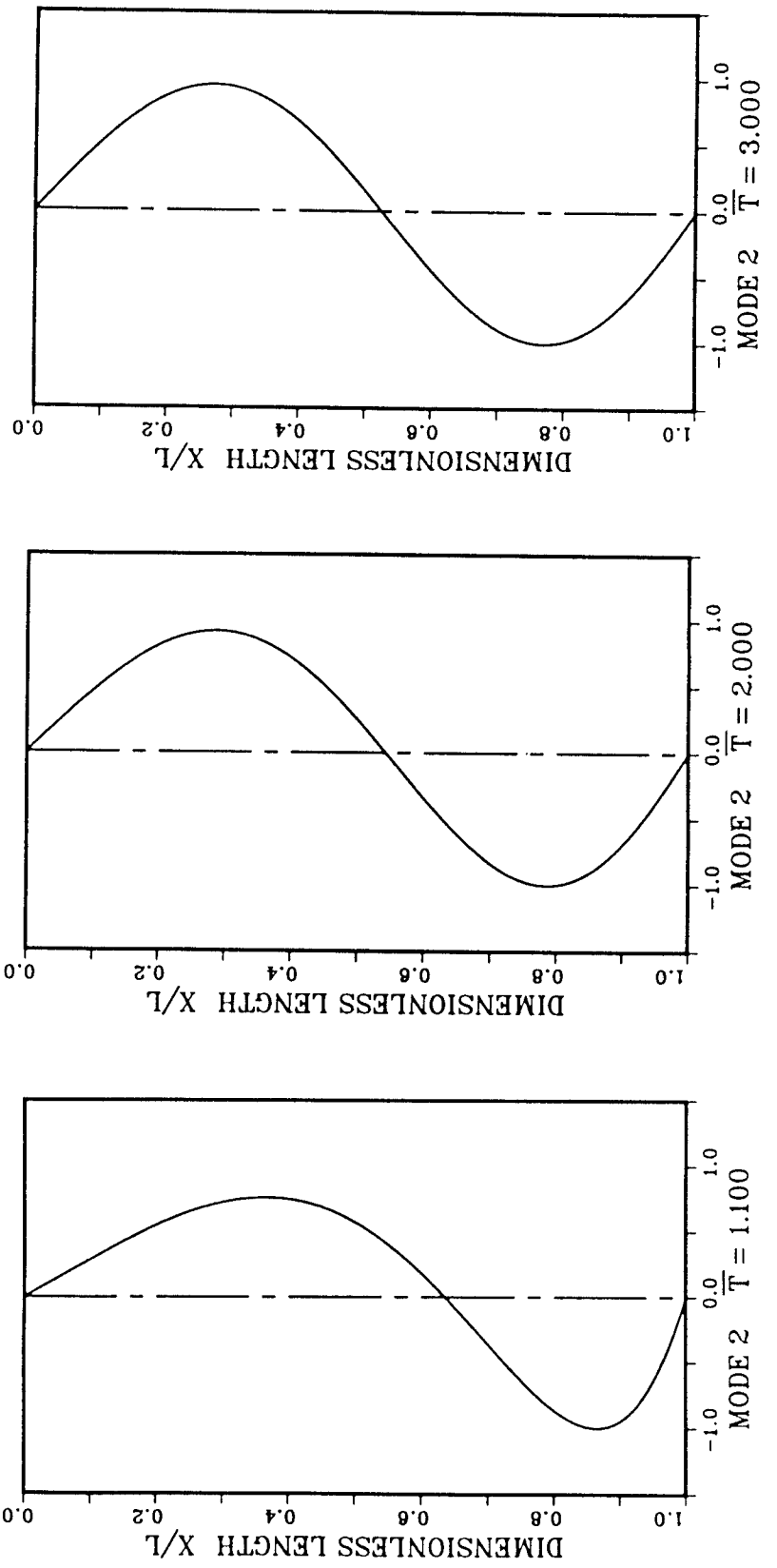

Fig. 4.4. Mode shape 2 for dimensionless tensions of 1.1, 2.0 and 3.0.

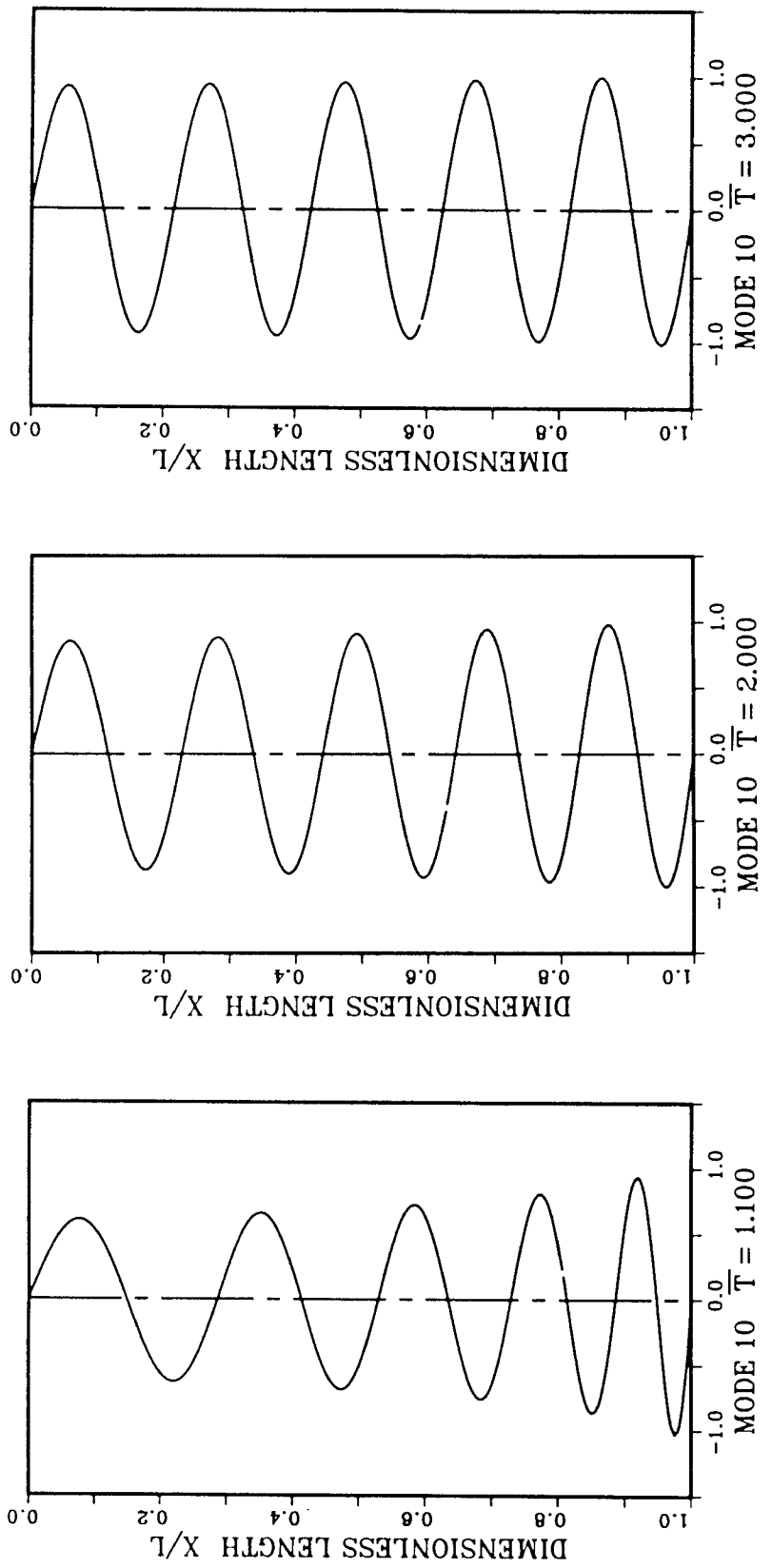

Fig. 4.5. Mode shape 10 for dimensionless tensions of 1.1, 2.0 and 3.0.

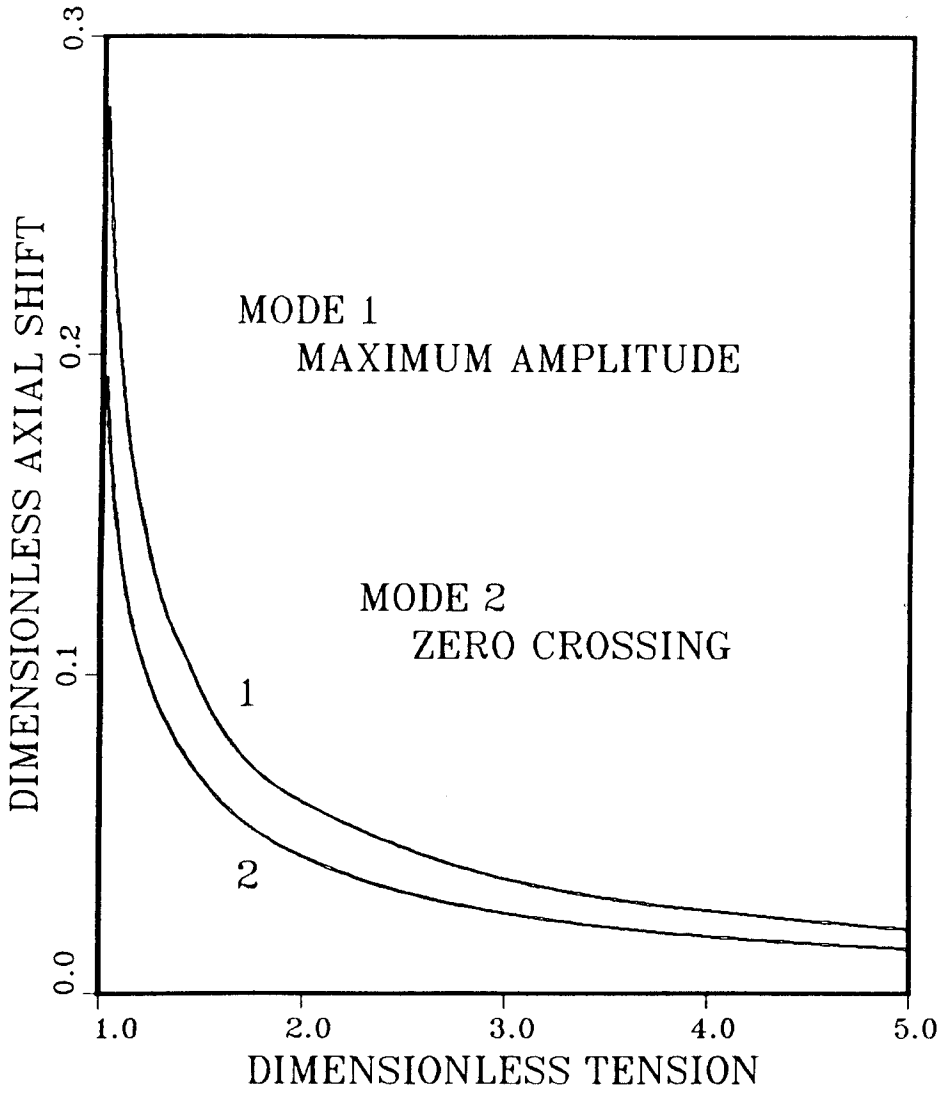

Fig. 4.6. Shifts in locations of maximum amplitude and zero crossings.

These exact results for mode shapes and frequencies were substantiated by a perturbation analysis. Details of this can also be found in FPA-84-3.

4.6 Concluding Remarks

The complete equations of motion for INPORTs have been developed for the analysis of three-dimensional motion and the effects of gravity gradients on the natural frequencies and mode shapes have been determined. For the latter, accurate numerical results support approximations made in earlier planar response calculations in which the tension gradient was replaced by its mean value. Work in progress now is centered on the analysis of out-of-plane motion. The objectives include the determination of the circumstances under which it will occur, the amplitude of the response (for interference purposes) and, if necessary, design solutions to control such motion.

References for Chapter 4

1. R.L. Engelstad and E.G. Lovell, "Basic Theory for Three-Dimensional Motion of LIBRA INPORT Tubes," Fusion Power Associates Report FPA-84-2, October 1984.

2. R.L. Engelstad and E.G. Lovell, "Planar Vibrations of LIBRA INPORT Tubes Including Gravity Gradient Effects," Fusion Power Associates Report FPA-84-3, October 1984.

5. GAS FLOW THROUGH INPORT UNITS

The INPORT unit concept[1] combines the advantages of liquid metal jet protection of the first wall from neutron damage and the wetted wall thin liquid metal film protection of the first structural surface from surface heat loads caused by target x-rays and ion debris. The concept was originally introduced in the evacuated cavity of the HIBALL reactor design[2] and has been extended to the gas filled cavity of the LIBRA reactor.[3] In the case of an evacuated cavity, the principal design issues are: (1) the loading of the INPORT units due to ablated liquid metal film by target x-rays and ions, and (2) the rate at which the ablated liquid metal recondenses back onto the bank of tubes. This second issue determines the allowable repetition rate in the cavity. For the situation where a gas is present, as it is in LIBRA or any light ion beam system, the principal design issues include the two previously stated ones plus (3) the heat transfer between the gas and the tubes as the fireball propagates through the tubes. A major concern in light ion fusion systems is the cooling of the gas between shots because this gas heat transfer determines the repetition rate in such systems. This heat transfer has been previously modeled using a simple control volume approach with account taken for choked flow between the rows of tubes.[3] In this last year we have investigated more accurate methods of analyzing this problem.

The problem of the fireball propagation through the bank of INPORT units is fundamentally a fluid dynamics problem of supersonic transient flow around multiple bluff bodies. A review of the literature indicates to us that this problem has not been studied in any detail either computationally or experimentally. Because the interaction of the gas with the INPORT units is basic to the viability of the concept we have decided to undertake a detailed, multifaceted investigation of this phenomenon. As a start, we have developed a two-dimensional compressible fluid dynamics code based upon the SOLA-ICE method.[4] This code is currently being vectorized and its performance evaluated on a Cray XMP-48 computer. Our experience with this relatively simple code will lead us toward the proper computation method of solution for this difficult fluid dynamics problem.

On the experimental side of the problem we are investigating the possibility of using the National Laser Users Facility at the Laboratory for Laser Energetics at the University of Rochester to perform a small scale experiment

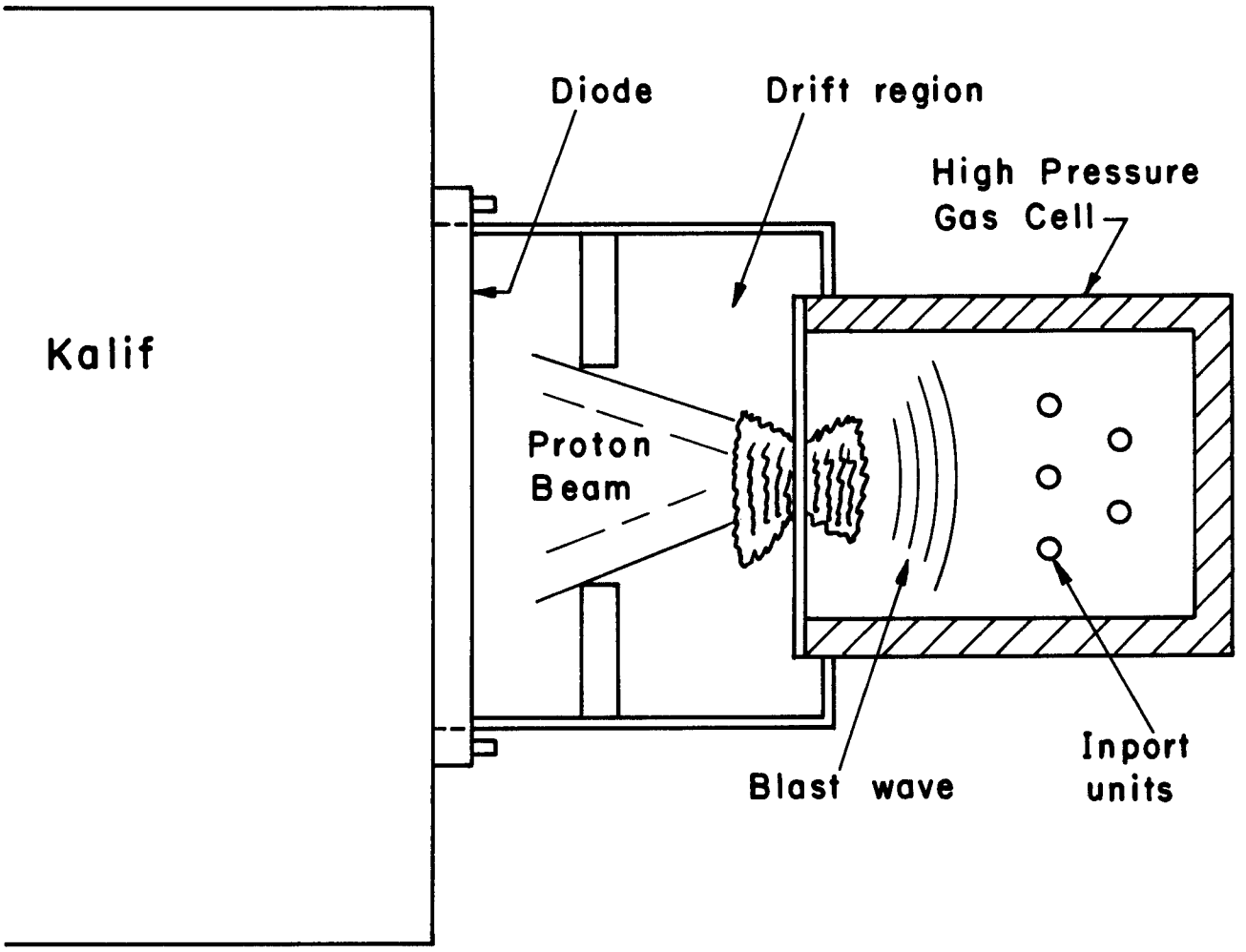

Fig. 5.1. Schematic of experiment to study flow around multiple bluff bodies using Kalif.

where a blast wave is created in a gas by focusing a high power laser onto a small amount of target material. The flow of the microfireball around structures placed near the microexplosion would be measured with interference instrumentation. We are also investigating the possibility of using the Kalif accelerator at KfK to perform this same experiment. Here we would focus a proton beam onto a slab target with a thickness comparable to the range of the protons. The expansion from the back surface of the target could be used to generate a shock wave in a gas as shown in Fig. 5.1. We will perform PHD-IV hydrodynamics calculations to determine the strength of the shock wave that can be generated and will design an experiment to measure the interaction of this shock with multiple bluff bodies.

In conclusion, our work on blast wave-INPORT unit interaction is turning toward more fundamental calculations and experiments that will serve to verify the concept in a very substantial way. These results along with the fatigue analysis that has previously been performed and reported[3] will make the INPORT unit concept the most thoroughly tested first wall protection scheme in the ICF reactor technology field.

References for Chapter 5

1. G.L. Kulcinski, G.A. Moses, et al., "The INPORT Concept, An Improved Method to Protect ICF Reactor First Walls," J. Nucl. Mat. 103 & 104, 103 (1981).

2. B. Badger et al., "HIBALL - A Conceptual Heavy Ion Beam Driven Fusion Reactor Study," University of Wisconsin Fusion Technology Institute Report UWFDM-450, Kernforschungszentrum Karlsruhe Report KFK-3203, June 1981.

3. B. Badger et al., "Annual Report for the LIBRA Light Ion Beam Fusion Reactor Project for the Period January-December 1983," Fusion Power Associates Report FPA-83-8, December 1983.

4. L.D. Cloutman, C.W. Hirt and N.C. Romero, "SOLA-ICE: A Numerical Solution Algorithm for Transient Compressible Fluid Flows," Los Alamos National Laboratory Report LA-6236, February 1976.

6. SUMMARY AND CONCLUSIONS

Progress on the LIBRA light ion fusion reactor study has been made in several different distinct areas due to the "critical issues" nature of the work. A documented version of the Z-PINCH code was delivered and made operational at KfK in July 1984. Versions of the ION and WINDOW codes were also delivered and made operational. After discussions with KfK scientists the Z-PINCH code has subsequently been updated to include the effects of ion beam current density profiles on the plasma channel within the context of the MHD modeling that the code is based upon. This code is currently being tested. An updated version of the ION code that includes the possibility of arbitrary magnetic field profile has been developed and documentation for this code has been written. An updated version of the WINDOW code that allows more general input has been developed and documentation has been written. These codes and documentation are all considered as deliverables from FPA to KfK.

Using the ION and WINDOW codes, sets of consistent parameters have been determined for the pulsed power equipment (using Ian Smith's designs), the diode geometry (using discussions with W. Schmidt and others at KfK as a basis), ion entrance angle to the channel (using the theoretical results of Ottinger, Mosher and Goldstein), maximum allowable channel current (using J. Olson's experiments as a guide), and maximum allowable transportable beam power (using the parameter space defined in the WINDOW code). For these particular calculations, indications are that there is a very small region in this multidimensional parameter space where focusing and propagation are allowed. Discussion of this problem should come at the next joint KfK-FPA review meeting.

Development of equations of motion for the INPORT units has been completed and reported and these equations have been solved for specific cases to determine the motion of the INPORT units when subjected to loadings consistent with the LIBRA design.

Work in the area of cavity gas-INPORT unit interaction has turned toward a more fundamental treatment of the fluid dynamics of transient supersonic flow over multiple bluff bodies. These studies are being pursued both computationally and experimentally. The ultimate results of these efforts along with the fatigue testing will make the INPORT the most advanced first wall protection concept in the ICF reactor design field.